

Population dynamics in flows

Citation for published version (APA):

Guccione, G. (2021). *Population dynamics in flows: numerical and theoretical investigations*. [Phd Thesis 1 (Research TU/e / Graduation TU/e), Applied Physics and Science Education]. Technische Universiteit Eindhoven.

Document status and date:

Published: 25/06/2021

Document Version:

Publisher's PDF, also known as Version of Record (includes final page, issue and volume numbers)

Please check the document version of this publication:

- A submitted manuscript is the version of the article upon submission and before peer-review. There can be important differences between the submitted version and the official published version of record. People interested in the research are advised to contact the author for the final version of the publication, or visit the DOI to the publisher's website.
- The final author version and the galley proof are versions of the publication after peer review.
- The final published version features the final layout of the paper including the volume, issue and page numbers.

[Link to publication](#)

General rights

Copyright and moral rights for the publications made accessible in the public portal are retained by the authors and/or other copyright owners and it is a condition of accessing publications that users recognise and abide by the legal requirements associated with these rights.

- Users may download and print one copy of any publication from the public portal for the purpose of private study or research.
- You may not further distribute the material or use it for any profit-making activity or commercial gain
- You may freely distribute the URL identifying the publication in the public portal.

If the publication is distributed under the terms of Article 25fa of the Dutch Copyright Act, indicated by the "Taverne" license above, please follow below link for the End User Agreement:

www.tue.nl/taverne

Take down policy

If you believe that this document breaches copyright please contact us at:

openaccess@tue.nl

providing details and we will investigate your claim.

**Population dynamics in flows:
numerical and theoretical investigations**

Giorgia Guccione



This work is part of the HPC-LEAP research programme

A catalogue record is available from the Eindhoven University of Technology Library

ISBN: 978-90-386-5297-9

Copyright © 2021 by Giorgia Guccione, Eindhoven, The Netherlands.

All rights are reserved. No part of this publication may be reproduced, stored in a retrieval system, or transmitted, in any form or by any means, electronic, mechanical, photocopying, recording or otherwise, without prior permission of the author.

Population dynamics in flows: numerical and theoretical investigations

PROEFSCHRIFT

ter verkrijging van de graad van doctor aan de
Technische Universiteit Eindhoven, op gezag van de
rector magnificus, prof.dr.ir. F.P.T. Baaijens, voor een
commissie aangewezen door het College voor
Promoties in het openbaar te verdedigen
op 25-06-2021 om 11.00 uur

door

Giorgia Guccione

geboren te Rome, Italië

Dit proefschrift is goedgekeurd door de promotoren en de samenstelling van de promotiecommissie is als volgt:

Voorzitter: prof.dr.ir. G.M.W. Kroesen
1st promotor: prof.dr. F. Toschi
2nd promotor: prof.dr. R. Benzi (Università degli Studi di Roma Tor Vergata)
Leden: prof.dr. G. Boffetta (Università degli Studi di Torino)
prof.dr. C. Storm
prof.dr. M.H. Jensen (University of Copenhagen)
dr.L. Giomi (LION Leids Instituut voor Onderzoek in de Natuurkunde)

Het onderzoek of ontwerp dat in dit proefschrift wordt beschreven is uitgevoerd in overeenstemming met de TU/e Gedragscode Wetenschapsbeoefening.

A mamma e papà

Contents

Introduction	1
1 Phenomenology and theoretical background	5
1.1 Population genetics and dynamics	6
1.2 Non-spatial populations	7
1.3 Spatially extended populations	10
1.4 Stochastic FKPP	12
1.5 Advective effects on population dynamics	13
1.6 Stochastic populations model	17
1.7 Interspecies Interactions	22
1.8 Bacterial motility and diffusion	25
1.9 Conclusions	26
2 Numerical methods	27
2.1 Wright-Fisher model	28
2.2 Moran model	29
2.3 Stepping stone model	30
2.4 Agent-based stochastic model	32
2.5 Conclusions	34
3 Discrete Eulerian model for population genetics and dynamics under flow	35
3.1 Method description	36
3.2 Numerical test in one dimension	39
3.3 Numerical test in two dimensions	42
3.4 Weak compressible flow in D=2	44
3.5 Conclusions	48

4	Strong noise limit for population dynamics in incompressible advection	49
4.1	Theory	51
4.2	Numerical approach	57
4.3	Comparison with analytical estimate	60
4.4	Conclusions	63
5	Pushed genetic waves	67
5.1	Theory	68
5.2	Deterministic transition and comparison with agent simulations	71
5.3	Effect of the source field	76
5.4	Incompressible flow	79
5.5	Conclusions	79
6	Concluding remarks and outlook	81
A	Diffusivity of E. coli-like microswimmers in confined geometries: The role of the tumbling rate	83
A.1	Methods	84
A.2	Weak confinement: Boundary accumulation	86
A.3	Strong confinement: Boundary escaping	89
A.4	Conclusions	91
	Bibliography	95
	Summary	103
	Curriculum Vitae	103
	Acknowledgements	109

Introduction

The current state of knowledge regarding evolutionary dynamics of marine species is closely connected with population genetics, that is the study of local variation of gene frequencies in a structured population. Each time the fitness of individuals depends on the relative abundance of phenotypes within a population, the field of evolutionary games is involved, which represents the competitiveness between species in a given environment. Marine environments encompass some of the most diverse ecosystems on Earth. One of the most extensively researched aspects of marine population genetics is the amount of genetic variation preserved in organisms. The forces of evolution that affect the distribution of alleles in populations are mutation, natural selection, gene flow, and genetic drift.

Planktonic organisms are microscopic marine photosynthetic individuals with sizes ranging from a few microns to several hundred microns and accounting for roughly half of all global primary productivity. They form the base of oceanic food webs and are responsible for most of the exchange of carbon dioxide between the atmosphere and the ocean [1, 2]. Due to this reason, phytoplankton play an essential role in the natural greenhouse effect. These tiny organisms are so crucial in the global carbon cycle, and even small changes in their productivity or in the relative abundance of the thousands of species could have a substantial influence on climate change [2].

Microorganism populations are carried along the uppermost layer (euphotic zone ~ 100 m) of the ocean [3]. The euphotic zone is characterized by a low quantity of nutrients due to consumption by phytoplankton. Periodic events, like upwelling and downwelling currents, supply nutrients to the upper water column. The aforementioned mechanisms can trigger the processes of water exchange in the mixed layer of the ocean. The upwelling current leads to a rise of deep water, where a rich concentration of nutrients resides. Passively transported microspecies are strongly influenced by the water circulation of the ocean, in fact, the convergence and the divergence of water masses allow them to experience the compressible turbulence [4].

Research Questions

In order to sustain our oceanic ecosystem, it is important to consider the physical factors variance which is tolerable by a population and how the population can keep on prospering in high Reynolds number fluid environments [5].

The focus of this thesis is to understand the role of compressible turbulence in shaping the fixation probability of a selective advantage population. This topic, which is relevant for population dynamics and evolution, has never been studied systematically and it is crucial to investigate how oceanic circulation may change life evolution.

In this regard, we have developed a new computational approach that merges the accuracy of considering a continuous space domain with the computational efficiency provided by a lattice-based model.

Thesis Outline

In chapter 1, the generalities of the genetic and the dynamics of populations are introduced. A brief overview regarding the population dynamics research field is given, in connection with the relevant study methodologies and developments performed over the years. The study is first carried out on well-mixed populations without considering dimensionality, and then it is applied to spatially extended populations. Beyond a deterministic approach, a stochastic model, based on Markov processes and concerning the dynamics of population dynamics under turbulent velocity flows is investigated.

In chapter 2, stochastic models for genetic evolution are accurately discussed. Species are made up of populations, a set of individuals genetically related. The study of genetic variation within a population deals with the biological differences affecting reproduction, feeding strategies, disease resistance, and many other factors. Among the several developed methods, we first mention the Wright-Fisher model that describes the process of genetic drift within a finite population size. The Moran model [6] is then examined, a simple approach that takes into consideration the selection of the organisms and the genetic drift. The Stepping Stone model [7] is introduced as an extension of the previous method, obtained by including the migration and reproduction of the individuals. The aforementioned models share many similarities with the ones used to investigate non-equilibrium phase transitions (see [8, 9]) and are tailored for lattice rules, and do not enable straightforward generalization by taking into account an external velocity advection. In Pigolotti *et al.* [10] an alternative method has been developed: the agent-based method, where each individual is advected by the external velocity, and diffusion is

implemented by a stochastic noise whereas death and reproduction processes are performed using an interaction distance δ . An extra computational cost is required to evaluate the individual numbers in each virtual δ -deme. This agent-based method has been recently used in Plummer *et al.* [11], where the competition between two different species, distributed in continuous space and under the effect of a compressible flow, is examined. It has been shown that a turbulent flow can dramatically change outcomes and can reduce the effect of selective advantage on fixation probabilities [11–13].

The original computational approach for researching the genetics of a large number of species is presented in the third chapter 3. The proposed procedure is an improvement of the origin off-lattice model described in detail in reference [4]. The improved method enables higher computational performance. The method is originally tested in one and two dimensions and subsequently, a weakly compressible velocity field is applied. This model sets the stage for the further studies presented in this dissertation.

In chapter 4, we discuss the case in which the population dynamics is within the strong noise limit. Without any advection and assuming molecular diffusivity for micron-ranged individual size, the strong noise limit can be achieved depending on nutrient abundances and sea temperature. Assuming that a strong noise limit is obtained without advection, the effect of ocean turbulence and the related eddy diffusivity should be taken into account. The Richardson theory is employed for such a purpose, together with the existing estimated rate of energy dissipation in the ocean, as discussed in reference [14]. Through the model introduced in the previous chapter, we investigate how the incompressible velocity field can modify the advantageous allele dynamics in a controlled case. In fact, we use a “cellular flow field” since the related computation of the effective diffusivity D_{eff} is known from references [15], [16], and [17]. In this controlled case, we provide theoretical predictions comparable with detailed numerical simulations. Once the correctness of our theoretical framework is established, a discussion is proposed in the conclusion section, on whether the “strong noise regime” may be relevant or not in oceanic situations.

The evaluation of the effect of stochastic fluctuations on antagonistic population dynamics and the exploration of the effect of external velocity on the principle of genetic dynamic is given in chapter 5. Deterministic effects are compared with the agent simulations for the initial population, with the aim of understanding the role of genetic fluctuations.

Finally, chapter 6 summarizes the key results of the studies mentioned in the preceding chapters. Thereafter, some possible outlooks are mentioned.

In appendix A the effective motility of a specific microorganism *E. coli like* is considered. We discuss the “run-and-tumble” motion of a flagellated *E. coli like* microswimmer under confinement. We simulate the flagellated microswimmer (*E. coli like*) by taking into account the complete hydrodynamic interaction of the microswimmer with the confining

walls as described by the Stokes equations endowed with appropriate boundary conditions at the interfaces.

1 | Phenomenology and Theoretical background

There has always been great interest in evolutionary theory, which seeks to understand what lies at the root of the genetic and dynamic variations within a population. The genetics of populations is driven by evolutionary forces that determine the genetic peculiarities of subsequent offsprings, whereas the population dynamics deals mainly with changes in population size and density for one or more species. The first modeling approaches have studied population dynamics neglecting the spatial structure. Subsequently, in order to extend the study to spatially inhomogeneous systems, reaction-diffusion mechanisms were introduced. Besides the Brownian diffusion, if species dispersal is biased due to a current flow, an advection term can be added to the previous mechanisms. Reaction-diffusion models are in themselves deterministic but can be derived as limits of stochastic processes, by applying the correct coarse-graining procedure.

1.1 Population genetics and dynamics

1

A **population** is a group of organisms belonging to the same species, that routinely interbreed while living in a particular area. Population genetics and population dynamics are long-standing and wide research areas in biology, mathematical physics, and more recently in statistical mechanics. Biological systems are dynamic and their mechanisms span several orders of magnitude in terms of considered space and time domains. These systems are governed by dynamic microscopic rules that give rise to complex macroscopic behaviors. Genetic diversity is fundamental to understand the interaction between the species and the surrounding environment. The individuals constituting a population often display different phenotypes and present different alleles of a particular gene. **Population genetics** is the study of genetic variation and seeks to understand how the frequencies of alleles and genotypes change over time, within and among populations, driving the adaptation. Population genetics expresses the heritable traits that enable the survival and reproduction of an organism in a given environment, it, therefore, explains the evolutionary factors that are the drivers of adaptation. Evolution is closely linked to the genetics of populations. In fact, it requires that populations' allele frequencies change with time. All the genes and their different alleles constitute the **genetic pool**. For the evolutionary process to take place, the allelic frequencies within the genetic pool need to change. The mechanisms of change are also known under the name of **evolutionary forces** and can account for all the genotypic variations. Among them, we can list mutation, natural selection, gene flow, and genetic drift. A schematic overview of these phenomena is presented below:

- **Mutation:** Alteration of genetic makeup so that a new variation of alleles is produced into a population.
- **Natural selection:** Principle according to which, each slight variation of alleles, if useful, is preserved [18].
- **Gene flow:** Transfer of genetic variation from one population to another, typically due to the migration of individuals.
- **Genetic drift:** Random change in the frequency of genes over time.

Population dynamics refers to the changes in the spatial density of species over time. The size of a population is affected by the per capita growth rate, which is the variation of the number of individuals, making up a population. Three factors influence the population dynamics: birth, death, and migration. Birth is the natural ability to add an individual to the existing population, as a result of reproduction. Death is the natural end of each organism's life and decreases the total amount of individuals. Migration refers to the

number of organisms moving into and out of populations, and it does not change the total number of considered individuals in the system.

Populations are defined through time and space. The spatial dimension concerns the distribution of organisms in space, whereas the temporal dimension relates to the variation of the spatial parameters over time. Spatial and time-based variations are affected by the system's biological properties and the occupied environment. The evolving nature of populations, implies knowledge of individuals' volume and composition at any given time and their changing properties, in order to perform a population dynamics study.

1.2 Non-spatial populations

For many decades, population dynamics was studied by means of the zero-dimensional approximation, in order to simplify the mathematical models of evolutionary processes. In a non-spatial description, it is assumed that in a given well-mixed population, composed of two or more species, interactions between any two individuals occur with the same probability [19]. This characterization, for which competition can occur between all the microorganisms present in the population, is a strong idealization. The organisms can also be far from each other, which means that the interaction is based on long-distance effects and the spatial structure becomes meaningless for the evolutionary dynamics.

1.2.1 Exponential and logistic population growth

The first model of the growth of a population without resource limitations is credited to Thomas Robert Malthus (1798) [20]. The main assumption of his "*Principle of population*" states that the rate of variation of the population $dp(t)/dt$ is proportional to the population $p(t)$.

$$\frac{dp(t)}{dt} = \mu p(t) \quad (1.1)$$

The constant of proportionality μ , also known as the Malthusian parameter, is the population growth rate. $\mu = b - d$ is the difference between the birth rate parameter b , and the death rate parameter d , where b and d are related to the considered species. The solution of the equation (1.1) results in the exponential Malthus's law:

$$p(t) = p(0)e^{\mu t}. \quad (1.2)$$

A dramatic growth in population size occurs when the growth rate μ is positive. In his work, Malthus argued that the growth of the human population cannot present an

exponential trend, otherwise, a shortage of food would occur as a consequence of the linear growth of good supplies. Indeed, uncontrolled infinite growth is not physical. In nature, populations cannot increase exponentially for a long time, as they will ultimately have to cope with limited food resources and available territory. In this regard, in 1836, Pierre Franois Verhulst proposed a revised model which would erase the unrealistic effects of endless growth [21], establishing the basis of the *logistic model*. In his theory, Verhulst considers factors affecting the growth rate, as for example the competition within a population. Competition is an interaction between organisms of the same species seeking similar resources, including limited food supplies or living space. Competition in a system with limited food supplies slows down the population growth, and can even cause saturation of the population size. The difference between the Malthusian exponential model and the logistic growth model is visually shown in fig. 1.1.

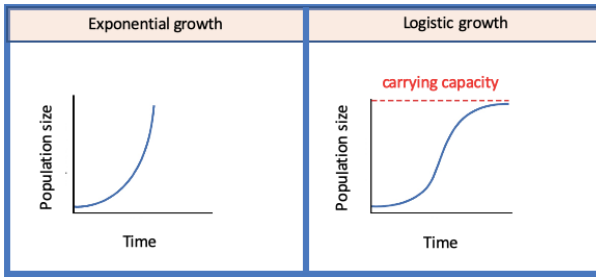


Figure 1.1: Comparison between exponential and logistic growth. The left graph shows an ideal environment case where the amount of resources is unlimited and populations grow at an exponential rate, resulting in a J-shaped curve. The logistic growth case is shown in the right graph. In this case the environmental factors limit the population growth and the population size levels off reaching the carrying capacity, producing a S-shaped curve.

The logistic population growth is expressed by the following equation:

$$\frac{dp}{dt} = \mu p \left(1 - \frac{p}{K} \right) \quad (1.3)$$

where K is defined as the maximum population abundance, or carrying capacity, for a given species. It is possible to rewrite the logistic differential equation (1.3) in terms of normalized population, by setting $c = p/K$

$$\frac{dc}{dt} = \mu c (1 - c) \quad (1.4)$$

The above equation (1.4) has two stationary solutions: an unstable equilibrium point at $c = 0$ and an asymptotically stable equilibrium point for $c = 1$ corresponding to the carrying capacity. As the time t becomes larger, any solution will tend towards the

equilibrium state at $c = 1$.

1.2.2 Kimura probability of gene fixation

Focusing on the simplest case of Darwinian dynamics for two competing populations, the pioneering works of Kimura [22], Kimura and Weiss [23], and Kimura and Ohta [24] provide a clear-cut answer in the well-mixed (zero-dimensional) case, i.e. neglecting any spatial structure of the population. Let us consider two different genotypes in a population, with concentrations c_A and c_B . Their evolution depends on the coexistence between the agent dynamics and the genetic drift, i.e. the deterministic and the stochastic contribution. It is not possible to determine a priori which one of the two species will be the dominant one in presence of turbulence, and a stochastic approach is needed for the evolution study. Well-adapted individuals with inherited favorable characteristics may survive and grow faster than others, passing on the genes that make them successful. Such organisms present a so-called **selective advantage**.

In absence of advection, Kimura [22], derived a theoretical prediction for the **fixation probability**, i.e. the probabilistic understanding of the eventual fate of new advantageous mutations. The fixation probability of new beneficial mutations plays a crucial role in the adaptation of populations in challenging environments. For the well-mixed case, the fixation probability can be expressed as:

$$P_{fix} = \frac{1 - e^{-sNf_0}}{1 - e^{-sN}}. \quad (1.5)$$

This formula (1.5) describes the fixation probability for a species with advantageous selection, s , in a population of size N , representing an initial fraction f_0 of all organisms. The space dependency is neglected in eq. (1.5), however, the result can be applied to spatially extended populations with simple migration patterns, such as diffusion [25]. The **fixation time** T_{fix} for small values of the selective advantage is given by the following relation [24]

$$T_{fix} = \frac{Nf_0}{\mu(1 - f_0)} \log\left(\frac{1}{f_0}\right) \quad (1.6)$$

where $1/\mu$ is the generation time, and it is assumed that no mutation occurs between the two different alleles.

1.3 Spatially extended populations

The theory described so far applies to systems varying through time only, and a homogeneous spatial distribution of the organisms is assumed. In a real ecosystem, most biological populations are inhomogeneously distributed in space and their dispersion rate plays a decisive role. The use of partial differential equations, known as **reaction-diffusion equations** represents a valid method for the quantitative description of spatially inhomogeneous systems.

1.3.1 The FKPP equation

A particular case of reaction-diffusion equations is the Fisher [26], Kolmogorov, Petrovsky, and Piskounov [27] equation, better known as FKPP equation¹. This equation is a natural extension of the logistic growth model and enables the description of the spatial propagation of an advantageous gene in a population $c(x, t)$.

The one-dimension FKPP equation is

$$\partial_t c = D \partial_{xx} c + \mu c(1 - c) \quad (1.7)$$

where D is the diffusion coefficient, μ is the reproduction rate, and 1 is the normalized carrying capacity of the system. The equation (1.7) describes a deterministic model for the density c of a population living in a given environment and with limited carrying capacity. The last term of the equation (1.7) is the non-linear reaction term generally presented as $f(c)$, it is controlled by the logistic growth dynamics and it has to satisfy the following conditions: $f(0) = f(1) = 0$ and $f(c) > 0$ for all $c \in [0, 1]$. Since the population has been normalized, the stable state corresponds to the full uniform population density, at $c(x, t) = 1$, while the unstable state $c(x, t) = 0$, corresponds to the spatially empty system.

1.3.2 Traveling waves

The FKPP equation (1.7) is particularly connected with the study of traveling waves. Precisely, its two steady solutions are connected through fronts whose motion describes the propagation from the state of full occupancy into the empty region. The evaluation of the stability of the stationary states determines the propagation direction of a front. The

¹For a mathematical description of the Fisher Kolmogorov equation, which has no general analytical solution, chapter 13 of the book “Mathematical Biology I” by Murray (2002) [21] can be consulted.

steady-state c is stable if $f'(c) < 0$ and unstable if $f'(c) > 0$.

In general, when a function is zero outside an $[a, b]$ interval, the function is said to be compact in that interval. The function that indicates an interval is a compact support function. In this case, the initial condition $c(x, 0)$ belonging to a certain interval between 0 and 1, presents a **compact support**. $c(x, 0)$ is a monotone decreasing function that terminates at $c = 0$ when at some finite spatial position $x(t)$. In other words, it means that the initial condition is sufficiently localized, and individuals are initially concentrated in a defined region and are absent in the rest of the territory. Traveling waves are defined as $c(x, t)$ solutions with translational symmetry, and their spatial profile remains constant while the wave propagates in space. Traveling waves are typically described by the following form:

$$c(x, t) = c(x - vt) = c(z) \quad (1.8)$$

Substituting the ansatz $z = x - vt$ into FKPP equation, we get

$$Dc_{zz} + vc_z + \mu c(1 - c) = 0 \quad (1.9)$$

where the propagation speed v has to be determined. This ordinary differential equation (1.9) establishes the shape of the front and satisfies the following boundary conditions:

$$\lim_{z \rightarrow -\infty} c(z) = 1 \text{ and } \lim_{z \rightarrow +\infty} c(z) = 0 \quad (1.10)$$

It is possible to convert the second-order differential equation (1.9) into first-order equation by defining $c' = F$ and $DF' = -vF - \mu c(1 - c)$. The introduced definitions lead to the phase-plane equation

$$\frac{dF}{dc} = \frac{-vF - \mu c(1 - c)}{DF} \quad (1.11)$$

whose steady states are $(c, F) = (0, 0)$ and $(c, F) = (1, 0)$ respectively. The critical point $(0, 0)$ is unstable if the velocity of the front approaches the value $v \geq v_{min}$, with $v_{min} = 2\sqrt{D\mu}$, for which there is a non-negative propagating wave solution. As a consequence, a range of front speeds is compatible with the linearized dispersal-reaction model. The minimum front speed v_{min} within this range is called the **critical speed**. A solution with front propagating at the minimum speed v_{min} occurs when the population is confined within some compact region.

1.3.3 Front propagation: *pulled* and *pushed*

The analysis of the front speeds can be broken down into two different situations classified as *pulled fronts* and *pushed fronts*. The stable state may propagate into an unstable state so that the front speed is established by the dynamics of the leading front edge [28].

For sufficiently sharp initial conditions with compact support, the front converges to the traveling wave with the minimal velocity $v = v_{min} + \mathcal{O}(t^{-1})$, although very slowly (*weak velocity selection*) [29, 30]. This solution of the classical Fisher equation is defined as a *pulled front*. Such fronts are typically pulled along by the growth and spread of small perturbations around the unstable state, in the leading edge where $c \ll 1$. This velocity can change due to the discreteness of the model. In fact, the presence of a discrete process in both time and space at the leading edge makes the Fisher wave speed lower if compared to the deterministic speed. An estimation by Brunet and Derrida [31] of how the Fisher wave value differs from the continuum wave speed was given:

$$v \sim \sqrt{D\mu} \left[2 - \frac{\pi^2}{(\ln N)^2} \right]. \quad (1.12)$$

Notice from eq. (1.12) that the convergence to the continuum limit is slow as $N \rightarrow \infty$.

In the case of the *pushed front*, the wave speed is determined by the nonlinear growth in the region behind the leading edge, forcing the front to go faster with regard to the critical front $v > v_{min}$. This effect is called *strong velocity selection*.

1.4 Stochastic FKPP

Since eq. (1.7) depicts the dynamics as a deterministic process, it does not take into account the fact that populations are composed of a discrete number of individuals exhibiting stochastic fluctuations. For spatially extended populations, where the space-independent ingredients of competing species are mainly the fitness (the perpetual increase of growth rate), the carrying capacity, and the diffusivity, it is convenient to express the evolutionary dynamics in terms of macroscopic density $f(\vec{x}, t)$ which carries one of the two alleles. In the continuum limit, the equation of the dynamics reads:

$$d_t f = D\Delta f + \mu s f(1 - f) + \sqrt{\frac{2\mu f(1 - f)}{N_R}} \eta(\vec{x}, t). \quad (1.13)$$

The first term on the r.h.s of eq. (1.13), represents the molecular diffusion D acting on the population dynamics, the second term is the effect of small advantageous selection s , and the third term corresponds to genetic fluctuations due to birth and death processes (see [10] for a detailed derivation of eq. (1.13) where with N_R and $\eta(\vec{x}, t)$ are respectively indicated the density number of individuals and the white noise δ -correlated in space and time.

1.5 Advective effects on population dynamics

Many biological populations composed of microorganisms live and compete in liquid media, like rivers, lakes, or oceans. These microorganisms need to find a way to thrive in high Reynolds number fluid environments. The classical spatial model for growth presented in eq. (1.7) can be generalized to investigate the dynamics of populations under the effect of an advecting flow, taking into account the transport resulting from the flow field $u(x, t)$.

$$\partial_t c + \partial_x(u c) = D \partial_{xx} c + \mu c(1 - c) \quad (1.14)$$

where c is the continuous variable describing the concentration of microorganisms, D is the diffusion coefficient and the last term corresponds to the reaction term, controlled by the logistic growth with rate μ . The advective velocity and the front propagation are closely related. The impact of the advection is investigated by assuming that the left part of the considered unidimensional spatial domain is inhabited whereas the right is empty. Without velocity field, the front would propagate towards the right direction, admitting traveling wave solutions with constant speed $v_F = 2\sqrt{D\mu}$ and front width w on the order of $\sqrt{D/\mu}$ [30]. It is now assumed a front propagating from right to left side in the presence of advection. The flow affects not only the expansion process but can also have a dramatic impact on the population's chance of survival in the habitat. The solution of eq. (1.14) for a one-dimensional homogeneous system, with a constant velocity of absolute value u , is simply given by a change with the reference frame. In this case, due to the presence of an adverse flow, the propagation velocity is reduced by u , so that the front propagates with the velocity $v'_F = v_F - u$. On the contrary, the two speeds sum up when the flow is supporting the growth, producing a front propagating with increased speed $v'_F = v_F + u$. The sign of the reduced propagation velocity determines the persistence of the species: a negative propagation speed leads to an elimination of the population, whereas a positive propulsion speed causes the invasion of the empty habitat [32]. Therefore, on an infinite habitat in an advecting flow, the population can survive only if $u \leq v_F = 2\sqrt{\mu D}$. The equation (1.14) can change according to the velocity field and is not easily analytically interpreted. It is not trivial, for instance, the analysis of the case where a compressible flow $\partial_x u \neq 0$ is present. In many studies, this equation has been investigated as a model for describing populations of microorganisms in turbulent flows, without neglecting inertial effects [5, 13]. The presence of a flow causes the movement of the individuals from the initial condition and represents also a vehicle for nutrients. The applicability of the reaction-diffusion-advection model relates to several living species with geometrical sizes ranging over many order of magnitude. The considered case of diffusion of passive microorganisms suspended in a liquid is related to the Brownian diffusion. As a final remark, the FKPP equation expresses the deterministic evolution of a population but it tends to neglect stochastic fluctuations that are particularly relevant

for small populations especially at the leading edge of the front.

1.5.1 Turbulent Flows

Most relevant flows in nature are turbulent. Observations of this type of motion are common in everyday life. The smoke of a cigarette, the mixing of coffee and milk in a cup, a whirling motion of a torrent, are just some of the countless possible examples. The turbulent motion is identified as a non-stationary, irregular and apparently, chaotic motion, characterized by the presence of eddies of different sizes and speeds, which are constantly changing. From a mathematical point of view, the concept of turbulence is identified with the chaotic behavior of the solutions of the Navier-Stokes equations.

1.5.2 Navier-Stokes equations

The motion of an incompressible fluid flow is governed by the Navier-Stokes equations:

$$\nabla \cdot \mathbf{v} = 0 \tag{1.15}$$

$$\partial_t \mathbf{v} + (\mathbf{v} \cdot \nabla) \mathbf{v} = -\frac{1}{\rho} \nabla p + \nu \nabla^2 \mathbf{v}$$

where v is the velocity field, p the pressure of the flow, ρ the density of the fluid, and ν the kinematic viscosity. The first relation identifies the mass conservation of the incompressible fluid and the second equation represents how the fluid's momentum changes due to pressure and dissipative forces. If an external force acts on our system, it is possible to define the rate of energy input and energy dissipation in a turbulent flow. Hereafter we shall denote the scale of magnitude which estimates the ratio of inertial forces to viscous forces within a fluid which is subject to relative internal movement due to different fluid velocities.

1.5.3 Reynolds number

To establish whether the motion of a viscous fluid is laminar or turbulent, a dimensionless quantity called Reynolds number is defined:

$$Re \approx \frac{LU}{\nu} \tag{1.16}$$

This parameter depends on the average speed U of the fluid, on the viscosity ν , and a linear quantity L characteristic of the duct. It has been experimentally demonstrated that, for a fluid flowing around a sphere, the regime is laminar for Re values below $2 \cdot 10^5$ and turbulent for values above. Therefore, for large Re , the non-linearities of the Navier-Stokes equations are dominant. This causes the absence of the analytical solution of the N-S equations and outlines the irregularity of the flow. In this regime, only statistical models can adequately describe the flow.

1.5.4 Laminar vs turbulent flows

In laminar flows, fluid layers slide in parallel with no eddies, swirls, or currents normal to the flow itself. Turbulent flows, on the other hand, include vortex structures of different sizes and speeds that make the flow unpredictable over time even if the motion remains deterministic. Motion, in fact, is governed by the laws of the deterministic chaos which implies full knowledge of the behavior of the system starting from its initial conditions. The deterministic nature of these systems does not make them predictable, every deterministic solution is unstable and a small uncertainty in the initial condition is enough to observe similar but different behaviors over time. This behavior is known as chaos. An example of the laminar and turbulent flows around a sphere is shown in fig. ??.

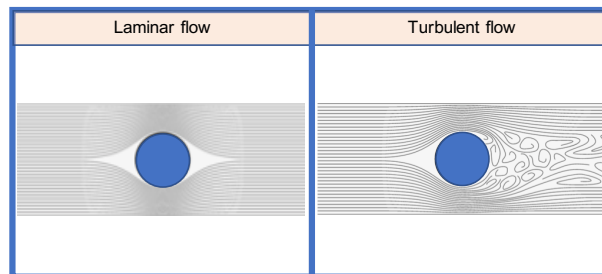


Figure 1.2: Laminar and Turbulent flow patterns over a sphere

As a clarifying example, let us consider two solutions having two slightly different initial conditions, $x(0)$ and $x(0) + E(0)$. After a few time steps, the two solutions behave totally differently. We denote by $x_1(t)$ the value returned by the initial condition $x(0)$ and by $x_2(t)$ the value obtained from $x(0) + E(0)$. We define $E(t)$ as the absolute value of the difference between the two tracer particles $|x_1(t) - x_2(t)|$. The distance $E(t)$ will be, shortly thereafter, an apparently random number ranging from 0 and 1. No matter how small $E(0)$ may be, after a few steps, it is impossible to predict the x trajectory. This

notion can be expressed by the Lyapunov exponent [33]:

$$E(t) = E(0) \exp^{\lambda_L t} \tag{1.17}$$

The sign of the Lyapunov exponent indicates the behavior of the nearby trajectories. A negative exponent $\lambda_L < 0$ indicates that neighboring trajectories converge to the same trajectory. In the limit where $\lambda_L > 0$ and $E(0)$ is infinitely small, the motion shows a strong dependence on the initial condition. When this occurs, the system develops a **chaotic motion**. Given the laws that describe the system, if the motion is chaotic, there is a time limit beyond which a prediction is not possible. The fraction $1/\lambda_L$, in eq. 1.17, represents the predictability time of the system. It can be concluded that after that time it is no longer possible to predict the state of the system starting from the initial condition. Keeping this in mind, it is remarked that a quasi-periodic motion is not chaotic even if it never reproduces exactly itself.

1.5.5 Richardson energy cascade

The nature of turbulent flow is highly dissipative. In the Richardson cascade picture, swirling structures are formed by providing energy from external forces to a fluid system. These vortices spin-off a cascade of nested smaller vortices. The large eddies are unstable and break up, transferring their kinetic energy to smaller eddies. These smaller eddies undergo a similar break-up process and transfer their energy to yet smaller eddies. The mechanism proceeds until the small-scale structures are small enough for the fluid’s molecular viscosity to convert their kinetic energy into heat.

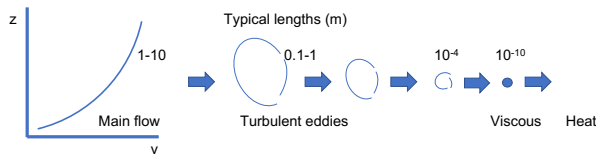


Figure 1.3: Sketch of Richardson cascade process: *Big whorls have little whorls which feed on their velocity and little whorls have lesser whorls and so on to viscosity*
- Lewis fry Richardson

Figure 1.3 shows the energy transfer through cascaded whirls, including typical geometries.

1.5.6 Kolmogorov's theory

The description of Richardson's energy cascade, first quantified by A.N. Kolmogorov [34], is the most fundamental concept of turbulence theory.

Kolmogorov postulated that for sufficiently high Reynolds number, the small scale eddies are isotropic. This assumption is very important because it implies that the statistical analysis of small eddies is independent of any specific geometry. Under this hypothesis, Kolmogorov statistically described the main features of the smallest turbulence scale (known as "Kolmogorov microscales") as follows:

$$\text{length scale} \quad \eta = \left(\frac{\nu^3}{\epsilon} \right)^{1/4} \quad (1.18)$$

$$\text{dissipative time scale} \quad \tau_\eta = \left(\frac{\nu}{\epsilon} \right)^{1/2} \quad (1.19)$$

$$\text{velocity scale} \quad v_\eta = (\nu \epsilon)^{1/4} \quad (1.20)$$

where ϵ is the mean rate of energy dissipation and ν is the kinematic viscosity. An alternative definition of the dissipative scale is the local Reynolds number of the Kolmogorov scale

$$Re = \frac{LU}{\nu} \approx \frac{\eta v_\eta}{\nu} = 1 \quad (1.21)$$

Although the speed of energy dissipation fluctuates in space and time in the turbulence of fluids, at microscale we tend to use the average values of the fields since they represent the typical values of the smallest scales in a given flow. The study performed by Kolmogorov in 1941 forms a theory of the medium field since it assumes the average energy dissipation rate as the relevant dynamic parameter.

1.6 Stochastic populations model

In this section, we introduce the stochastic analysis that characterizes the evolution of a population in a heterogeneous system, more accurately than the deterministic model. A population composed of discrete elements whose growth occurs based on unpredictable events will be considered. From a qualitative point of view, this approach can modify macroscopic observables such as the propagation speed.

Several stochastic models have been developed to explore genetic drift. The considered intrinsic fluctuations become very relevant when the population size is small. This can happen in the proximity of an expanding front or when the population size is reduced due to compressibility-based effects.

1

1.6.1 Compressible Turbulence

Given a fluid volume, the divergence is defined as the percentage variation of that volume per unit time. A positive divergence refers to a volumetric dilation while a negative divergence is connected with a volume contraction. It is therefore intuitive to think that, since the total mass contained in the volume must remain unchanged, a dilatation causes a decrease in density whereas a contraction produces an increase in density. Previously it has been remarked that the divergence of the velocity field is zero for incompressible fluids by looking at the Navier-Stokes equations eq. (1.15). As a consequence, a fluid is *incompressible* when the density is constant. A *compressible* flow, on the contrary, holds account of the effect of fluctuations, namely as the relative volume change in response to a pressure change. Competing organisms can be mixed and compressed by turbulent movement. When population dynamics is combined with compressible turbulence, the system can be described in terms of the dimensionless number τ_η/τ_g i.e. the ratio between the biological and the flow time scales. $\tau_\eta \equiv (\nu/\epsilon)^{1/2}$ is the Kolmogorov dissipative time scale, with ν the kinematic viscosity and ϵ the rate of energy dissipation per unit mass, whereas $\tau_g \equiv (1/\mu)$ is the growth time.

Compressible turbulent flows may exhibit **weak or strong compressibility**. In the *weak compressibility* case, the time scale of the turbulent flow is relatively large if compared to the generation time of the particles, and $\tau_\eta \gg \tau_g$. The effect of the flow is considered almost negligible and then the particles cannot experience the turbulence.

At the limit where $\tau_\eta \ll \tau_g$, the effect of the fluid flow plays a significant role. This regime is defined as a *strong compressibility* regime and results in a system that is completely governed by turbulence and where only a small number of particles can survive. Strong compressibility is responsible for the clustering of biological entities [35]. The particles are transported to the sinks (areas of negative divergence) where they tend to die due to competition effects. That is why in this regime, the total size of the population is strongly reduced. Clustering implies a reduction of the biological mass and enhancement of the effects associated with number fluctuations.

1.6.2 Evolutionary dynamics of two species

The evolutionary dynamics of the two species depends on the coexistence between the replicator dynamics and the genetic drift, with both deterministic and stochastic contributions. We will start by analyzing the neutral case $s = 0$, in a one-dimensional system, for the densities $c_A = N_A/N$ and $c_B = N_B/N$ in an advecting field $u(\vec{x}, t)$ [12]. The macroscopic equations describing the evolution of the densities are:

$$\begin{aligned} \partial_t c_A + \partial_x(uc_A) = & D\Delta c_A + \mu c_A(1 - c_A - c_B) + s\mu c_A c_B + \\ & + \sqrt{\mu \frac{c_A}{N}(1 + c_A + c_B)} \eta_A(x, t) \end{aligned} \quad (1.22)$$

$$\begin{aligned} \partial_t c_B + \partial_x(uc_B) = & D\Delta c_B + \mu c_B(1 - c_A - c_B) - s\mu c_A c_B + \\ & + \sqrt{\mu \frac{c_B}{N}(1 + c_A + c_B)} \eta_B(x, t) \end{aligned} \quad (1.23)$$

with $\eta_A(x, t)$ and $\eta_B(x, t)$ Gaussian noises, δ -correlated in time and space that must be interpreted using Ito calculus [7, 36].

The above equations derive from a microscopic equation through the Kramers-Moyal method, the order of such description is equivalent to the van Kampen inverse system size expansion [37].

1.6.3 Doering's probability fixation formula

A rather nontrivial result was obtained by Doering in a remarkable landmark paper [38], in which he showed that the probability of fixation P_{fix} for the stochastic FKPP equation, in one spatial dimension, does not depend on diffusivity D , at the limit of small values of dispersion and large total population size:

$$P_{fix} = 1 - \exp \left[-sN \int dx f(x, t = 0) \right] \quad (1.24)$$

where $f(x, t = 0)$ is the initial spatial distribution of the fraction of a determined species. The same outcome seems to hold for the two-dimensional case, with $d = 2$, according to the numerical investigations presented by [10, 25].

1.6.4 Strong noise limit

In spatially extended systems, the populations are mixed by diffusion. The diffusion scale $\sqrt{D/\mu}$ may be considered as an "effective deme size". This means that individuals within a distance smaller than $\sqrt{D/\mu}$ are mixed very efficiently over a single generation, and appear decoupled when the distance is larger than $\sqrt{D/\mu}$. For the one-dimensional problem, we have derived the velocity of the front v_F from the Fisher equation in absence of noise. However, this is applicable only at the limit of weak noise, i.e. $N\sqrt{\frac{D}{\mu}} \gg 1$, that corresponds to having many individuals in an effective deme size. By adding a noise term to the FKPP equation, Doering, *et al.* [38] considered the limit $N\sqrt{\frac{D}{\mu}} \leq 1$, where fluctuations play a decisive role. This limit is characterized by small values of D and N and is called a **strong noise regime** (or weak growth limit).

The behavior of the velocity of a stochastic front seems to go according to $v \sim D\mu N$, a much smaller quantity than the so-called Fisher velocity $v_F \sim \sqrt{D\mu s}$ observed for $N \ll 1$. We will discuss in chapter 4, how the slowing down of the front propagation and the segregation effects induced by genetic fluctuations (see [7]) can explain the reason for which P_{fix} is independent of D .

The total concentration c is uniform over the domain ($c = 1$), when a population is subject to the advection of an incompressible flow velocity field \vec{v} . In this case, the equation becomes

$$\partial_t f + \vec{v}\vec{\nabla} f = D\Delta f + \mu s f(1 - f) + \sqrt{\frac{2\mu f(1 - f)}{N_R}} \eta(\vec{x}, t) \quad (1.25)$$

where \vec{v} is assumed to be a two-dimensional incompressible flow with $div(\vec{v}) = 0$. Now, we summarize some of the key findings obtained in chapter 4. Without advection, the strong noise limit occurs when the following inequality holds:

$$\frac{a^2}{N_0 D} \gg \frac{1}{\mu} \quad (1.26)$$

where $a \equiv L/n$ is called the *deme* size, with $N_R \equiv N_0/a^2 = n^2 N_0/L^2$ the population density. The physical interpretation of eq. (1.26) is rather clear: $a^2/(N_0 D)$ is the diffusive characteristic time needed for a population of size N_0 to spread over a distance of the order of a , whereas $1/\mu$ is the generation time. Competition in space occurs at a much slower rate when the inequality in eq. (1.26) is satisfied. Consequently, the characteristic

timescale of the system slows down, and the fixation time T_{fix} is given by

$$T_{fix} = \frac{L^2}{D} \frac{f_0}{1-f_0} \log\left(\frac{1}{f_0}\right) \quad (1.27)$$

which can be compared to eq. (1.6), with D/L^2 replacing μ/N .

In presence of advection, a proper analysis can be performed by considering the effective (or eddy) diffusivity, D_{eff} , due to the flow, and the related characteristic spatial scale, l_u . Both D_{eff} and l_u are not easily computable starting from the knowledge of the advection field. In a few cases, as discussed in this section, it is possible to obtain an analytical estimate for both quantities (see [39] for details). In chapter 4, we will provide theoretical and numerical evidence that there may exist a strong noise scenario for the dynamics if the following inequality is fulfilled:

$$\frac{l_u^2}{D_{eff}N_0} \gg \frac{1}{\mu} \quad (1.28)$$

Moreover, we find that the relation $a^2/D > l_u^2/D_{eff}$ is always valid. When eq. (1.28) is satisfied, the corresponding estimate of T_{fix} , for small s , is given by

$$T_{fix} = \frac{N_T l_u^2}{D_{eff}N_0} \frac{f_0}{1-f_0} \log\left(\frac{1}{f_0}\right) \quad (1.29)$$

where $N_T = n^2 N_0$ is the total population size. Note that T_{fix} , given by eq. (1.29), is shorter than the one given by eq. (1.27), but still much larger than the fixation time for a well-mixed population given by eq. (1.6).

1.6.5 Damköhler number

The relation $D_{eff} \sim U_0 l_u$ holds for the relatively simple case of chaotic flows with U_0 being some typical velocity. Then (1.28) can be written as:

$$Da \equiv \frac{\mu l_u}{U} \gg N \quad (1.30)$$

where Da is called the Damköhler number and represents the ratio between the rate of growing and the characteristic rate of population spreading (see also [15, 16] for the study of thin front propagation in steady and unsteady cellular flow and no genetic fluctuations, i.e. $N \rightarrow \infty$). For finite $Da \gg N$, strong noise effects characterize the dynamics in the

presence of chaotic advection.

In the case of $D_{eff} \sim Ul_u$, the ratio l_u/U is defined as the "eddy turnover time" at scale l_u of the flow. If the flow is characterized by a single spatial scale l_u , eq.(1.30) becomes a condition on the velocity scale U . However, for turbulent flows, the eddy turnover time increases with l . The system behaves as in the well-mixed case for small values of l (turbulence increases mixing and no strong noise effects can arise), however, there may exist a critical scale above which strong noise effects becomes relevant and the characteristic timescale of the Darwinian dynamics increases.

1.6.6 Heterozygosity

Heterozygosity is a measure of genetic variation within a population [7] and quantifies the loss of diversity in a population composed of two genotypes. The heterozygosity in the one-dimensional case can be expressed as

$$H(x, x'; t) \equiv \langle 2f(x, t)[1 - f(x', t)] \rangle. \quad (1.31)$$

The heterozygosity is given by the product of the two fractions $f(x, t)$ and $(1 - f(x', t))$ and defines the probability for two randomly selected individuals to belong to different species (that is carrying two different alleles) [10]. The heterozygosity becomes zero when one of the two genotypes fix. In 1970, Crow and Kimura [40] stated that if the population size is not very small ($N \gg 1$), the total heterozygosity decays exponentially in well-mixed neutral systems:

$$\langle H(t) \rangle = H(0) \exp\left(-\frac{t}{2N}\right) \quad (1.32)$$

The relation (1.32) indicates that after $2N$ generation time the expected heterozygosity becomes the initial value $H(0)$ divided by the factor e^{-1} . Thus, in a one-dimensional system, the local diversity $H(t) \equiv H(x, x'; t)$ decays according to $t^{-1/2}$ in the case of a neutral model without mutation. In two dimensions, this decay is much slower and behaves as $1/\ln(t)$ [7].

1.7 Interspecies Interactions

An interpretation of the interspecies interaction of microorganisms is fundamental to provide an understanding of biological diversity. However, classical ecological competitiveness models ignore populations spatially extended. This type of population is treated as

well-mixed organisms that freely interact with each other. Coexistence in such a setting is highly limited [41, 42] and biodiversity is significantly diminished. In fact, if the range of interaction is limited, individuals never compete against the whole population. In [43], it is shown that this reduced interconnection suppresses the selection. Therefore, the conventional theory of well-mixed systems overestimates the probability of fixation of beneficial species. The analysis of species interplay aims to look for models and constraints which affect the evolution of interactions and the conditions which support coevolution. Diversity is much greater, in spatially heterogeneous settings, and one of the substantial insights consists of the manner space can improve the coexistence of the organisms. In this regard, spatially extended mathematical models, as the reaction-diffusion equations are considered.

Such an analysis has acquired importance only in recent years, becoming a new focus of evolutionary research. Typically, every species has a peculiar trait and the interaction of two species can be described in general terms as mutualism, predator/ prey competition, and antagonism as shown in fig. 1.4.

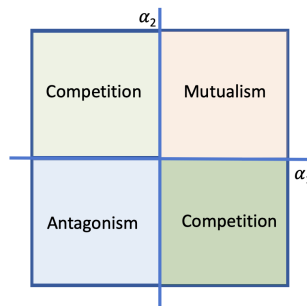


Figure 1.4: Representation of the four different competition scenarios of the species. The point in the center where $\alpha_1 = \alpha_2 = 0$ indicates the neutral evolution.

- **Mutualism** : $(+, +)$, in which both species benefit from the interaction.
- **Competition**: $(+, -)$, $(-, +)$ in which one species benefits at the expense of another one.
- **Antagonism**: $(-, -)$ in which the two species bear a cost of mutual interaction.

The antagonistic interaction can occur in a very wide range of geometrical scales. For example, the reproduction between a fire-bellied toad (*Bombina bombina*) and the yellow-bellied toad (*B. variegata*), can generate hybrids, which are considered selectively disadvantaged combinations [44]. Proceeding towards smaller dimensions, we find populations of micron-scale bacteria poison-secreting. Such antibacterial toxin production

is widespread in microbial cultures and may have significant effects on the environment as well as on human health [45–47].

1

In chapter 5 we model two antagonistic strains in a two-dimensional system. For this purpose we focus on the dynamics of two species A and B having different growth rates, μ_A and μ_B , respectively. We take a thin layer of individuals at carrying capacity, so that A -individuals have fraction f and B individuals have a fraction $(1 - f)$. In order to model the antagonistic interaction, we assume that the growth rates depend on the local fraction of the other species,

$$\begin{aligned}\mu_A &= \mu_A^0 + \alpha(1 - f) \\ \mu_B &= \mu_B^0 + \beta f\end{aligned}\tag{1.33}$$

in which the base growth rates are represented by the apex 0 and, where α and β are the amplitudes of the fraction-dependent contributions for both the strains. To ensure that the two species have mutually antagonistic interaction, we take $\alpha, \beta \leq 0$. In such a way they incur a penalty for growth as either species expand next to each other. As we have seen in [48], the established interactions create a dynamical "tension line" γ between the two species. It can be shown that the two strains separate faster in their components for smaller negative values of α and β . According to the work by Lavrentovich we can define $\delta = \alpha - \beta$ and $\sigma = -(\alpha + \beta)/2$, and consequently $\gamma \approx \gamma(\sigma)$, i.e. the line tension is a monotonically increasing function of σ . Making use of equations (1.22) and (1.23) we find the two equations describing the evolution of two spatially extended fractions:

$$\begin{aligned}\frac{\partial c_A}{\partial t} + \nabla(\vec{u}(r)c_A) &= D\Delta c_A + \mu c_A(1 - c_A - c_B) + \\ &\quad -\mu c_A c_B(\sigma - \delta/2) + \sqrt{\mu \frac{c_A}{N_0}(1 + c_A + c_B)}\end{aligned}\tag{1.34}$$

$$\begin{aligned}\frac{\partial c_B}{\partial t} + \nabla(\vec{u}(r)c_B) &= D\Delta c_B + \mu c_B(1 - c_A - c_B) + \\ &\quad -\mu c_A c_B(\sigma + \delta/2) + \sqrt{\mu \frac{c_B}{N_0}(1 + c_A + c_B)}\end{aligned}\tag{1.35}$$

where N_0 is the number of individuals per deme.

1.8 Bacterial motility and diffusion

Motility is a non-trivial factor in the fitness and viability of bacteria. Motility determines the manner in which microorganisms scout the environment, seeking food and avoiding predation. [4, 10]. For swimming bacteria, the motion is characterized by frequent tumbling events which allow the microorganism to explore a vast portion of the surrounding space [49–51].

1.8.1 Run-tumble propulsion

An organism, to keep moving at low Reynolds number, must execute cyclic deformations that break time-reversal symmetry (or non-reciprocal motion) [49, 52]. In a liquid environment, evolution has selected a number of different swimming strategies exploiting cilia or flagella [53–55]. A typical strategy employs rotating flagella driven by a motor embedded in the cell membrane. The motor is able to switch between clockwise and counter-clockwise rotation. In the case of *Escherichia coli* and *Salmonella typhimurium*, flagella are randomly distributed on the cell surface. However, when all the motors rotate in the same direction, the flagella arrange in a single bundle at a pole of the cell [56]. The steady tail rotation thrusts the microorganisms in the “run” phase, in which the bacterium moves in a smooth forward motion. The run phase is frequently interrupted by tumbling events. For *E. coli*, during the tumbling phase, one of the motors reverses the rotation. Consequently, the flagellum bundle unwraps, and the microorganism stops and changes its orientation. Then, as all the motors resume to rotate in the same direction, the flagella aggregate again into a single bundle and a new run phase starts. The overall motion is named “run-and-tumble” and it is represented in fig. 1.5.

For run and tumble swimmers, in free space, the trajectory during the run phase is approximately a straight line. It follows that the increase of the tumbling frequency α corresponds to a reduction of the effective diffusion coefficient D . Indeed, by assuming that the run phase is characterized by a typical constant velocity v_0 and that tumble events occur instantaneously, the effective diffusion coefficient scales as $D \simeq l^2 \alpha$, with $l = v_0/\alpha$ the distance covered during a run phase. Hence, $D \simeq v_0^2/\alpha$, see e.g.[57].

1.8.2 Bacterial dispersion in microfluidic channels

A completely different phenomenology is observed when flagellated *E. coli* like microorganisms move close to a solid wall or to an air-liquid interface. Microswimmers are attracted towards the boundaries via hydrodynamic interactions [58–62], and in the

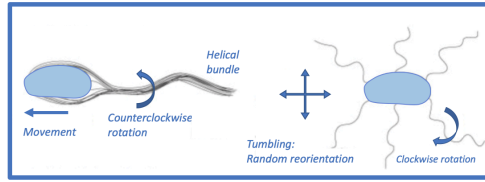


Figure 1.5: *E. coli* switch the frequency of CCW (run) vs CW (tumble) rotation of their flagella based on their sensing

case of solid surfaces, may get trapped in stable circular orbits parallel to the wall. This deterministic motion prevents bacteria to explore the surrounding space. In this condition, the role of tumbling events is twofold. On one hand, as in free-space, a high tumbling frequency hampers the bacterium to swim away for long distances, on the other hand, tumbling favors the escape from the stable circular orbits. An analysis of a simplified model suggests that the diffusion coefficient reaches a maximum value for a tumbling frequency $\alpha \simeq \tau^{-1}$, being τ the characteristic time scale associated with the stable circular orbit [63].

1.9 Conclusions

This chapter provides an overview of the population dynamics and genetic properties. A general explanation of the mechanisms that affect genetic diversity over time is given. In fact, population genetics forms the fundamental basis of evolutionary change, which is the modification of hereditary characteristics of groups of organisms through the generations. To determine the evolution of a population, several fundamental processes such as the influence of the environment and the reciprocal interaction between the different alleles should be taken into account. To understand the mechanisms at the basis of the genetic diversity over time, two different approximations are analyzed: non-spatial and spatial. Firstly a deterministic approach is studied, which although simple is not realistic. Addressing most of the research questions present in evolutionary biology requires random effects to be taken into account, and a stochastic approximation results more appropriate. For the considered case, the resulting evolution does not depend on the given initial condition but only on the probability to exhibit certain dynamics.

2 | Numerical methods

The evolution of complex biological systems out of equilibrium is usually studied by means of stochastic models. Sewall Wright and Ronald Fisher have developed the first stochastic population model intending to study the genetic drift process [64, 65]. These models have laid the groundworks for the theory of population genetics, enabling important follow-up studies and further models still referenced today. The most relevant models are described in the next section, to create a clear link between the state of the art and the research choices proposed in this work.

Large portion of this content refers to the review of Korolev et. al [7]

2.1 Wright-Fisher model

The *Wright-Fisher* model describes the process of genetic drift within a finite population. Consider a population in equilibrium composed of N diploid individuals. Each diploid individual can contain either the same allele or two different alleles, namely A and B . According to the deterministic model, the relative frequency of type A is given by $p = i/2N$ where the index i is related to the number of types A allele at step t . We consider the case where the alleles A and B are evenly fit. The $2N$ alleles, composing the considered population at time t , may give birth to a causal number of offspring making up the next generation at the time $t+1$. An allele copy from the initial population is randomly chosen and a duplicate of that allele is found in the new generation. It is assumed that no mutations occur. Suppose further that once the new generation is formed, the previous one is completely replaced. In light of these assumptions, the generations do not overlap, since N genes die and other N genes are born at each time step (see fig. 2.1).

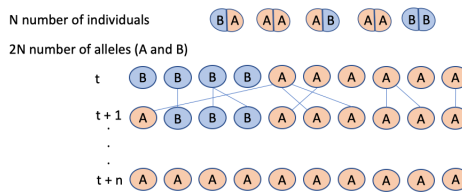


Figure 2.1: Structure of the Wright-Fisher model. The population is characterized by $2N$ alleles. The new generation of $2N$ allele copies is produced through a binomial sampling of the old generation's genetic pool. The sampled offspring alleles may be assembled into a new set of diploids, or else used to calculate a new generation of binomial sampling.

We are interested in calculating the exact probability that the number of A allele copies, i remains equal to $2pN$ after a generation of random sampling. This is given by the binomial distribution:

$$p_{ij} = \binom{2N}{j} p^j (1-p)^{2N-j}, \quad 0 \leq i, j \leq 2N \quad (2.1)$$

where $\binom{2N}{j} = \frac{2N!}{j!(2N-j)!}$ gives the binomial coefficient. p_{ij} indicates the transition probability within one generation. Equation (2.1) determines the probability for an allele with i copies in the first generation to be found in j copies in the next generation. After one step the probability is given by the number of A allele copies j over $2N$, $p(1) = j/2N$.

One would expect that since at the first step the relative fitnesses of the alleles A and B are the same, also their frequencies should stay constant over the generations $p(t+1) = p(t)$. What one notices is that allele frequencies increase and decrease over time by chance.

This mechanism is defined as genetic drift, by which random sampling of descendants allows the allele frequencies to change their deterministic expectations.

In case the whole population is reproducing, then the variance of the frequency of the A allele in the next generation $t + 1$, can be obtained by the variance equation $\sigma^2(\Delta p) = \frac{p(1-p)}{2N}$. In the most likely case where not all the individuals are involved in the reproductive process, the variance of the change in the gene frequency is given by the relation: $\sigma^2(\Delta p) = \frac{p(1-p)}{2N_e}$, where N_e represents the effective population size, i.e. the number of breeding individuals among the idealized population. In particular, the coefficient N_e is a population genetic metric used to evaluate the effect of genetic drift in the finite population on allele frequencies. Individuals in the *Wright – Fisher* model simultaneously reproduce at every time step. This behavior may lead to an overestimated genetic drift effect. We now introduce a model where only one individual reproduces at a time over generations.

2

2.2 Moran model

The *Moran model* represents a finite-population stochastic process and describes the evolution of a population forward in time. This method differs from the previous one due to the possibility of overlap between different generations, and it is a very effective approach to model the *birth* and *death* events of the individuals.

The description, in the simplest version (without selection or mutation), is the following: A population consisting of N individuals possibly carrying two alleles A and B is considered. At every discrete time step, an organism is randomly selected for reproduction and another one for dying [66], thereby preserving the overall number of individuals. Each new individual inherits the type of its parent and replaces a randomly chosen individual (possibly its parent). This sampling procedure results in genetic drift. It is common to keep track of the population only at discrete points in time when a birth-death event has occurred. Time is therefore measured by the number of events that occurred rather than in chronological time.

Let us define the frequency $p(t)$ as the fraction of species A with respect to the total population of size N , at time t . The expected value of this frequency at time $t + 1$ and the variance of $\langle p(t + 1) \rangle$ will be respectively:

$$\langle p(t + 1) \rangle = p(t) \quad (2.2)$$

$$\langle [p(t + 1) - \langle p(t + 1) \rangle]^2 \rangle = \frac{2p(t)[1-p(t)]}{N^2} \quad (2.3)$$

where angular brackets represent average concerning the individual chosen at random for reproduction and death. Since, at every time step, only one individual of the entire population gives birth, the time t is measured as generation time τ_g/N . The two mentioned equations (2.2) and (2.3) point out that the frequency $f(t)$ behaves as an unbiased random walk in the space of allele frequencies, with a frequency-dependent diffusion coefficient. It is possible to outline that this random walk, in a continuum regime, follows the Fokker-Planck equation [40, 67]

2

$$\frac{\partial P(t, f)}{\partial t} = \frac{\mathfrak{D}_g}{2} \frac{\partial^2}{\partial f^2} [f(1-f)P(t, f)] \quad (2.4)$$

where $P(t, f)$ is the probability density function for f at time t , measured in generations and $\mathfrak{D}_g = \frac{2}{N\tau_g}$ is the genetic diffusion constant.

2.3 Stepping stone model

The *Stepping Stone Model* (SSM) is introduced with a simple but clarifying visual example shown in fig. 2.2. Two populations p_x and p_y are considered, living on a mainland and an island, respectively. The mainland and the island are represented by the two cylinders and it is assumed that only the x -population can migrate on the island (fig. 2.2). The overall population given by the sum of p_x and p_y individuals is denoted by N . The frequency p of y -population living on the island after a time step t is given by the following relation:

$$p_{y,t+1} = mp_{x,t}(1-m)p_{y,t} \quad (2.5)$$

where m is the fraction of immigrants and $(1-m)$ is the fraction of individuals already present on the island (see fig. 2.2).

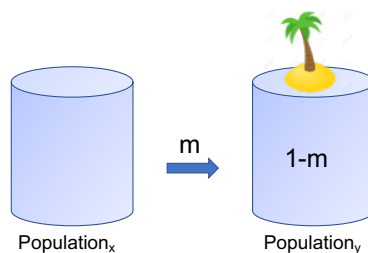


Figure 2.2: Basic mainland-island example. The two cylinders represent the mainland and the island. Within them a population of N individuals is present. Only the migration, illustrated by the m parameter, from the mainland to the island is possible.

The SSM, introduced by Kimura [23, 68], is a more realistic discrete model for spatial growth. It considers a one-dimensional domain discretized into an infinite number of islands, called *demes*, consisting of many well-mixed populations. Every site is saturated up to its carrying capacity, and consequently, the local population size N is constant during the whole dynamics. The island deme can be sub-divided into multiple demes to create a linear spatial lattice. In sketch fig. 2.3, three sub-demes are considered and marked by the indices $l - 1, l, l + 1$ indices, representing adjacent locations on the spatial lattice. Two different allelic variations of organisms are present in each sub-deme. The connection between the neighboring populations is given by the migration rate, m . Since the migration rate is divided between the two closest demes, it corresponds to $\frac{m}{2}$.

The number of sub-demes can be extended up to infinite to treat the system with a continuous approach. The evolutionary state of the system depends on the macroscopic density of individuals $f(x, t)_l$ carrying one of the two alleles, within the l deme, and is well described by the following stochastic differential equation in the considered continuum case:

$$\frac{df_l}{dt} = \frac{m}{2}(f_{l-1} + f_{l+1} - 2f_l) + s f_l(1 - f_l) + \sqrt{\mathcal{D}_g f_l(1 - f_l)} \Gamma_l \quad (2.6)$$

where s is the selective advantage, Γ_l represents a zero-mean white Gaussian noise that obeys to $\langle \Gamma_{l_1}(t_1) \Gamma_{l_2}(t_2) \rangle = \delta_{l_1} \delta_{l_2} (t_1 - t_2)$ and it must be interpreted using Ito's calculus [7]. Each population presents a stochastic change in allele frequencies at each generation, that may be due to genetic drift and other local processes.

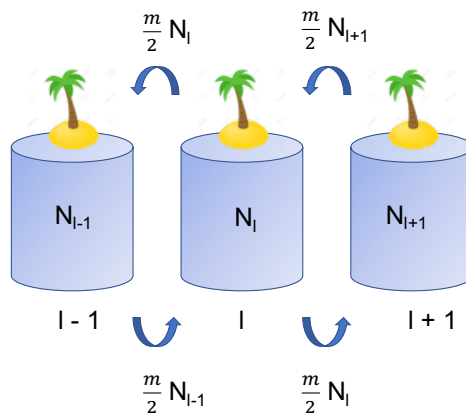


Figure 2.3: An infinite one-dimensional stepping stone model. Each population, which consists of N organisms is connected to only two others and exchange migrants at a rate of $\frac{m}{2} N$ in each direction each generation.

Mutation terms can be added to (2.6) to describe the continuous time and space limit of the SSM thanks to the stochastic Fisher-Kolmogorov-Petrovsky-Piscounov equation [26].

2.4 Agent-based stochastic model

2

The agent-based stochastic model (ABM) or individual-based model, enables the understanding of the dynamics of a complex system starting from the study of the single agents composing the system. All organisms are treated as independent individuals interacting with each other and with the surrounding environment.

In the models introduced so far, the spatial movement of the individuals was mainly due to the diffusion process. Furthermore, the discrete nature of the individuals living in a population and the stochastic behavior of the related evolution have been neglected.

Extending population dynamics research beyond a deterministic viewpoint provides an opportunity to combine the current understanding of microorganism systems with complementary studies. In this regard, the stochastic continuum dynamics of a population can be investigated by involving the intrinsic fluctuations in the study approach. Such a broadening of perspectives opens important routes towards the study of all the organisms that live in the ocean, all the existing allelic variants, and the underlying chaotic flow.

Due to the presence of the flow and its inhomogeneities, one of the central aspects of the *Stepping Stone model*, namely, the constant size of the local population in time or in space [5], is lacking.

The ABM model can catch both the discrete nature of the particles and the stochastic features of their interactions. The individual-based model coupled with the flow, developed by Perlekar in 2011 [69], is here described. A spatial one-dimensional mesh of size L is subdivided into intervals of size δ and n particles are equally distributed within the intervals. For simplicity, only particles having two different allele variations, called A and B , are considered. Within each interval, there are N_A and N_B individuals with allele variation A and B , respectively. The total number of individuals, inside a deme, is defined by $N = N_A + N_B$. The particles are advected by the flow and diffused by the Brownian motion according to

$$x_i(t + \Delta t) = x_i(t) + u\Delta t + \sqrt{2D\Delta t}\Gamma_i(t) \quad \text{with } i=1,2,\dots,n \quad (2.7)$$

where u is the advecting velocity, Δt is the time step, and $\Gamma(t)$ is a normally distributed random variable with zero mean and unitary variance. Furthermore, the particles inside the sub-domain δ can reproduce themselves, die or compete with other neighboring

particles, at a certain rate k . The set of these processes, known also as *logistic dynamics* is summarized in table 2.1. All of these processes may possibly happen with the opposite

$A + B \xrightarrow{k} B + B$	Occurs when two particles, with different alleles, interact with each other, and one of the two particles changes species, at a rate k . In order to implement this event, it is necessary to know the number of particles of one of the two species within the range δ . If the relation $kN_B\Delta t > r_t$ is valid, where r_t is a random number uniformly distributed in $[0, 1]$, then the process occurs.
$A \xrightarrow{k} A + A$	In this reaction a particle A reproduces itself, giving birth to another particle of the same type. It occurs if the relation $k\Delta t < r_t$ is fulfilled.
$A + A \xrightarrow{k} A$	An interaction between two particles of the same species takes place, and one of the particles dies at rate k . This occurs if the relation $k(N_A - 1)\Delta t < r_t$ is true.

Table 2.1: Agent-based model logistic dynamics.

species, by modulating, where it is needed, the number of individuals with the right allele in the relations. In the case of one species only, these mathematical expressions would refer to Doering’s birth-coagulation reactions [38].

In a recent work of Plummer et al., [11] a one-dimensional agent-based model of two-species competition is implemented for a well-mixed system, which is coupled to a compressible flow. The employed birth-death relations that were used are the following:

$$A \rightarrow A + A \quad \text{at rate } \mu; \quad A \rightarrow \emptyset \quad \text{at rate } \gamma(N_A - 1) + \lambda_{AB}N_B \quad (2.8)$$

$$B \rightarrow B + B \quad \text{at rate } \mu; \quad B \rightarrow \emptyset \quad \text{at rate } \gamma(N_B - 1) + \lambda_{BA}N_A \quad (2.9)$$

The growth rate μ and the death rate γ are the same for both the species in the above equations (2.8) and (2.9). This means that the well-mixed carrying capacity of each species is the same. However, the rate of the death process for the competition can vary, allowing the definition of the selective advantage s as

$$s = 1 - \frac{\lambda_{AB}}{\gamma} \quad (2.10)$$

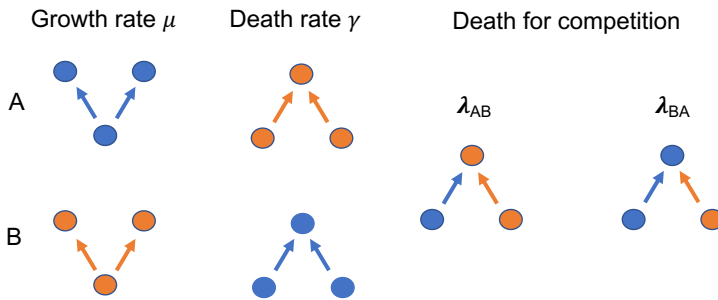


Figure 2.4: Visual draft of the processes that take place: reproduction, death, and competition.

Very often, the relation $\mu \rightarrow \mu(1 + s)$ can be found, for one of the species, to which corresponds to faster growth.

2.5 Conclusions

Multiple population models that reflect environmental variables have been analyzed since cell fitness values depend not only on their cell types but also on their location. A good approximation of the biological evolution of a mutant with fitness $s + 1$ in a population having fitness 1 is given by the works of Wright-Fisher and Moran for unstructured genetic populations (dimension $d = 0$). The evolutionary dynamics is mainly discussed through the stochastic equation of Fisher Kolmogorov Petrovsky, Piscounov (sFKPP) with geographically organized populations. The stepping stone model allows a first stochastic discussion by hypothesizing a well-mixed population where organisms carrying different alleles migrate across an infinite array of demes. A common feature of the discussed models is the fixed total population size, which does not change through subsequent generations. To enable a more generic study, the agent-based method is introduced, which lays the foundations for the explanation of the method proposed in this dissertation. It relies on the stepping stone model, inserts rules for the processes of birth and death, and for the first time takes into account variations in density.

3 | Discrete Eulerian model for population genetics and dynamics under flow

Fluid advection can seriously impact genetic competition among biological species living in marine surroundings. Both the off-lattice agent-based architecture (see Chapter 2) and the novel method proposed in the current chapter, based on the density in loco, are used to define the dynamics of two competing populations under (turbulent) velocity fields in one and two spatial dimensions.

The proposed algorithm is initially described and tested in one and two dimensions without flow. A systematic comparison of our approach against known analytical and numerical results is given. Then the fixation probability of an advantageous species in the case of two-dimensional weakly compressible flows is investigated.

Part of this chapter is based on the review “A novel, accurate, and efficient model for population dynamics and genetics in marine environments” by G. Guccione et al. [70]

3.1 Method description

The proposed computational approach is here described. A one-dimensional (1D) system with periodic boundary conditions is considered. The system consists of a uniform lattice of size L , discretized in n intervals of size $\Delta x = L/n$. Each interval $i = 1, \dots, n$ spans the region $x \in [(i-1)\Delta x, i\Delta x]$. We denote by $N_i^{(\beta)}$ the number of individuals in the interval i , where $\beta = A, B$ refers, in this case, to the two possible species (for different realizations, the number of the species may also be greater). At equilibrium and with no external flow, we can define the density N_0 of individuals per mesh point corresponding to the overall carrying capacity $N_0 L / \Delta x$. With this definition, we can also think of N_0 as the average carrying capacity for a mesh site.

3

At time t , our knowledge is given by the set of numbers $N_i^{(\beta)}$ for $i = 1, \dots, n$. Our task is to compute the evolution of the system at time $t + \Delta t$, where Δt represents our time step.

We implement the evolution using four different steps. In step 1, we implement a Markov chain with next-neighbor hopping and periodic boundary conditions, which is known to be consistent with the diffusion equation with diffusivity D once the hopping probability is given by the relation

$$p \equiv \frac{D\Delta t}{\Delta x^2}; \quad (3.1)$$

with $p \ll 1$.

Step 1. Diffusion. For each interval i , we compute the particle positions $x_a(i)$ ($a = 1, \dots, N_i$) according to the rule:

$$x_a(i) = \left(i - \frac{1}{2}\right)\Delta x + \Delta x \left(\eta - \frac{1}{2}\right)(1 + 2p), \quad (3.2)$$

where η is a random number that is uniformly distributed $[0, 1]$. In this step, only a small fraction of the N individuals is spread outside of the initial site i . Note that we do not assume any knowledge of the previous position of the individuals.

Step 2. Advection. Once step 1 is performed, we can compute the advection and obtain

$$x_a(i, t + \Delta t) = x_a(i) + u(x_a(i))\Delta t \quad (3.3)$$

where $u(x, t)$ is a prescribed advecting field.

Step 3. *Relabeling*. For each off-mesh particle a , we can now determine the deme index,

$$j \equiv \left\lfloor \frac{x_a(i, t + \Delta t)}{\Delta x} \right\rfloor + 1 \quad (3.4)$$

and therefore apply the rule

$$\tilde{N}_j = \tilde{N}_j + 1 \quad (3.5)$$

to increment the deme occupancy number. Note that before implementing eq. (3.2) we put $\tilde{N}_j = 0$ for all demes $j = 1, \dots, n$.

Since from Step 1 to Step 3 we repeat the same operation for both species in the sections, we ignore the label β for the different species.

Step 4. *Birth and death processes*. After running step 1 to step 3 for all the intervals, we apply the last step where we execute the rules for stochastic population dynamics for each segment j . At this stage, for every j interval, we compute the birth-death process \tilde{N}_j times according to the following rules:

$$\tilde{N}_j^{(A)} = \tilde{N}_j^{(A)} + 1 \quad \text{at rate } r_b(A) \quad (3.6)$$

$$\tilde{N}_j^{(A)} = \tilde{N}_j^{(A)} - 1 \quad \text{at rate } r_d(A) \quad (3.7)$$

$$r_b(A) = \mu \Delta t$$

$$r_d(A) = \mu \Delta t \frac{\tilde{N}_j^{(A)} - 1 + \tilde{N}_j^{(B)}(1 - s)}{N_0}$$

$$\tilde{N}_j^{(B)} = \tilde{N}_j^{(B)} + 1 \quad \text{at rate } r_b(B) \quad (3.8)$$

$$\tilde{N}_j^{(B)} = \tilde{N}_j^{(B)} - 1 \quad \text{at rate } r_d(B) \quad (3.9)$$

$$r_b(B) = \mu \Delta t$$

$$r_d(B) = \mu \Delta t \frac{\tilde{N}_j^{(B)} - 1 + \tilde{N}_j^{(A)}(1 + s)}{N_0}$$

where s is the selective advantage, $s > 0$, or disadvantage, $s < 0$, of individuals A with respect to B . Here, r_b and r_d denote the *birth* and the *death* probability, respectively. Note that for each mesh site, the probability to obtain k new offspring or deaths is binomial and it approximates a Poisson distribution only when the number of individuals considered in the specific process is large enough. This is never the case near the edge of a propagating front and/or near extinction even for a large value of N_0 .

At the end of step 4, we can put $N_j^{(\alpha)} = \tilde{N}_j^{(\alpha)}$ and we can start with a new time step.

Let us now briefly comment on our method. The effect of advection does not change the number of particles, i.e., it is conservative. Thus neglecting, for the time being, the death-birth process, we obtain the equation for each species,

$$\partial_t N(x, t) + \partial_x(u(x, t)N(x, t)) = D\Delta N. \quad (3.10)$$

The birth-death process is the same one implemented in Ref. [11].

On the other side, ignoring diffusion and advection and neglecting terms of the order of s/N_0 inside the noise term [10], step 4 gives

$$\frac{dN_A(t)}{dt} = \mu N_A \left(1 - \frac{N_A + N_B}{N_0}\right) + \mu s \frac{N_A N_B}{N_0} \quad (3.11)$$

$$+ \sqrt{N_A \mu \left(1 + \frac{N_A + N_B}{N_0}\right)} \eta_A(t)$$

$$\frac{dN_B(t)}{dt} = \mu N_B \left(1 - \frac{N_A + N_B}{N_0}\right) - \mu s \frac{N_A N_B}{N_0} \quad (3.12)$$

$$+ \sqrt{N_B \mu \left(1 + \frac{N_A + N_B}{N_0}\right)} \eta_B(t)$$

where η_A and η_B are independent delta correlated in time Wiener processes. Upon defining $c_A = N_A/N_0$ and $c_B = N_B/N_0$ and introducing the advection and diffusion, the final equations of motion read:

$$\partial_t c_A + \partial_x(u c_A) = D\Delta c_A + \mu c_A(1 - c_A - c_B) \quad (3.13)$$

$$+ s\mu c_A c_B + \sqrt{\mu \frac{c_A}{N_0} (1 + c_A + c_B)} \eta_A(x, t)$$

$$\partial_t c_B + \partial_x(u c_B) = D\Delta c_B + \mu c_B(1 - c_A - c_B) \quad (3.14)$$

$$- s\mu c_A c_B + \sqrt{\mu \frac{c_B}{N_0} (1 + c_A + c_B)} \eta_B(x, t)$$

Finally, assuming that $c_T \equiv c_A + c_B \sim 1$ everywhere and upon denoting $f = c_A/c_T$, we obtain

$$\partial_t f + u(x, t)\partial_x f = D\Delta f + s\mu f(1 - f) + \sqrt{\frac{2\mu f(1 - f)}{N_0}} \eta(x, t). \quad (3.15)$$

We remark that the statistical properties of the system are invariant upon the scaling: $\mu \rightarrow 1$, $D \rightarrow \frac{D}{\mu}$, $t \rightarrow t\mu$, which is equivalent to working in units of generation time.

3.2 Numerical test in one dimension

In this section, we introduce some numerical tests confined to one-dimensional systems. Going back to what was discussed in subsections 1.3.1, 1.3.2 and 1.3.3, we briefly summarize below some salient aspects. First, we need to solve the Fisher-Kolmogorov-Petrovsky-Piscounov (FKPP) equation that describes the space-time evolution of a population in a reaction-diffusion system. In one space dimension, it reads

$$\partial_t c = D \partial_{xx} c + \mu c(1 - c), \quad (3.16)$$

where $c(x, t)$ is a continuous variable that identifies the concentration of individuals, D is the diffusion coefficient, and μ is the growth rate. The uniform solutions of eq. (3.16) are $c = 1$ and $c = 0$ for a stable and unstable state, respectively. In 1995, Mueller and Sowers [71] showed that for $\mu > 0$, the traveling wave solutions to eq. (3.16) are always characterized by a *compact support property*. We can set up initial conditions that depend on c as follows: $c(x, 0) \rightarrow 1$ as $x \rightarrow -\infty$ and $c(x, 0) \rightarrow 0$ as $x \rightarrow +\infty$. For this kind of boundary conditions, we can find a continuous family $c(x, t)$ of traveling wave solutions of the form

$$c(x, t) = c(x - vt), \quad (3.17)$$

where v is the velocity of the traveling wave and $c(x, t)$ is a function that must satisfy the following ordinary differential equation

$$Dc'' + v c' + \mu c(1 - c) = 0, \quad (3.18)$$

with conditions : $c(-\infty) = 1 \quad c(\infty) = 0.$

Around the unstable state, $c(x, 0)$, the velocity of the front approaches the deterministic continuum minimum value $v_{min} = 2\sqrt{D\mu}$. At this minimum speed, the fronts are called “pulled fronts” which are pulled along by the growth and spreading of small perturbations in the leading edge where $c \ll 1$. Small perturbations in traveling waves arise due to the randomness associated with discrete events in both space and time such as birth and death processes. Thus we expect that the observed value of the Fisher wave velocity propagation is lower than the deterministic one. Brunet and Derrida [31] gave an estimation of that value as

$$v \sim \sqrt{D\mu} \left[2 - \frac{\pi^2}{(\ln N)^2} \right]. \quad (3.19)$$

From eq. (3.19), one can clearly observe that the convergence to the continuum limit is extremely slow as $N \rightarrow \infty$. Fluctuations have been considered by Doering, *et al.* conjecture [38] adding a noise term to the FKPP equation; for the strong noise regime

(or weak growth limit), they found that the speed value goes according to

$$v \sim D\mu N. \quad (3.20)$$

In fig. 3.1 the normalized Fisher wave speed versus the number of individuals per site N_0 is shown. There are two theoretical estimates, corresponding to the weak and strong noise limits. The simulations, identified by dots, are consistent with the theoretical lines: with 10 particles per site, the strong noise regime is found and the Fisher velocity is about ~ 0.3 times greater than the theoretical estimates. In this work, simulations are performed in the weak noise regime, where the velocity of the genetic wave v_g is $\simeq v_{min}$.

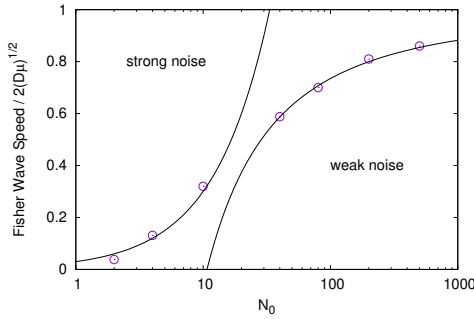


Figure 3.1: Algorithm convergence tests: Fisher wave behavior varies with the number of individuals per site. It is possible to distinguish two theoretical limits: on the left, the strong noise trend, and, on the right, the weak noise one. We performed simulations for $\mu = 10$ and $D = 0.001$; the circles indicate the results of our simulations that are, asymptotically, in very good agreement with the theoretical lines.

The diversity of a population composed of two genotypes in one dimension is measured by the heterozygosity [7],

$$H(x, x'; t) \equiv \langle f(x, t)[1 - f(x', t)] \rangle. \quad (3.21)$$

This quantity is given by the product of the two fractions $f(x, t)$ and $(1 - f(x', t))$ and it defines the probability that two selected individuals, chosen at random, are from different species (carry different alleles) [10]. For homogeneous conditions, $H(x, x'; t)$ depends on the $r = |x - x'|$. The heterozygosity becomes zero when there is the fixation of one of the two genotypes. Moreover, it is known that in a one-dimensional system, $H(t) \equiv H(x, x; t)$ decays in time as $t^{-1/2}$. In fig. 3.2, we have tested this theoretical prediction using our methods with $N_0 = 50$ on the domain with periodic boundary conditions discretized on a 512 mesh point: the result very clearly confirms the theoretical behavior. Next, to further validate the algorithm, we calculate, in the absence of advection,

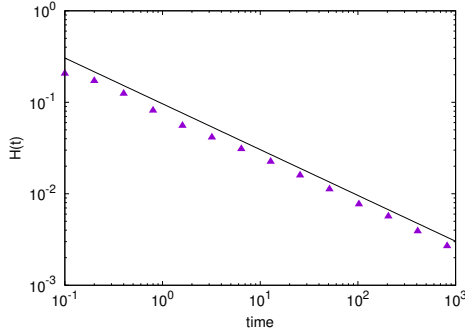


Figure 3.2: Log-log plot of the decay of one-dimensional local heterozygosity, $H(t)$, as a function of time. The black continuous line shows the theoretical heterozygosity in 1D, $t^{-1/2}$, and the purple symbols show our simulations. The error bar is calculated on 500 cases and the variance is smaller than the symbol size.

the fixation probability is given by

$$P_{fix} = \frac{1 - e^{-sNf_0}}{1 - e^{-sN}}. \quad (3.22)$$

In fig. 3.3, different panels corresponding to a different number of individuals per box are shown. In our simulations, we focus on small selective advantages, in order to study more realistic cases. Our results are in good agreement with the theoretical predictions (continuous black lines, in the figures).

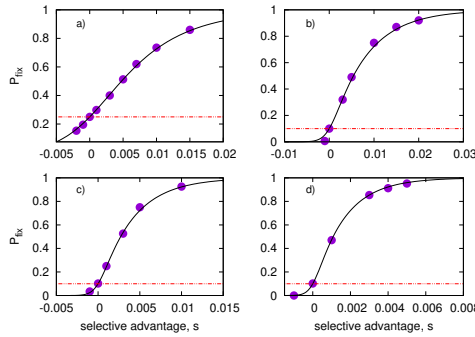


Figure 3.3: Fixation probability of one species, in a one-dimensional domain, vs different values of the selective advantage. In each plot, the Kimura formula is reported (black solid line) by fixing N_0 , the number of particles per site, and f_0 , the initial fraction of a species (red dashed line). Our no-flow results for the fixation probability are illustrated with the solid circles; the lines and the results are in very good agreement for every case. The length of the domain of size $L = 2\pi$ is divided into 128 intervals. The values of N_0 and f_0 for each graph are (a) $N_0 = 4$, $f_0 = 0.25$; (b) $N_0 = 10$, $f_0 = 0.1$; (c) $N_0 = 20$, $f_0 = 0.1$; (d) $N_0 = 50$, $f_0 = 0.1$. N in eq. (3.22) is $128 N_0$.

3.3 Numerical test in two dimensions

In this section, we implement the method previously introduced (Sec. II) and validated for a one-dimensional system on a two-dimensional configuration. Following the same schematic procedure of the 1D case, we start by estimating the heterozygosity parameter. It is known that in two spatial dimensions, the local heterozygosity decay in time is slower compared to 1D: it goes to zero as $H(t) \sim 1/\ln(t)$ [7, 10]. To check whether our method is able to exhibit such (slow) decay, we specifically perform a set of numerical simulations with $N_0 = 20$ on a domain with periodic boundary conditions and 256^2 mesh point. In fig. 3.4, such slow logarithmic decay is appreciable. In this figure, we plot $1/H(t)$ versus time. Note that starting with well-mixed conditions, $H(0) = 1/4$. Therefore, $1/H(t)$ is 4 at $t = 0$ and grows in time as $\ln(t)$, as shown in the figure. The loss of the genetic variability given by our simulations (purple triangles) is in agreement with the theory (black solid line).

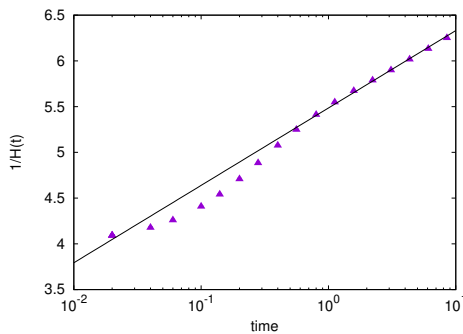


Figure 3.4: Behavior in the log-linear scale of the inverse of the heterozygosity, $1/H(t)$, as a function of time in 2D. The symbols, representing the results of our simulation results, are in good agreement with the black solid line that indicates the theoretical trend, $\frac{1}{H(t)} \sim \ln(t)$.

The second step, as in the numerical validations in 1D, is to verify Kimura's formula, given by eq. (3.22), for the two-dimensional system in the absence of advection. The formula for the probability of fixation is still valid for higher dimensions and our results together with the theoretical prediction (solid black line) show an unequivocal agreement in fig. 3.5.

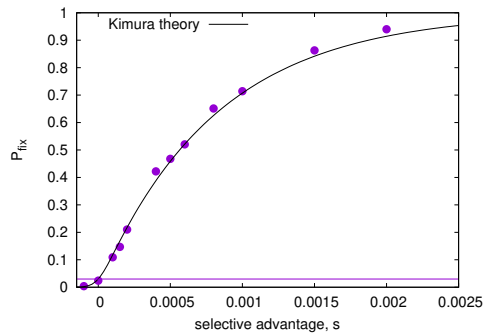


Figure 3.5: Probability of fixation as a function of the selective advantage in the absence of advection. Simulations are performed on a 64×64 lattice with, initially, 10 individuals per box, a diffusion coefficient of $D = 0.01$, and an initial fraction of $f_0 = 0.03$ (horizontal red dashed line). Our no-flow results for the fixation probability are illustrated with the solid circles and the theoretical prediction of Kimura by the solid black line.

3.4 Weak compressible flow in D=2

Before adding an advecting velocity field to our two-dimensional system, we briefly discuss the main results achieved by Plummer *et al.* [11], where a particular configuration of the velocity field was used, given by

$$u(x) = u_0 \sin\left(x - \frac{\pi}{2}\right). \quad (3.23)$$

For small enough u_0 , the flow field in (3.23) is weakly compressible, i.e., the condition $c_A + c_B = 1$ is valid within a small percentage (up to 4 percent for $u_0 = 0.05$ on a domain size 2π). We will test whether, as in 1D, the Kimura formula is still valid provided we define N as effective population size, N_{eff} . For $s \rightarrow 0$, it has been shown in [11] that N_{eff} depends only on the diffusion constant D , u_0 , and on the maximum number N_0 of individuals per site. The crucial point is to recognize that near to the source, one can define a characteristic scale, $l_s = \sqrt{D/u_0}$. Any organism that moves significantly farther than l_s from the source is unlikely to be able to return and has, therefore, a negligible chance of fixation as it is drawn into the sink. It follows (see [11] for details) that N_{eff} can be estimated as

$$N_{eff} = B_1 \rho_0 \sqrt{\frac{D}{u_0}} \quad (3.24)$$

where B_1 is a constant of the order of unity and ρ_0 is the density at each point, namely $N_0/\Delta x$.

Following [11], one simple way to understand the physical meaning of eq. (3.24) is to consider the deterministic case, i.e., eq. (3.15) in the limit $N_0 \rightarrow \infty$, and assume an initial population $f = 1$ in a small box Δ at the location x_0 , and zero otherwise. Then, the population, whose spatially averaged initial ratio is $\bar{f}_0 \equiv \langle f_0 \rangle = \Delta/L$, where $L = 2\pi$, evolves to an asymptotic value, $f_\infty(x_0) = \lim_{t \rightarrow \infty} f_t(x_0)$, which depends on x_0 . The ratio $f_\infty(x_0)/\bar{f}_0$ is a function of x_0 and shows a Gaussian-like behavior in terms of $x_0 - x_s$, where x_s is the position of the source with a variance proportional to l_s and $f_\infty(x_s)/\bar{f}_0 \gg 1$. This is equivalent to saying that for $s = 0$, there is a significant advantage for the offspring occurring near the source and a strong disadvantage for those occurring downstream. This implies that the effective population size (for small s) is the one corresponding to the population size close to the source, i.e., at a distance l_s from the source. Following [19], one simple way to understand this result is to consider a simple toy model on a linear graph where the source is a relative ‘‘cold’’ site (node of the graph) with respect to the downstream ‘‘hot’’ sites, where ‘‘cold’’ and ‘‘hot’’ refer to the probability for an offspring to be advected by the external flow using the same language of [19].

The same considerations can be made for the two-dimensional version of the same problem. For this purpose, we consider the following flow

$$\begin{aligned} u(x) &= u_0 \sin\left(x - \frac{\pi}{2}\right) \sin y \\ u(y) &= -u_0 \sin\left(x - \frac{\pi}{2}\right) \cos y \end{aligned} \quad (3.25)$$

with periodic boundary conditions and a domain of size $(2\pi)^2$. In fig. 3.6, the final fraction of the initially localized species $f_\infty(x_0, y_0)/\bar{f}_0$ is shown where, now, $\bar{f}_0 = \Delta^2/(4\pi^2)$. Two peaks are clearly visible in correspondence with the sources, representing the upwelling regions. The asymptotic value of f_∞/\bar{f}_0 is increasing in the proximity of the sources while being it is reduced moving away from them.

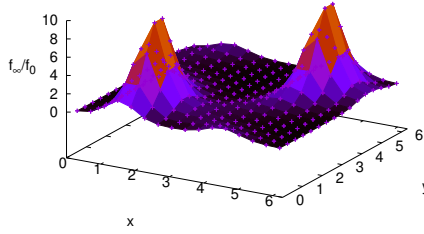


Figure 3.6: Shape of the asymptotic fraction, $f_\infty(x,y)$, normalized by the initial fraction, \bar{f}_0 . Populations starting close to the source become increasingly larger.

In fig. 3.7, we show, with a black line, a one-dimensional section (along the y axis) of the two-dimensional behavior of f_∞/\bar{f}_0 . Since for $s = 0$ $P_{fix} = \bar{f}_0$, one can consider the black line as the increase in P_{fix} due to the effect of the velocity field near the source. To validate this interpretation, as well as the quality of our method, we performed a series of numerical simulations with $N_0 = 2$ at $s = 0$ using the same initial conditions of the deterministic simulations. After estimating the fixation probabilities, we compute the increase of P_{fix} as a function of the initial position, x_0 . The results are shown as symbols in fig. 3.7 where an excellent agreement is visible with the deterministic value of f_∞/\bar{f}_0 . This result demonstrates that the mechanism described in [11], for small enough s should be true for the two-dimensional flow considered here. Based on the previous results, we can generalize eq. (3.24) for the two-dimensional case as follows:

$$N_{eff} = 2B_1^2 \rho_0 \frac{D}{u_0} \quad (3.26)$$

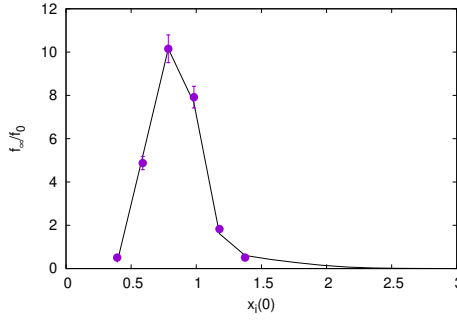


Figure 3.7: Enhancement effect due to the presence of a source. Comparison between numerical simulation P_{fix}/\bar{f}_0 (symbols) and the deterministic line f_∞/\bar{f}_0 (solid black line). For this simulation we implement 250 cases with a diffusivity of $D = 10^{-2}$, two particles per site with a grid base of 64×64 , and a velocity of $u_0 = 0.05$. The error bar is calculated on 250 cases.

3

The factor 2 in eq. (3.26) comes from the fact that for our flow field, given by eq. (3.25), we have two sources and two sinks.

Using a grid resolution of 64^2 , with $N_0 = 2$, we have computed P_{fix} as a function of s as reported in fig. 3.8. Two different behaviors can be observed depending on the value of s . The small s region is very well fitted by the Kimura formula (3.22) with an effective population size given by eq. (3.26) and with the same value of $B_1 = 3.5$ used in [11].

From fig. 3.8, it is clear that the behavior of P_{fix} , for large enough s , is controlled by a different value of the effective population size, hereafter referred to as N_g . In one dimension, following [11], the effective population size is estimated by considering the scale δ near to a source in x_s where $u_0\delta \sim B_2 2\sqrt{D\mu s}$, with B_2 another constant of the order of 1: an initial population in $x \in [x_s - \delta, x_s + \delta]$ can develop a Fisher genetic wave at speed $2\sqrt{D\mu s}$, which is supported by the velocity field. Only Fisher genetic waves that start in this interval are able to cross the system; this provides an estimate $N_g = 2\delta(s)\rho_0$. In two dimensions, the same argument gives:

$$N_g \sim 4\delta^2\rho_0 = 4 \left[\frac{2\sqrt{D\mu s}}{u_0} \right]^2 \rho_0. \quad (3.27)$$

Using eq. (3.27), we obtain the curve (black) of fig. 3.8, which provides an excellent fit of the numerical simulations.

Finally, since both N_{eff} of eq. (3.26) and N_g given by eq. (3.27) are proportional to $N = 64^2 N_0$ for our simulations, we can easily predict that upon increasing N_0 , the fixation probability will follow the same master curve if plotted as a function of sN . To demonstrate this and to validate the quality of our method for large N_0 , we show, in fig.

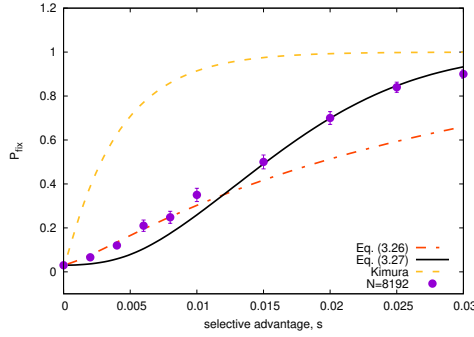


Figure 3.8: Probability of fixation under a 2D velocity field as a function of the selective advantage. The yellow dashed line represents the Kimura theoretical line in the absence of flow that follows eq. (3.22). The base grid is 64×64 with two individuals per cell, so the total number of individuals is $N = 8192$. In addition, the diffusivity parameter is 10^{-2} and the velocity value is $u_0 = 0.05$. The black continuous line and the red dot-dashed line are the theoretical predictions and our simulations are illustrated by symbols, with an error bar of about 5%, both in good agreement.

3.9, P_{fix} as obtained for the same flow as eq. (3.25) for $N_0 = 2$ and $N_0 = 10$. The red dot-dashed and black continuous curves obtained using the prescriptions discussed above for small s and large s , respectively, provide an excellent fit for the numerical results. Overall, the results discussed in this section extend the ones previously obtained in [11] and demonstrate the validity of our method for population dynamics advected by an external compressible velocity field.

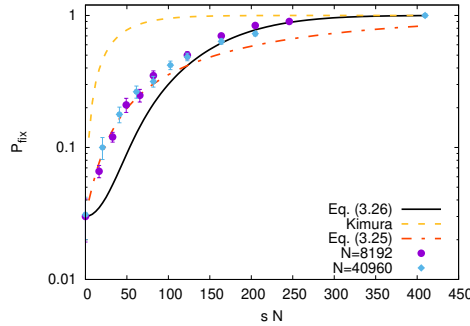


Figure 3.9: Kimura probability of fixation in the presence of the velocity field. Calculations were carried out with an overall mesh size of 64×64 and with 10 individuals per cell. The total number of individuals is $N = 40960$. The yellow dashed line shows the theoretical Kimura's trend, while the red dot-dashed and the black continuous lines represent the numerical prediction. Dots and diamonds represent our simulations for two different N , 8192 and 40960, respectively, with an error bar of about 5%.

3.5 Conclusions

In the present chapter, we developed a numerical method suitable for accurately and efficiently investigating the behavior of population dynamics and genetics under flow. This approach allows for the study of a large number of individuals by, first, implementing the diffusion and advection processes, particle by particle, and afterward, for each box composing the 2D lattice, performing the birth and competition steps.

In order to test and validate our method, we considered a one-dimensional system. We implemented the FKPP equation, analyzing the algorithm convergence.

After that, we applied this method to the heterozygosity and Kimura formula and we found a very good agreement between the theoretical and simulated results. The method we propose does not require any dynamic management of particle positions and has no limitations on the number of individuals for mesh points. Both features imply major simplifications in computer coding, especially for a large number of individuals and for parallel computation. It is worth remarking that for a large number of individuals, one can increase the computational efficiency of our method by directly sampling the binomial distribution in each mesh point along the lines discussed in [72].

For the 2D system, we retraced the procedural scheme of the one-dimensional system and we investigated the larger system under an advection field composed of two sinks and two sources. Our main result was to find, for the 2D system, a net growth of particles born in the proximity of a source, as compared to the individuals at different initial positions.

An interesting aspect, to follow up on our work, is presented in chapter 5. It is related to the effect of stochastic fluctuations in antagonist population dynamics and the exploration of the effect of external velocity on the genetic nucleation theory.

4 | Strong noise limit for population dynamics in incompressible advection

Genetic diversity relates to all the changes at the basis of the evolution process of populations. In marine environments, several factors like the amount of nutrients, temperature, etc..., play an important role in determining the dynamics of a population. An important and yet rather unexplored study is the understanding of the role of the dispersion of the individuals.

In chapter 1 we have seen how propagating fronts play a key role in population dynamics. The reaction-diffusion systems can be described by two types of fronts: pulled and pushed. In particular, pulled waves are powered by high growth rates at the leading edge, where the number of organisms is low and fluctuations are large. Some biological evolution models are very sensitive to noise as long as they are characterized by few individuals and small values of diffusivity.

In this regard, we are interested in understanding if the probability fixation, theorized by Kimura in the well-mixed case [22], holds also in the strong noise regime.

In the well-mixed environment, the fixation probability and the time spent by the beneficial organisms to get over all the population can be written as

$$P_{fix} = \frac{1 - e^{-sNf_0}}{1 - e^{-sN}} \quad (4.1)$$

$$T_{fix} = \frac{Nf_0}{\mu(1 - f_0)} \log\left(\frac{1}{f_0}\right) \quad (4.2)$$

where f_0 is the initial relative fraction of a population with a small selective advantage s , N is the total population size and $1/\mu$ is the generation time.

In this chapter, we give a theoretical framework to support previous findings according to which the fixation probability is independent of the diffusivity acting in the system. We further investigate the effect of an incompressible two-dimensional flow on the dynamics of an advantageous allele. In particular, we will study how P_{fix} and T_{fix} may change (see 1.6.4 subsection) in presence of an advecting flow.

Finally, we summarize our results and discuss their relevance in the case of population dynamics of oceanic phytoplankton subjected to marine turbulence. All the numerical simulations are based on the method discussed in [70] (see chapter 3).

4.1 Theory

We consider two populations, A and B , in a two-dimensional closed system of size $L \times L$ endowed with periodic boundary conditions. Let c_A and c_B , denote the relative time/space-dependent concentrations, with $c_A + c_B = 1$. The two populations are advected by an incompressible velocity field. The dynamics of a population is well described by the continuum stochastic Fisher equation in terms of diffusion D , logistic growth μ , selective advantage s , and advection \vec{v} . Upon denoting f as the fraction of the concentration of a species over the total concentration, $f \equiv c_A/(c_A + c_B)$, the discretized form of the equation governing the dynamics of the two populations is:

$$\frac{\partial f}{\partial t} + \vec{v} \cdot \vec{\nabla} f = D\Delta f + \mu s f(1 - f) + \left[\frac{2\mu}{N_0} f(1 - f) \right]^{1/2} w(\vec{x}, t) \quad (4.3)$$

where N_0 is the total number of organisms per deme and $w(\vec{x}, t)$ is a Gaussian random process δ -correlated both in space and time. Given the deme size a , eq. (4.3) can be discretized on a regular grid of n points, where $n = L/a$, with L being the domain size (see chapter 3 for an extensive explanation). For a two-dimensional case, $N = n \times n$ demes exist in the domain. In the following, we will use the notation f_i , with $i = 1, 2, \dots, N$, to indicate the value of $f(x, y, t)$ in the deme i and consequently $\vec{\nabla} f_i$, Δf_i denoting values of $\vec{\nabla} f$ and Δf in the same deme. The divergence of the velocity field is assumed to be zero. Upon averaging eq. (4.3) in space and by denoting $f(m)$ as the space average of $f(x, y, t)$, we obtain:

$$\frac{\partial f(m)}{\partial t} = \mu s \langle H \rangle + \left[\frac{2\mu}{N_T} \langle H \rangle \right]^{1/2} w(t) \quad (4.4)$$

where $N_T = N_0 N$, $H \equiv f(x, y, t)(1 - f(x, y, t))$ is the heterozygosity, which is the measure of genetic variation at a locus, $w(t)$ is a Gaussian random process δ -correlated in time, and $\langle \dots \rangle \equiv \frac{1}{L^2} \int \dots dx dy$. In order to obtain the noise variance on the r.h.s. of eq. (4.4), we define the noise term acting on $f(m)$ as

$$\frac{1}{N} \sum_i \left[\frac{2\mu}{N_0} f_i(1 - f_i) \right]^{1/2} w_i \equiv \frac{1}{N} \sum_i \sigma_i w_i \quad (4.5)$$

where σ_i is equivalent to $\left[\frac{2\mu}{N_0} f_i(1 - f_i) \right]^{1/2}$ and w_i is a shorthand notation for the noise

acting on deme i . Since $\langle w_i w_j \rangle = \delta_{ij}$, the variance of the noise term (4.5) is given by

$$\left\langle \frac{1}{N^2} \sum_{i,j} \sigma_i \sigma_j w_i w_j \right\rangle = \frac{2\mu}{N_0 N^2} \sum_i f_i (1 - f_i) = \frac{2\mu}{N_0 N^2} \langle H \rangle. \quad (4.6)$$

The space averaged $\langle H \rangle$ can also be written as

$$\langle H \rangle = H(f(m)) - \langle (\delta f)^2 \rangle \quad (4.7)$$

where $H(f(m)) = f(m)(1 - f(m))$ and $\delta f \equiv f(x, y, t) - f(m)$. Following the results discussed in [17, 73] and considering small values of the selective advantage, s , we can obtain useful insights on the dynamics of the system by looking at the equation for H at $s = 0$, namely

$$\frac{\partial H}{\partial t} + \vec{v} \cdot \vec{\nabla} H = D \Delta f - 2Df \Delta f - \frac{2\mu}{N_0} f(1 - f) + \dots \quad (4.8)$$

where the third term on the r.h.s of eq. (4.8) is derived from the application of Itô's calculus and the final dots represent all the terms due to noise.

Next, we perform a space averaging. Due to the periodic boundary conditions and to the incompressibility of the velocity field, we can use the identities $\langle \Delta f \rangle = 0$, $\langle \vec{v} \nabla H \rangle = \langle \text{div}(\vec{v} H) \rangle = 0$ and $-\langle f \Delta f \rangle = \langle (\nabla f)^2 \rangle$. The final result is achieved by: 1) averaging eq. (4.8) over the noise realizations, which allowed us to neglect the noise; 2) neglecting the time derivative $\partial_t \langle H \rangle$, which rapidly goes to zero both in one and in two dimensions (see [7] for details). Then, we get:

$$D \langle (\nabla f)^2 \rangle = \frac{\mu}{N_0} \langle H \rangle \quad (4.9)$$

Let us also remark that eq. (4.9) is formally independent of \vec{v} . Possible effects due to the velocity advection can be explored through the following steps. The time variable t_* , is introduced and defined by the relation

$$D \langle (\nabla f)^2 \rangle \equiv \frac{1}{t_*} \langle (\delta f)^2 \rangle. \quad (4.10)$$

Using eq. (4.10) into eq. (4.7) we can compute $\langle H \rangle$ as a function of $H(f(m))$ and we

obtain

$$\langle H \rangle = H(f(m)) - \frac{\mu t_*}{N_0} \langle H \rangle. \quad (4.11)$$

Solving eq. (4.11) for $\langle H \rangle$, it turns out

$$\langle H \rangle = AH(f(m)) \quad (4.12)$$

where

$$A = \frac{1}{1 + \frac{\mu t_*}{N_0}} \quad (4.13)$$

Using eq. (4.12) we can express $\langle H \rangle$ as $H(f(m)) = f(m)(1 - f(m))$. We insert this latter in eq. (4.4) obtaining:

$$\frac{\partial f(m)}{\partial t} = sA\mu f(m)(1 - f(m)) + \left[\frac{2\mu A}{N_T} H(f(m)) \right]^{1/2} \quad (4.14)$$

The key quantity to consider from now on is the ratio $G \equiv \mu t_* / N_0$. For $G \ll 1$ and eq. (4.13), we obtain $A \sim 1$ and eq. (4.14) reduces to the case of a well-mixed population with selective advantage s . On the contrary, for $G \gg 1$ we get $A\mu \sim N_0/t_*$ and the characteristic time of the system dynamics depends explicitly on both N_0 and t_* . This is the case referred to as strong noise limit where the genetic drift, directly related to population size (small = more drift, large = less drift), becomes important.

Firstly, we analyzed the case $\vec{v} = 0$, i.e. the case where $t_* = t_D$. The effect of random perturbations, caused by the growth and death processes of a population, within each single deme implies that the concentration gradients must be of order $1/a$.

A reasonable guess on t_D may be derived by considering, the two-dimensional stochastic differential equation

$$\partial_t \phi = D\Delta\phi + \sqrt{\epsilon w}(\vec{x}, t). \quad (4.15)$$

Assuming that there exists an "ultraviolet" cutoff k_M , it is possible to exactly compute the ratio $\langle (\nabla\phi)^2 \rangle / \langle (\phi)^2 \rangle$ obtaining:

$$\frac{\langle (\nabla\phi)^2 \rangle}{\langle (\phi)^2 \rangle} \sim k_M^2. \quad (4.16)$$

(Mathematical details for the k_M introduction will be treated in the [Appendix](#)). From the

above insight, using $k_M \sim 1/a$, we have

$$t_*(\vec{v} = 0) \equiv t_D \sim \frac{a^2}{D}. \quad (4.17)$$

By means of equations (4.13), (4.14), and (4.17) the following result is obtained:

$$\begin{aligned} \frac{\partial f(m)}{\partial t} &= \frac{\mu}{1 + \frac{\mu}{N_R D}} s f(m)(1 - f(m)) + \\ &+ \left[\frac{2}{N_T} \frac{\mu}{1 + \frac{\mu}{N_R D}} f(m)(1 - f(m)) \right]^{1/2} \end{aligned} \quad (4.18)$$

where $N_R = N_0/a^2 \equiv N_T/L^2$ is the population density.

The strong noise limit for eq. (4.18) is expressed by the condition $\mu a^2/(N_0 D) = \mu/(N_R D) \gg 1$ which corresponds to $\frac{a^2}{N_0 D} \gg \frac{1}{\mu}$. In the strong noise limit, eq.(4.18) becomes:

$$\begin{aligned} \frac{\partial f(m)}{\partial t} &= N_R D s f(m)(1 - f(m)) + \\ &+ \left[\frac{2 N_R D}{N_T} f(m)(1 - f(m)) \right]^{1/2} \end{aligned} \quad (4.19)$$

From eq.s (4.18), (4.19) the fixation probability P_{fix} for a well-mixed population is deduced as the one derived from Kimura theory [22]. Through eq. (4.1) is possible to derive P_{fix} in the space-dependent dynamics. A simple computation shows that P_{fix} is independent of the diffusivity, D . This is a rather remarkable result first predicted by Doering et. al. [17], for the one-dimensional problem in the strong noise limit, and observed by [4, 25] in both one and two dimensions. Here we get a clear-cut explanation for this result.

Thanks to eq.s (4.18), (4.19) we derive that for both cases, strong and weak noise, the probability of fixation P_{fix} can be computed by knowing N_T and the space average of the initial population fraction, hereafter denoted by $f(m, 0)$. Using (4.1) we get:

$$P_{fix} = \frac{1 - e^{-s N_T f(m, 0)}}{1 - e^{-s N_T}} \quad (4.20)$$

Next we can rewrite $N_T f(m, 0) = N_R \int dx dy f(x, y, 0)$. Performing the limit $L \rightarrow \infty$,

$N_T \rightarrow \infty$ with $N_R = \text{const}$, we obtain

$$P_{fix} = 1 - e^{-sN_R \int dx dy f(x,y,0)} \quad (4.21)$$

which is the generalization, in two dimensions, of the result proved in [17] for the one-dimensional case only.

In the strong noise limit, taking as a reference eq. (4.19), space average population $f(m)$ behaves as a well-mixed population of size N_T growing (or decaying) with a characteristic timescale $1/(N_R D)$ and a selective advantage s . Then, the average fixation time should be on the order $N_T/(N_R D) \sim L^2/D$ which is the expected timescale for fixation at $\vec{v} = 0$, in the continuous limit of eq. (4.3). On the contrary, the average fixation timescale is on the order of N_T and it is independent of the diffusivity D , in the weak noise limit. In summary, for $\vec{v} = 0$ our theoretical approach agrees with both theoretical and numerical findings in both one and two dimensions and supports our estimate given in eq. (4.17), i.e. $t_* = a^2/D$.

We now turn our attention to the case $\vec{v} \neq 0$. In this case, the estimate of t_* , referred to as t_u in the following, computed in terms of the ‘‘effective’’ or ‘‘eddy’’ diffusivity D_{eff} and the corresponding space scale l_u :

$$t_*(\vec{v} \neq 0) \equiv t_u \sim \frac{l_u^2}{D_{eff}} \quad (4.22)$$

In general, it is possible to show that $t_u < t_D$. This inequality can be understood through the following reasoning. Let us define \tilde{D}_{eff} as the effective diffusivity acting at the deme scale a over the time t_u , i.e. $\tilde{D}_{eff} t_u = a^2$. It follows that $\tilde{D}_{eff} = D_{eff} a^2 / l_u^2$ and we expect the advection to be relevant in the dynamics provided $\tilde{D}_{eff} \geq D$. Then:

$$\tilde{D}_{eff} = D_{eff} \frac{a^2}{l_u^2} \geq D \rightarrow t_D \equiv \frac{a^2}{D} \geq \frac{l_u^2}{D_{eff}} \equiv t_u \quad (4.23)$$

The inequality $t_u < t_D$ implies that the strong noise limit for $\vec{v} \neq 0$ may be observed only if, for $\vec{v} = 0$, the system is in the strong noise regime.

In presence of an advection velocity field, eq. (4.14) becomes:

$$\begin{aligned} \frac{\partial f(m)}{\partial t} &= \frac{\mu}{1 + \frac{\mu l_u^2}{N_0 D_{eff}}} s f(m)(1 - f(m)) + \\ &+ \left[\frac{2}{N_T} \frac{\mu}{1 + \frac{\mu l_u^2}{N_0 D_{eff}}} f(m)(1 - f(m)) \right]^{1/2} \end{aligned} \quad (4.24)$$

As already noted, to understand whether or not the strong noise limit is achieved, the relevant quantity we need to analyze is:

$$G_u \equiv \frac{\mu l_u^2}{N_0 D_{eff}} \quad (4.25)$$

For $G_u \gg 1$, the system should be considered in the strong noise limit and eq. (4.24) becomes

$$\begin{aligned} \frac{\partial f(m)}{\partial t} &= \frac{N_0 D_{eff}}{l_u^2} s f(m)(1 - f(m)) + \\ &+ \left[\frac{2}{N_T} \frac{N_0 D_{eff}}{l_u^2} f(m)(1 - f(m)) \right]^{1/2} \end{aligned} \quad (4.26)$$

There is no simple analytical way to estimate D_{eff} and l_u for a prescribed velocity field \vec{v} . In some cases, as the one considered in this section, an explicit computation of D_{eff} and l_u can be done (see [39] and [15] for further details). In general, a characteristic velocity field u_0 such that $D_{eff} = u_0 l_u$ can be introduced. This is, for instance, the case for a turbulent flow where u_0 is the characteristic scale of the turbulent kinetic fluctuations, on scale l_u , and D_{eff} is obtained by the Richardson diffusion [14]. Using $D_{eff} = u_0 l_u$ the condition $G_u \gg 1$ becomes $\mu l_u / (N_0 u_0) \gg 1$ which is the same condition given by $Da \equiv \frac{\mu l_u}{U} \gg N$.

Finally, using eq. (4.26) and the inequality $t_u < t_D$, for the average fixation time, we get

$$\frac{N_T l_u^2}{N_0 D_{eff}} = \frac{N_T}{N_0} t_u \leq \frac{N_T}{N_0} t_D = \frac{L^2}{D} \quad (4.27)$$

For large G_u , the effect of the velocity advection is to speed up the characteristic time need to reach fixation. This is also another way to understand the inequality $t_u < t_D$.

In the next two sections, we provide numerical evidence to support our theoretical discussions.

4.2 Numerical approach

For our numerical investigations, we consider a two-dimensional domain of size $L = 2\pi$ with a deme size $a = L/128$. The numerical method used in the following study is based on [70] and revised in chapter 3. The velocity field \vec{v} is given by:

$$v_x = u_0 \sin(k(y - L/2) + \phi(t)) \quad (4.28)$$

$$+ \phi(t) \cos(k(x - L/2) + \phi(t))$$

$$v_y = -u_0 \sin(k(x - L/2) + \phi(t)) \quad (4.29)$$

$$+ \phi(t) \cos(k(y - L/2) + \phi(t))$$

$$\phi(t) = \delta \sin(\omega t) \quad (4.30)$$

Using the above choice of \vec{v} we can consider three different cases:

- *No-flow*: $u_0 = 0$
- *Non-chaotic flow*: $u_0 > 0$ and $\delta = 0$
- *Chaotic flow*: $u_0 > 0$ and $\delta = \delta_0$

The *No-flow* case refers to the “standard” FKPP equations already investigated in many papers (see for instance [7], [10]). The second case corresponds to a *non-chaotic* cellular flow [74]. While the last one corresponds, for a proper choice of δ_0 , to a *chaotic* cellular flow. $k = 8$ is set for all cases, and for the *chaotic flow* case we choose $\delta_0 = 2$ and $\omega = 2$ ensuring the occurrence of a chaotic flow condition. Finally, in all our numerical investigations, we consider $f(x, y, 0) = 0.0625$ uniformly distributed in the domain. We study the dynamics of the system as a function of N_0 , u_0 , and D .

For cellular flow, we can employ the analytical approach developed in [39] and [15] to compute D_{eff} as a function of $l_u \equiv 2\pi/k$ and u_0 . We find that for the *non-chaotic flow*, $D_{eff} \sim \sqrt{D u_0 l_u}$, whereas for the *chaotic flow*, $D_{eff} \sim u_0 l_u$.

Based on the theoretical analysis done in the previous section, we are interested in computing the quantity A defined in eq. (4.12) and, in particular, we are interested in studying the quantity $G \equiv A^{-1} - 1$ for the three different cases. Next, using eq. (4.17), for $\vec{v} = 0$ and eq. (4.22) for $\vec{v} \neq 0$ we obtain:

- $G_{No-flow} \sim \frac{\mu a^2}{N_0 D}$
- $G_{Non-chaotic flow} \sim \frac{\mu l_u^2}{N_0 \sqrt{D l_u u_0}}$

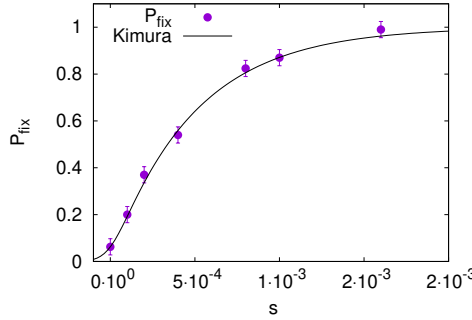


Figure 4.1: Kimura Fixation probability as a function of the selective advantage, s obtained from a chaotic flow. Simulations (purple circles) are performed with $N_0 = 2$, diffusion coefficient of $D = 10^{-3}$ and $u_0 = 1$. The continuous black line corresponds to the Kimura formula eq. (4.1). The error bar is calculated as $\sqrt{P_{fix}(1 - P_{fix})/m}$, where m is the number of simulations. For the results shown in the figure $m = 500$.

- $G_{Chaotic\ flow} \sim \frac{\mu l_u^2}{N_0 u_0 l_u}$

4

By relying on the above expressions of G for the cases of *no-flow*, *non-chaotic flow* and *chaotic flow*, we predict three different scaling properties to be observed, namely:

- I) different scaling laws as a function of D : $G_{No-flow} \sim D^{-1}$, $G_{Non-chaotic\ flow} \sim D^{-1/2}$ and $G_{Chaotic\ flow}$ independent on D
- II) same scaling properties for all cases as a function of N_0 , i.e. N_0^{-1}
- III) diversity in the scaling behavior of $G_{Non-chaotic\ flow}$ and $G_{Chaotic\ flow}$ as a function of u_0 : $G_{Non-chaotic\ flow} \sim u_0^{-1/2}$ and $G_{Chaotic\ flow} \sim u_0^{-1}$.

Besides the scaling predictions listed above, our theoretical analysis shows that the fixation probability P_{fix} , eq. (4.3), depends neither on D nor on u_0 . The fixation probability is given by Kimura's formula or equally by the Doering's relation in the limit $L \rightarrow \infty$, as already shown for $u_0 = 0$ in [10].

In figure 4.1 we support our conclusion by showing P_{fix} with $u_0 = 1$ and for the *chaotic flow* case with $D = 10^{-3}$ and $N_0 = 2$. The black line in the figure represents the trend of Kimura's formula which agrees extremely well with the numerical results, sketched by the purple solid circles.

Next, we discuss how A can be numerically calculated. Eq. (4.12) has been derived assuming an average of different realizations. Let us define $\langle H \rangle_\alpha$ the value of $\langle H \rangle$ for the α realization and $f(m)_\alpha$ the corresponding value of $f(m)$ for the same realization.

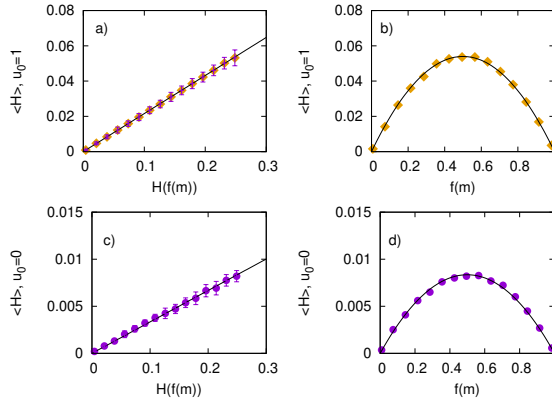


Figure 4.2: In the panels on the left, two graphs representing the average heterozygosity versus the heterozygosity of the mean value of f are shown. On the right, the plots of the average heterozygosity as a function of the average value of f are sketched. The panels on the top differ from the ones on the bottom because of the presence of the chaotic flow (diamonds). The lower panels are the cases with no flow (circles purple points). We performed simulations for $D = 10^{-3}$ and $N_0 = 2$. The error bars are 3 times the variance computed over 100 realizations.

Both $\langle H \rangle_\alpha$ and $f(m)_\alpha$ are functions of time. Then eq. (4.12) states that

$$\langle \bar{H} \rangle = AH(\bar{f}(m)) \quad (4.31)$$

where the $\bar{\cdot}$ is the average over different realizations, i.e. $M^{-1} \sum_\alpha \dots$, with M the number of realizations. In figure 4.2 we show the quality of the results we obtain for the cases *no-flow* and *chaotic flow* with $D = 10^{-3}$, $N_0 = 2$, imposing for the last one $u_0 = 1$. The left panels show the plot of $\langle \bar{H} \rangle$ for $u_0 = 1$ (top) and $u_0 = 0$ (bottom) as function of the heterozygosity of the mean value of f whereas the right panels show the behavior of $\langle \bar{H} \rangle$ as function of $\bar{f}(m)$ for $u_0 = 1$ (top) and $u_0 = 0$ (bottom). We also computed the quantity A_α for each realization, i.e. we calculate A_α as the best fit of the relation $\langle H \rangle_\alpha = A_\alpha H(f(m)_\alpha)$. The error bars in figure 4.2 refer to the three-time variance of A_α . The same result holds for different values of s and D . From the numerical simulations we can obtain a measure of A with an accuracy of about 1%.

Next, we consider how the computation of A may eventually depend on s . In figure 4.3 we show $\langle \bar{H} \rangle$ as a function of $H(\bar{f}_m)$ for the *chaotic flow* case with $D = 10^{-3}$ and three different values of $s = 10^{-4}$, $s = 10^{-3}$, and $s = 1.6 \cdot 10^{-3}$. No difference is observed in A between the three different cases. Based on the results of figure 4.3, we can reasonably reach the conclusion that our numerical computation of A is independent of s . From the knowledge of A , we can extract the value of $G = A^{-1} - 1$ for three different cases *no-flow*, *non-chaotic flow*, and *chaotic flow*.

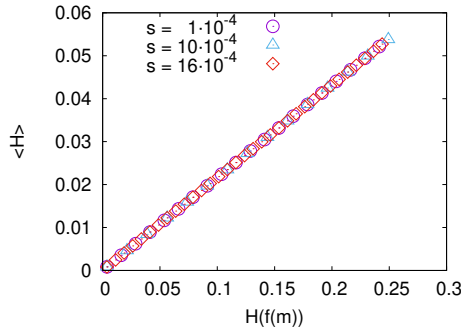


Figure 4.3: Average heterozygosity vs heterozygosity of the average value of f for three different values of the selective advantage, s , under a chaotic flow. Parameters $N_0 = 2$ and $D = 10^{-3}$.

4.3 Comparison with analytical estimate

4

As stated in the previous section, we have three different predictions on the scaling $G = A^{-1} - 1$ for the three considered cases with *no-flow*, *non-chaotic flow* and *chaotic flow*. Prediction I) refers to the behavior of G with respect to the diffusivity D , and we expect

$$\begin{aligned}
 G_{No-flow} &\sim \frac{1}{D} \\
 G_{Non-chaotic flow} &\sim \frac{1}{\sqrt{D}} \\
 G_{Chaotic flow} &\sim const.
 \end{aligned}
 \tag{4.32}$$

As discussed in section 4.1, the scaling of $G_{Non-chaotic flow}$ and $G_{Chaotic flow}$ depends on how the effective or Eddy diffusivity D_{eff} depends on D . For both the cases with *chaotic* and *non-chaotic flow*, the effective diffusivity can be computed [15]. We obtain for the *non-chaotic* case $D_{eff} \sim \sqrt{D}$, whereas for the *chaotic* case D_{eff} is independent of D . To check the scaling eq. (4.32) we consider $D \in [0.0002, 0.016]$ for all cases and we fix $N_0 = 2$. The results are shown in figure 4.4 where we plot $G_{No-flow}$, $G_{Non-chaotic flow}$ and $G_{Chaotic flow}$ as a function of D . The two straight lines refer to the scaling D^{-1} and $D^{-1/2}$. For the *non-chaotic flow* case, the computation performed at $u_0 = 1$ is shown whereas for the *chaotic flow* case, it is shown for two different values of u_0 , namely $u_0 = 1$ and $u_0 = 0.2$. For a relatively small value of D the three different scaling behaviors (4.32) are satisfied. For a relatively large value of D , the values of G decrease and approach order 1, this result is expected since the so-called "weak noise" regime is defined for large enough values of D , and the spatial effects can be neglected. Besides that, we can observe that

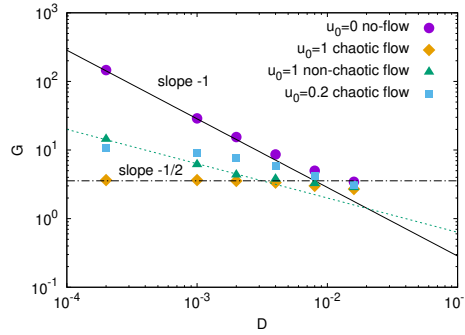


Figure 4.4: Values of G as a function of the diffusion parameter D . Circles, triangles, squares, and diamonds represent our simulations for different velocity cases: no velocity ($u_0 = 0$), non-chaotic velocity field for the value $u_0 = 1$, and chaotic velocity field for the values $u_0 = 0.2$ and $u_0 = 1$, respectively. The continuous and dashed lines refer to the linear fit of the simulation results whose slope are -1 in one case and $-1/2$ in the other case. The horizontal dot-dashed line shows the constant value achieved for the chaotic flow with $u_0 = 1$ at very small D . The error bar is estimated from the error of the best fit; it is smaller than the size of the system, which is why it cannot be seen from the graph.

the $G_{Non\text{-}chaotic\ flow}$ and the $G_{Chaotic\ flow}$ are both smaller than the $G_{No\text{-}flow}$, independently of D . This observation agrees with our theoretical discussion reported in section 4.1 and implies the relation $t_u < t_D$.

Next, we consider the behavior of G as a function of $N_T = N_0 n^2$. For all cases we should observe that $G \sim N_T^{-1}$. To check this prediction, we consider the two cases *no-flow* and *chaotic flow* and in figure 4.5 we show $G_{No\text{-}flow}$ and $G_{Chaotic\ flow}$ as a function of N_T (note that $G_{No\text{-}flow}$ has been multiplied by 10 to make the figure more readable). Again, the behavior of G as a function of N_T is rather well satisfied. Combining the results shown in figures 4.4 and 4.5 we can argue, as already noted in section 4.1, that the continuous limit of eq. (4.3) can be achieved by sending $N_T \rightarrow \infty$ and by keeping $N_T D$ small and constant. In other words, the continuous limit of eq. (4.3) is achieved by increasing the domain size at constant density and by vanishing the diffusivity.

The last prediction discussed in section 4.2, applies only to cases *no-flow* and *chaotic flow* and refers to the scaling behavior of G with respect to the velocity u_0 :

$$G_{Non\text{-}chaotic\ flow} \sim \frac{1}{u_0^{1/2}}; \quad G_{Chaotic\ flow} \sim \frac{1}{u_0} \quad (4.33)$$

In figure 4.6, we show $G_{Non\text{-}chaotic\ flow}$ and $G_{Chaotic\ flow}$ for $N_0 = 2$, $D = 10^{-3}$ and $u_0 \in [0.1, 1]$. Note that $G_{Chaotic\ flow}$ has been increased by a factor 10 to make the figure more readable. The scaling (4.33) is well verified in both cases.

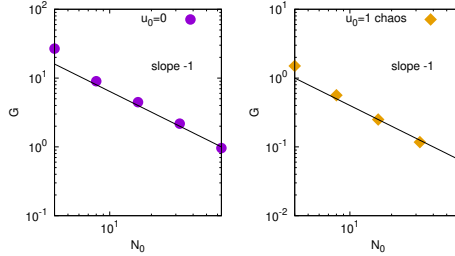


Figure 4.5: Values of G as a function of the number of individuals N_0 per deme. The left panel (purple circles) represents the case of no-velocity while the right panel (yellow diamonds) represents the results in presence of a chaotic flow with $u_0 = 1$. Both curves follow the slope -1 . In both cases we used $D = 10^{-3}$ and $N_0 \in [4 : 64]$.

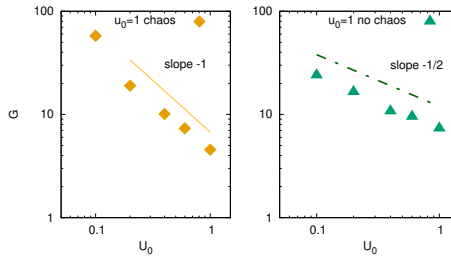


Figure 4.6: Values of G as a function of the velocity intensity u_0 . Diamonds (left panel) point out the results under chaotic velocity field while triangles (right panel) indicate the findings in the presence of a non-chaotic velocity field. The two different behaviors are shown: the chaotic results follow the slope -1 (left panel) whereas the non-chaotic ones follow the slope $-1/2$ (right panel). The numerical parameters used in the simulations are $N_0 = 2$ and $D = 10^{-3}$.

The results shown in figures 4.4, 4.5 and 4.6 validate the theoretical analysis performed in section 4.1. Without any advection field, the timescale of the dynamics is controlled by the ratio $G_D = \mu/(N_R D)$, where $N_R = N_T/L^2$ is the population density and the diffusivity plays a relevant role only for $G_D \gg 1$. In presence of advection, the relevant parameter depends on the effective diffusivity D_{eff} and its corresponding length scale l_u through the combination $G_u = \mu l_u^2/(N_0 D_{eff}) \leq G_D$. In general, the functional form of D_{eff} depends on the flow properties (as shown in figures 4.4 and 4.6). For a large value of G_u , the timescale of the dynamics is controlled by the effective diffusivity and by l_u . In all cases, the fixation probability depends neither on the diffusivity nor on the advection, assumed to be incompressible.

4.4 Conclusions

In this chapter, we focus our investigation on the fixation probability between two populations, one of which has a slight selective advantage. In particular, we consider the case of two populations whose dynamics is confined in a closed system and, eventually, advected by a two-dimensional incompressible flow. We also restrict our consideration to the case of two populations that are initially uniformly distributed in the space, and the one with the selective advantage presents a space density $f(0) \ll 1$. For the well-mixed case, when both diffusion and/or advection are irrelevant, the fixation probability is given by the Kimura theory. For the one-dimensional system and without advection, it was shown that the fixation probability does not depend on the value of diffusivity acting in the system [38]. This result has been confirmed by Maruyama (1974) [25] and thanks to the numerical simulations performed by Pigolotti et al., [10] who also argued that Doering's findings should be true also for the two-dimensional case, still without advection.

Previous evidence was generalized in several ways. We provided a theoretical analysis showing that the fixation probability should be independent of the diffusivity and the effect of the velocity field, if present. We have also shown that, without advection, the results in [38] are recovered for small diffusivity or equivalently for large system size. Concerning this latter case, we have argued theoretically and checked numerically that the dimensionless relevant parameter in the system is the ratio $\mu/(N_R D)$, where $1/\mu$ is the generation time for the population growth, N_R is the population density and D the diffusivity. In the strong noise regime, corresponding to $\mu/(N_R D) \gg 1$, the timescale for the fixation occurrence depends on N_R , D and s . Therefore, we expect fixation to occur on a timescale L^2/D . Our analysis has been generalized to take into account the effect of advection. The relevant dimensionless parameter is $\mu l_u^2/(N_0 D_{eff})$, where N_0 is the number of individuals per deme, D_{eff} is the effective or eddy diffusivity induced by the flow and l_u is the corresponding length scale of the flow. The equivalent of the strong

noise regime is given by the condition $\mu l_u^2 / (N_0 D_{eff}) \gg 1$. In this regime, the fixation timescale is controlled by the flow dynamics. We remark that the quantity $\mu l_u^2 / (N_0 D_{eff})$ plays the same role of the Damköler number $Da = \mu l_u / u_0$ for the continuous equation (with no number fluctuations i.e. with no variation in the number of particles within the deme) where u_0 is the characteristic velocity of the flow field. It is known that, without number fluctuations, the front speed of a population advected by an incompressible velocity field depends on the Damköler and the *Péclet* number $u_0 l_u / D$ [15]. When the number of fluctuations are taken into account, previous theoretical and numerical findings for the continuous case are valid, provided that the relation $\mu l_u^2 / (N_0 D_{eff}) \gg 1$ is met.

Besides the above results, which nicely generalize many previous findings, one can wonder whether the effect of the advection of an incompressible flow may be relevant for some realistic cases. In particular, we want to consider the case of phytoplankton dynamics subject to ocean circulation and turbulence. We assume that, without advection, the phytoplankton dynamics can be considered to be in the strong noise regime, where diffusivity effects control the time scale in which the slightly advantageous population eventually dominates (fixation). This is true, for instance, for population density on the order of $10^7 - 10^9$ individuals for m^3 with a generation time on the order of 1 day and size of order $1 \mu m$ corresponding to diffusivity order $10^{-13} m^2 / sec$. Depending on the population density, these parameters correspond to $\mu / (N_R D) \in [50 : 1000]$. Next, we consider the effect of turbulence knowing that the effective diffusivity becomes scale-dependent and it can be estimated using the Richardson theory and the Kolmogorov scaling. Let ϵ be the energy dissipation per unit mass of the turbulent flow, l the scale in which the effect of the effective viscosity $D_{eff} \sim \epsilon^{1/3} l^{4/3}$ and $N_0 \sim 1$ is considered and the relevant dimensionless quantity which becomes $G_t \equiv \mu l^2 / (N_0 D_{eff})$. An estimate of ϵ can be obtained by using the recent analysis performed by [75], where it is shown that, for $l \sim 10 km$, the probability distribution of ϵ is similar to a log-normal distribution with a most probable value near the surface close to $\epsilon \sim 10^{-10} m^2 / sec$. Through these approximations, we obtain $G_u \sim 10$ and the timescale of the fixation occurrence becomes on the order of 10 days. This estimate is clearly very rough since all the considered variables show strong and even intermittent fluctuations both in space and in time. At any rate, the evaluation of G_u illustrates that the advection of a relatively weak compressible flow, for instance, due to a moderate upwelling, may become an important effect on the population dynamics located in the upwelling region, as discussed in [11]. This effect varies depending on the population sizes, densities, characteristics of the population (motile versus non-motile), and also on different flow characteristics, thus contributing, directly or indirectly, to the well-known complex dynamics of oceanic biomass.

Appendix: Mathematical details for introducing the cutoff k_M

In this appendix, an explanation regarding the introduction of the cutoff k_M in the system, during the step between equation (4.15) and (4.16), is given.

By combining the equation (4.16), namely

$$\frac{\langle(\nabla\phi)^2\rangle}{\langle\phi^2\rangle} \sim k_M^2 \quad (4.34)$$

with the equation (4.10),

$$D \frac{\langle(\nabla f)^2\rangle}{\langle(\delta f)^2\rangle} = \frac{1}{t_*} \quad (4.35)$$

we get the follow relation:

$$\frac{1}{t_*} = Dk_M^2 = \frac{D}{a^2}. \quad (4.36)$$

Thus, it is possible to derive the timescale t_* , as

$$t_* = \frac{a^2}{D}. \quad (4.37)$$

Now, to solve the following equation (4.15)

$$\partial_t \phi = D\Delta\phi + \sqrt{\epsilon}w(\vec{x}, t) \quad (4.38)$$

we perform a Fourier transform of (4.38), obtaining

$$\partial_t \phi_k = -k^2 D\phi_k + \sqrt{\epsilon}w_k \quad (4.39)$$

by knowing that the Fourier transform of white noise is a constant, the average of ϕ^2 and $(\nabla\phi)^2$, are respectively:

$$\langle\phi^2\rangle = \int kdk \langle\phi_k^2\rangle \quad (4.40)$$

$$\langle(\nabla\phi)^2\rangle = \int k^2 kdk \langle\phi_k^2\rangle \quad (4.41)$$

Calculating the average of ϕ^2 , we get

$$\langle\phi_k^2\rangle = \frac{\epsilon}{2k^2 D} \quad (4.42)$$

so, we find that

$$\langle \phi^2 \rangle = \frac{\epsilon}{2D} \int \frac{k dk}{k^2} = \frac{\epsilon}{2D} \ln \left(\frac{k_M}{k_0} \right) \quad (4.43)$$

and for the gradient, we have

$$\langle (\nabla \phi)^2 \rangle = \frac{\epsilon}{2D} \int \frac{k^2 k dk}{k^2} = \frac{\epsilon}{4D} k_M^2 \quad (4.44)$$

Making the relationship between $\langle \phi^2 \rangle$ and $\langle (\nabla \phi)^2 \rangle$, and by keeping apart the natural logarithmic term, we obtain the factor k_M . This is why it was necessary to introduce the cutoff.

5 | Pushed genetic waves

The main regulators of ecological equilibrium and functioning are biodiversity and species interactions. The biological control exercised by living organisms establishes, in most cases, an antagonistic interaction. We focus on the dynamics of two competing species, A and B having fraction f and $1 - f$, respectively. The growth rates depend on the local fraction of the species $\mu_A = \mu_A^0 + \epsilon_A(1 - f)$ and $\mu_B = \mu_B^0 + \epsilon_B f$ where the parameters $\epsilon_A, \epsilon_B \leq 0$. As both types of species evolve next to each other, both strains incur a growth penalty. By setting μ_A^0 and μ_B^0 equal to 1, the equations governing the evolution of the two species are

$$\frac{\partial c_A}{\partial t} + \nabla(\vec{u}(r)c_A) = D\Delta c_A + c_A(1 - c_A - c_B) + \epsilon_A c_A c_B \quad (5.1)$$

$$\frac{\partial c_B}{\partial t} + \nabla(\vec{u}(r)c_B) = D\Delta c_B + c_B(1 - c_A - c_B) + \epsilon_B c_A c_B \quad (5.2)$$

where $\sigma = -(\epsilon_A + \epsilon_B)/2$ is the antagonist interaction strength and $\delta = \epsilon_A - \epsilon_B$ is the selective advantage.

We aim at investigating the properties of eq.s (5.1) and (5.2) by increasing the number of individuals, in the limit $N_0 \gg 1$ (continuum limit) and then by comparing the deterministic outcomes with the agent simulations.

5.1 Theory

We consider the equations (5.1) and (5.2) in a two dimensional system of size $L \times L$, with periodic boundary conditions and deme area a^2 . Upon defining $c = c_A + c_B$ and $f = c_A/c$ and $1 - f = c_B/c$ we get:

$$\frac{\partial c}{\partial t} + \nabla(\vec{u}(r)c) = D\Delta c + c(1 - c) + (\epsilon_A + \epsilon_B)c^2 f(1 - f) \quad (5.3)$$

The dynamic of the fraction $f(x, t)$ is given by the relation

$$\frac{\partial f}{\partial t} = \frac{1}{c} \frac{\partial c_A}{\partial t} - \frac{c_A}{c^2} \frac{\partial c}{\partial t} \quad (5.4)$$

$$= \frac{1}{c} c_A(1 - c) + \frac{\epsilon_A c_A c_B}{c} - \frac{f}{c} c(1 - c) - (\epsilon_A + \epsilon_B) c f^2(1 - f) \quad (5.5)$$

$$= \epsilon_A c_A c_B - (\epsilon_A + \epsilon_B) c f^2(1 - f) \quad (5.6)$$

$$= \epsilon_A c f(1 - f) - (\epsilon_A + \epsilon_B) c f^2(1 - f) \quad (5.7)$$

by imposing $\epsilon_A = -(\sigma - \frac{\delta}{2})$ and $\epsilon_B = -(\sigma + \frac{\delta}{2})$

$$\frac{\partial f}{\partial t} = -(\sigma - \frac{\delta}{2}) f(1 - f) + 2\sigma c f^2(1 - f) \quad (5.8)$$

$$= 2\sigma c f^2(1 - f) - \sigma f(1 - f) + \frac{\delta}{2} f(1 - f) \quad (5.9)$$

We obtain

$$\frac{\partial f}{\partial t} = f(1 - f) \left[\frac{\delta}{2} + \sigma(2f - 1) \right] c \quad (5.10)$$

Hereafter, we assume $c = 1$. The deterministic generalization of the model, flow acting in the system, is given by

$$\frac{\partial f}{\partial t} + \vec{u}(r) \cdot \vec{\nabla} f = D\Delta f + f(1 - f) \left[\frac{\delta}{2} + \sigma(2f - 1) \right] \quad (5.11)$$

We assume that the flow is expressed by the following form:

$$u_x = u_0 \sin \left(2\pi \left(x - \frac{L}{2} \right) \right) \quad (5.12)$$

$$u_y = u_0 \sin \left(2\pi \left(y - \frac{L}{2} \right) \right) \quad (5.13)$$

The stationary solution, without advection, equates to:

$$D\Delta f = -\frac{dV(f, \delta)}{df} \quad (5.14)$$

where $\frac{dV(f, \delta)}{df} \equiv 2\sigma f(1-f)(f - \frac{1}{2}) + \frac{\delta}{2}f(1-f)$. Eq. (5.14) can be interpreted as follows: f represents the position of the particle, at time x , that is subjected to a negative potential $-V$.

A theoretical framework of the deterministic equations for a radially symmetric f around the point $(L/2, L/2)$ is developed, in the limit $D \rightarrow 0$, $\sigma \rightarrow 0$, and theoretic interface width $w^2 \equiv D/\sigma$ finite and small. Let f be defined as a radial basis function

$$f(r, t) = \phi(r - R(t)) \quad (5.15)$$

The equation (5.11) can be rewritten in the radial form obtaining

$$-\frac{\partial \phi}{\partial r} \frac{dR}{dt} = D\Delta \phi + \frac{D}{R} \frac{\partial \phi}{\partial r} - u(r) \frac{\partial \phi}{\partial r} - \frac{dV}{df} \quad (5.16)$$

By spatially integrating and by multiplying by $\left(\frac{\partial \phi}{\partial r}\right)$ we get

$$-\left\langle \left(\frac{\partial \phi}{\partial r}\right)^2 \right\rangle \frac{dR}{dt} = \frac{D}{R} \left\langle \left(\frac{\partial \phi}{\partial r}\right)^2 \right\rangle - u(r) \left\langle \left(\frac{\partial \phi}{\partial r}\right)^2 \right\rangle - \int_0^\infty \frac{dV}{d\phi} \frac{\partial \phi}{\partial r} dr \quad (5.17)$$

where

$$-\int_0^\infty \frac{dV}{d\phi} \frac{\partial \phi}{\partial r} dr = \int_0^\infty \frac{dV}{d\phi} d\phi = -[V(\phi(\infty)) - V(\phi(0))] = \quad (5.18)$$

$$= V(\phi(0)) = \frac{\sigma}{2} \phi(0)^2 (1 - \phi(0))^2 - \frac{\delta}{2} \left[\frac{\phi^2(0)}{2} - \frac{\phi^3(0)}{3} \right] \quad (5.19)$$

In the case $\phi(0) = 1$, $V(\phi(0)) = -\frac{\delta}{12}$ and $\left\langle \left(\frac{\partial \phi}{\partial r}\right)^2 \right\rangle = \frac{1}{6w}$

The radial equation reads:

$$-\frac{1}{6w} \frac{dR}{dt} = \frac{1}{6w} \frac{D}{R} - \frac{1}{6w} u(r) - \frac{\delta}{12} \quad (5.20)$$

by simplifying:

$$\frac{dR(t)}{dt} = -\frac{D}{R} + u_0 \sin(2\pi R) + \frac{\delta w}{2}. \quad (5.21)$$

The eq. (5.21) is based on the following assumptions: $\phi(0) = 1$, $w/R(0) \ll 1$ and $c = 1$. The first term on the r.h.s. corresponds to the surface tension effect, the second one is linked to the velocity field, and the last one is mainly related to the sign of the selective advantage. This equation tells us whether the blob increases or decreases over time. It depends on the value of the selective advantage. If $\delta = 0$, all the competing species are selectively neutral, the blob shrinks, and without velocity field, it goes extinct. In the case of selective advantage $\delta > 0$, the presence of the velocity field enables the blob expansion. It is possible to get a critical value of δ from which the blob grows.

Another way to get the same radial equation (5.21) is by defining the following

$$D \frac{\partial^2 \phi}{\partial r^2} + 2\sigma\phi(1 - \phi) \left(\phi - \frac{1}{2} \right) = 0 \quad (5.22)$$

where eq.(5.22), can also be rewritten as

$$\phi(r, t) = \frac{1}{2} \left[1 - \tanh \left(\frac{r - R(t)}{2w} \right) \right] \quad (5.23)$$

Using (5.23) we obtain:

$$\frac{\partial \phi}{\partial r} = -\frac{1}{w} \phi(1 - \phi) \quad (5.24)$$

By inserting (5.24) in (5.11), we obtain the radial equation for the well-mixed case with $c = 1$:

$$\frac{1}{w} \phi(1 - \phi) \frac{dR}{dt} = -\frac{1}{w} \phi(1 - \phi) \frac{D}{R} + \frac{u(R)}{w} \phi(1 - \phi) + \frac{\delta}{2} \phi(1 - \phi) \quad (5.25)$$

where $u(R) = u_0 \sin(2\pi R)$. We notice that $\phi(1 - \phi)$ is strongly localized for small w in the region $r \sim R(t)$. This observation allows the approximation of the first term on the r.h.s. of (5.25) to $D/R(t)$. The final result reads

$$\frac{dR(t)}{dt} = -\frac{D}{R} + u_0 \sin(2\pi R) + \frac{\delta w}{2} \quad (5.26)$$

5.2 Deterministic transition and comparison with agent simulations

As previously mentioned, our aim is to compare the deterministic prediction against the agent simulations with finite N_0 . The eq. (5.21) can be used to predict the fate of an initial population of size $R(0)$. In the following we assume $R(0)$ to be fixed and we compute the critical value of δ above which the initial population reaches fixation in the domain. The critical value of δ is given by the following relation

$$\delta_c = \frac{2D}{wR(0)} \quad (5.27)$$

For $\delta > \delta_c$ the blob expands whereas for $\delta < \delta_c$ it goes extinct. The relation (5.27) is true under the assumptions valid for eq. (5.21). We will see that the velocity field, when present, has a not negligible effect on δ_c .

In the model, it is assumed to host on average N_0 individuals per deme. Upon defining $N_{box} \equiv (L/a)^2$, the total number of individuals N_T is given by $N_{box} \times N_0$. Therefore the continuous limit is achieved by increasing N_0 .

The set of parameters for the numerical investigations are: the size of the system $L = 1 = 128 \times a$, the diffusion $D = 0.0009$, the interface width $w \sim 0.05$ and the interaction strength $\sigma = 0.36$.

The assumptions made on the finite size of the system are analyzed in the following:

- 1. $R(0)$ is known up to a a . The error on $R(0)$ is of the order of $\frac{a}{R(0)}$, and the equation for the critical value of δ becomes $\delta_c = \frac{2D}{w(R(0)-a)}$.
- 2. The value of $\phi(0)$ is not equal to 1, but it is slightly smaller.
- 3. The assumption $c = 1$ is never true for any finite σ . There is an effect due to $c \neq 1$.

Two values of the radius $R(0)$, $R(0) = 0.125$ and $R(0) = 0.21$ are considered, so that the ratio $w/R(0)$ is never small. A reasonable estimate of the error due to the finite discretization can be obtained by assuming both w and $R(0)$ known with an accuracy of $\pm a/2$. The overall error is therefore $(a/w + a/R(0))/2 \sim 0.1$.

Using eq.(5.3) we can argue that a better approximation is given by

$$c(x, y) = \frac{1}{1 + 2\sigma\phi(1 - \phi)} \quad (5.28)$$

Thus, at the interface, for $\sigma = 0.36$ we get $c = 1./1.18$, the effect of which is not negligible in determining δ_c .

Since c is not constant, we must take care of the effect induced by the neglected term $2\nabla f \frac{\nabla c}{c}$. This term is found in the steps between the equation (5.3) and the equation (5.11).

By using eq.s (5.23) and (5.24) we can write:

$$\begin{aligned} 2D\nabla\phi\nabla\log(c) &= -2D\nabla\phi\frac{2\sigma(1-2\phi)}{1+2\sigma\phi(1-\phi)}\nabla\phi & (5.29) \\ &= \frac{4D\sigma}{w}\nabla\phi\frac{(1-2\phi)\phi(1-\phi)}{1+2\sigma\phi(1-\phi)} \end{aligned}$$

Eq. (5.29) suggests that everything goes as if the system is affected by a self-induced velocity field $U_{eff}(r)$ given by

$$U_{eff} \equiv -\frac{4D\sigma}{w}\frac{(1-2\phi)\phi(1-\phi)}{1+2\sigma\phi(1-\phi)} \quad (5.30)$$

So that:

$$2D\nabla\phi\nabla\log(c) = -U_{eff}(r)\nabla\phi \quad (5.31)$$

The "velocity" U_{eff} is exactly zero at the interface and one may think it has no effect on the interface dynamics. However, because U_{eff} represents a sink, it tends to oppose any increase of the initial radius $R(0)$. Thus, we can expect that the term (5.29) leads to an increase of the critical value of δ .

Now, looking at the quantitative results, we consider three different no-flow cases. The first two cases have as initial condition a blob of radius $R(0)$ equal to 0.125 and 0.21, respectively. The third case takes into account an initial condition having a homogenous strip in the y direction of size $2R(0)$, where $R(0)$ corresponds to $R(0) = 0.0625$.

Figures 5.1 and 5.2 show the cases for bubbles of radius $R(0) = 0.125$ and radius $R(0) = 0.21$ respectively, as initial conditions. Figure 5.3 shows the case of a strip with initial size $2R(0)$ with $R(0) = 0.0625$. The two vertical lines, the red dot-dashed line and the red continuous line display the critical value of δ at which a transition to $\phi = 1$ is observed: the red dot-dashed line is obtained assuming $c = 1$ and it is highlighted with an arrow. The symbols, whose shapes correspond to different values of N_0 , are fitted by a black dashed curve and represent the agent simulations.

In the strip case, the effect of surface tension can be considered negligible although for

small $R(0)$ we do expect a finite value of δ for the transition to occur.

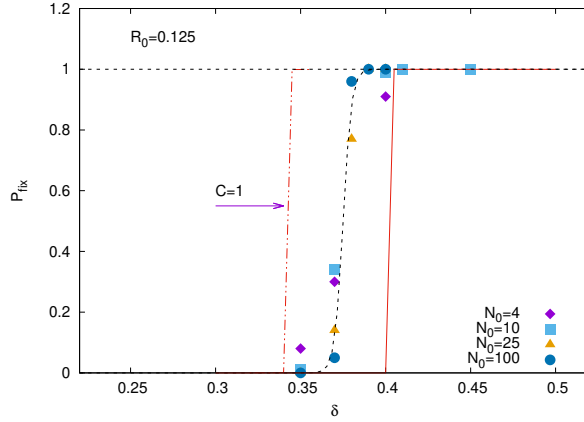


Figure 5.1: Critical value of δ to let the transition to $\phi = 1$ occur. The initial state is a blob of radius $R(0) = 0.125$. By increasing δ a transition represented by the red continuous vertical line is observed, whereas the red dot-dashed vertical line, at smaller δ , corresponds to the solution of eq. (5.11) with $c = 1$. The symbols refer to the agent simulations with different values of $N_0 = 4, 10, 25, 100$ and are fitted by a black dashed curve.

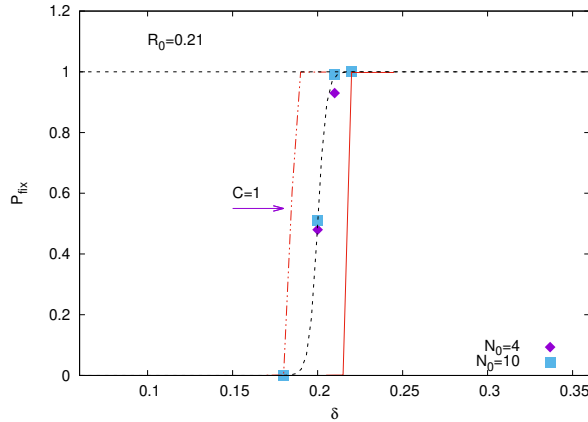


Figure 5.2: Critical value of δ to let the transition to $\phi = 1$ occur. The initial state is a blob of radius $R(0) = 0.21$. By increasing δ a transition represented by the continuous vertical line is observed, whereas the red dot-dashed vertical line, at smaller δ , corresponds to the solution of eq. (5.11) with $c = 1$. The symbols refer to the agent simulations with different values of $N_0 = 4, 10$ and are fitted by a black dashed curve.

The obtained no-flow results with agent simulations indicate that the critical value of δ , for finite N_0 , is always in between $\delta_c(c = 1)$ and $\delta_c(c \neq 1)$. We observe a rather strong convergence, sketched by a sharp transition, already with $N_0 = 10$.

5

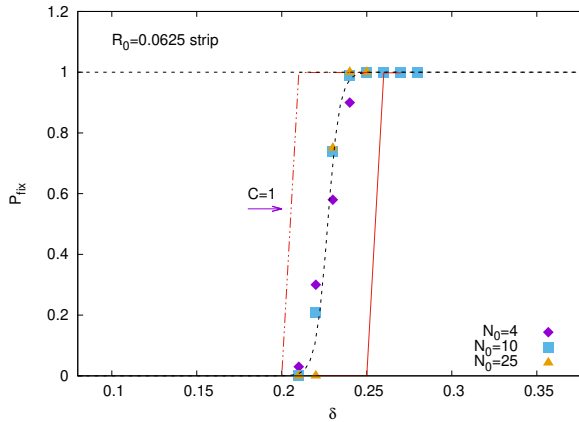


Figure 5.3: Critical value of δ to let the transition to $\phi = 1$ occur. The initial state is a strip with size $2R(0)$, $R(0) = 0.0625$. By increasing δ a transition represented by the red continuous vertical line is observed, whereas the red dot-dashed vertical line, at smaller δ , corresponds to the solution of eq. (5.11) with $c = 1$. The symbols refer to the agent simulations with different values of $N_0 = 4, 10, 25$ and are fitted by a black dashed curve.

The heterozygosity is a useful tracer to understand the dynamics of the interface. We investigate the case of the blob with $R(0) = 0.125$ (fig. 5.1) by setting $\delta = 0.38$. In particular, a one-dimensional cut of $\phi(r, t)$ at $y = L/2$ (at the initial position of the population) is considered and the heterozygosity $H(x, t) = \phi(1 - \phi)$ for $y = y_0 = 1/2$ is computed. In figure 5.4 the heterozygosity $H(x, t)$, as a function of both space x (y-axis) and time t (x-axis), is shown. The heterozygosity at its maximum $H(x, t) = 0.25$ (yellow color) corresponds to $\phi = 1/2$. The figure illustrates quite clearly the behavior of the interface over time: at the early stage, the transient behavior shows a weak shrink of the system followed by an almost linear growth with time. Interestingly none of the interfaces at $\phi = 1/2$ fluctuates, i.e. the region $\phi = 1/2$ does not perform any random behavior as one usually observes at the interface between neutral populations. This indicates that the behavior observed should be close to the one observed in the limit for $N_0 \rightarrow \infty$.

5

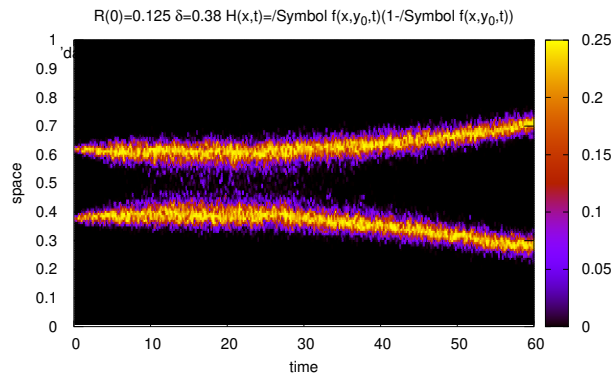


Figure 5.4: Space vs time visualization of the interface dynamics. The cross-section at $y \equiv y_0 = 1/2$ of an initial blob of radius $R(0) = 0.125$ is considered, (see figure 5.1). The heterozygosity $H(x, t) = \phi(x, y_0, t)(1 - \phi(x, y_0, t))$ whose maximum corresponds to the yellow color $H(x, t) = 0.25$, is shown.

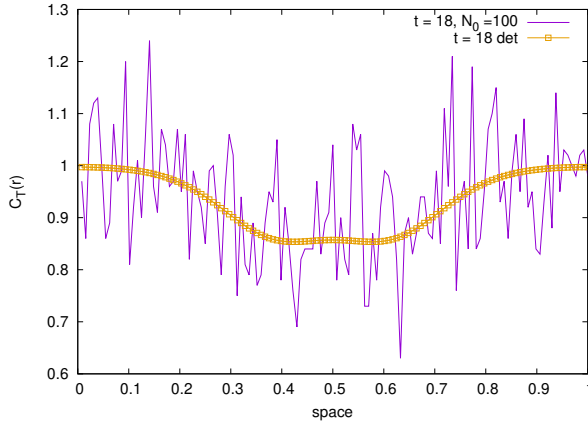


Figure 5.5: Cross-section $c(x, y_0, t)$ of the total population size $c_T(r)$, for $y \equiv y_0 = 1/2$, by setting time at $t = 18$ and selective advantage at $\delta = 0.41$. The orange-dotted line refers to the deterministic solution of eq. (5.11) while the purple continuous line corresponds to the agent simulations for $N_0 = 100$.

In figure 5.5, the cross-section $c(x, y_0, t)$ of the total population size $c_T(r)$ for $y \equiv y_0 = 1/2$, at time $t = 18$ and selective advantage at $\delta = 0.41$ is shown. By integrating the equations (5.11) and (5.3) we get the orange-dotted line while the purple continuous line displays the agent simulations results obtained for $N_0 = 100$.

5

Reasonable evidence that emerges is that the region near the centre of the initial population $x = 1/2$ is characterized by a lower value of c as expected for the deterministic solution. The agent simulations for $N_0 = 100$ show quite remarkable fluctuations order $O(N_0^{-1/2})$ around an average value close, or just like, the solution of the deterministic case. These fluctuations, on average, tend to smear the effect of the self-induced velocity field analyzed in eq.s (5.30), (5.31) which is strongly linked to the functional form of $\phi(x, y, t)$ in (5.23). This may explain why the agent simulations show a transition at a critical value of δ in between the $\delta_c(c = 1)$ and $\delta_c(c \neq 1)$. Eventually, the convergence to the deterministic case, if any, may be extremely low since the r.m.s fluctuations on ∇c should be of order $1/(aN_0^{1/2})$ with a the deme size. To summarize the results, there is a rather good quantitative agreement of the agent simulations with the deterministic dynamics within the accuracy provided by the present resolution.

5.3 Effect of the source field

We now consider the effect of a weak compressible velocity field acting in the two-dimensional system, given by the two components (5.12) and (5.13). In the equation

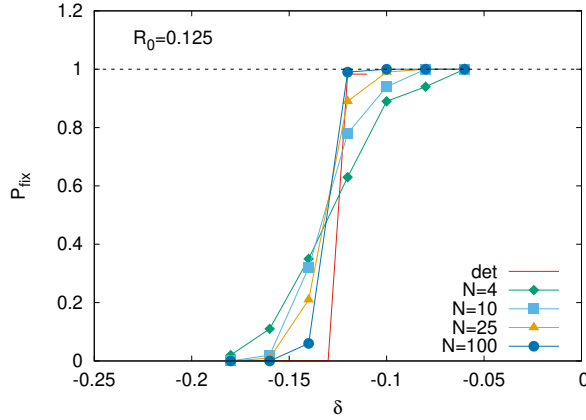


Figure 5.6: Critical value of δ to let the transition to $\phi = 1$ occur, with a source advection $u_0 = 0.02$. The initial state is a blob of radius $R_0 = 0.125$. By increasing δ we observe a transition represented by the red continuous vertical line. The symbol lines refer to the agent simulations with different values of $N_0 = 4, 10, 25$.

(5.12) $u_y = 0$ is set. We assume all the parameters equal to the cases discussed in the figures 5.1-5.3, setting the constant value of the velocity field $u_0 = 0.02$.

Let us denote by $\delta_c[R(0), u_0]$ the critical value of δ above which the initial population grows and reaches fixation. Let also be $\delta_c[R(0), 0] \equiv \delta_c(c \neq 1)$, the critical value of δ for $u_0 = 0$. Using eq.(5.21) we can predict the value $\delta_c[R(0), u_0]$ by the relation:

$$\delta_c[R(0), u_0] = \delta_c(R(0), 0) - \left(\frac{2u_0 \sin(2\pi R(0))}{w} \right) \quad (5.32)$$

Eq. (5.32) is supposed to hold both for the deterministic case (corresponding to $N_0 = \infty$) and for the agent simulations, within an accuracy similar to the ones previously discussed in the no-velocity cases.

We can easily see that the simulations with agents and the deterministic results converge ever more by increasing the number of species present in the deme.

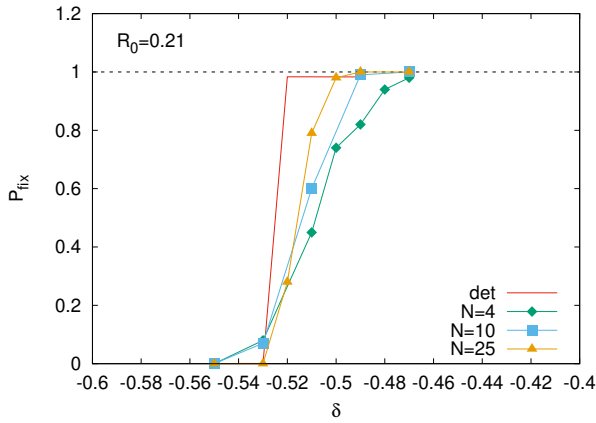


Figure 5.7: Critical value of δ to let the transition to $\phi = 1$ occur, with a source advection $u_0 = 0.02$. The initial state is a blob of radius $R_0 = 0.21$. By increasing δ we observe a transition represented by the red continuous vertical line. The symbol lines refer to the agent simulations with different values of $N_0 = 4, 10, 25$.

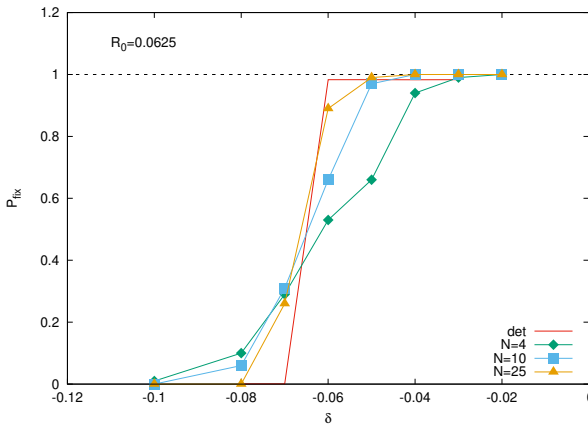


Figure 5.8: Critical value of δ to let the transition to $\phi = 1$ occur, with a source advection $u_0 = 0.02$. The initial state is a strip with size $2R(0)$, $R(0) = 0.0625$. By increasing δ we observe a transition represented by the red continuous vertical line. The symbol lines refer to the agent simulations with different values of $N_0 = 4, 10, 25$.

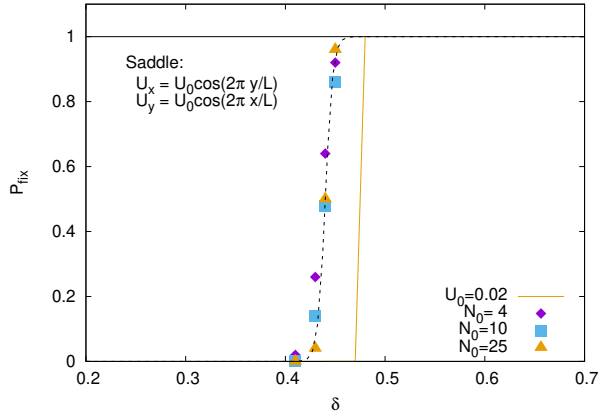


Figure 5.9: Critical value of δ for a transition to $\phi = 1$ with a source advection with $u_0 = 0.02$ (yellow continuous line). The initial state is a blob of radius $R(0) = 0.125$ and the velocity field is given by eq. (5.33) and (5.34). The symbols refer to agent simulations with different values of $N_0 = 4, 10, 25$.

5.4 Incompressible flow

In this section, we now consider the transition in δ for fixed $R(0)$ when the system is advected by the following incompressible flow:

$$u_x = u_0 \cos\left(2\pi\left(y - \frac{L}{2}\right)\right) \quad (5.33)$$

$$u_y = u_0 \cos\left(2\pi\left(x - \frac{L}{2}\right)\right) \quad (5.34)$$

In figure 5.9 we show P_{fix} as a function of δ for $R(0) = 0.125$ for $u_0 = 0.02$. The deterministic transition is represented by the continuous yellow line for $u_0 = 0.02$. The filled symbols refer to the agent simulations.

As we have already observed, for $N_0 = 10$ we already reach a good convergence in the simulations to measure the transition point which is $\delta_c = 0.44$ for $u_0 = 0.02$. The transitions for the agent simulations are rather close to the deterministic one.

5.5 Conclusions

We based our study on the probability of fixation between two populations with an antagonistic interaction. In particular, the case of two populations whose dynamics is

confined in a closed two-dimensional structure $L \times L$ with periodic boundary conditions and eventually advected by a weak compressible velocity field is taken into account.

We focus our investigation on two separate scenarios. In the first scenario, the initial spatial distribution of the fraction f of a species (for example A), at $t = 0$, is radially symmetric delimitate around $L/2, L/2$. In the second scenario, f corresponds to a homogeneous strip in the y direction of size $2R(0)$. Upon finding the functional form, a framework to analyze the deterministic equations is developed. The deterministic results obtained for an initial population are compared with the agent simulations.

We analyzed the dynamics by increasing the number of individuals per deme such that the solution of eq.s (5.1) and (5.2) approaches the continuum description. The results obtained by the use of agent-based simulations were compared to those deterministic with the object to understand the role of number fluctuations in population genetics.

By examining the numerical simulations we observed that the carrying capacity cannot be set at its maximum $c = 1$ for any antagonist interaction strength. In the case of no velocity field, we discover that the critical value of the selective advantage shows a transition always in between $\delta_c(c = 1)$ and $\delta_c(c \neq 1)$, and eventually convergence to the deterministic solution but very slowly.

To understand the dynamics at the interface we study the heterozygosity as a tracer. It is noticed that, after an initial moment of shrinking, the transient behavior shows a linear growth. Then, by taking a cross-section of the total population with space, it is observed that the remarkable fluctuations are around an average value close to the deterministic solution.

On average, these fluctuations can reduce the effect of the effective velocity and in the long-run they could eventually minimize the differences at the interface.

The case of a weak compressible and incompressible velocity field is then investigated. As for the case without velocity field, we find net agreement between the deterministic results and the agent simulations as the number of individuals per deme increases.

6 | Concluding remarks and outlook

In this thesis, we have explored the effect that individual dispersion has on a population genetics under compressible flow conditions.

The proposed computational method enables the analysis in continuous space with an efficiency comparable with the discrete lattice case. Efficient computation is possible with an extremely large number of individuals per site, without managing the position of each individual.

We assume a uniform lattice of spacing Δx with each site occupied by N_j individuals. At each time step, we redistribute the N_j individuals on a domain $(1+a)\Delta x d$, where d is the dimension of our system and a is suitably chosen to introduce a diffusion process. Next, we advect the N_j individuals in continuous space using the external velocity, if present. After this step, some of the original N_j individuals have been moved to different regions of space, i.e., to a different box of size Δx , changing the number of individuals of the new box. Once we complete the diffusion and advection for all sites, independently one from another, we apply the birth-death processes stochastically according to the prescribed rates. Note that we do not need to remember the exact position in each site from one step to another, and it is enough to know how many individuals of each species are present at the prescribed site. In this way, we can efficiently work with an extremely large number of individuals per site without managing the position of each individual. This is actually the reason why we can achieve a significant increase in computational performance.

By applying this method in presence of a two-dimensional weakly compressible flow, we discovered that the dynamics of populations can be strongly influenced especially when the individuals are sited within a source of the flow. This is an important result for a two-dimensional system.

The introduced original method has allowed us to analyze specific cases of interest. As a

preliminary examination we set off on the strong noise regime to figure out if, in such a case, the probability of fixation remains unaffected by the system's diffusivity. This has been validated through a rigorous theoretical analysis and simulation process by means of the original code. We have also investigated the impact of incompressible flow advection in a real scenario.

A further approached aspect of population dynamics concerns the antagonistic interaction between species. This aspect has important repercussions on the microbial evolutionary dynamics. We considered a spatially extended dynamics on which eventually weak compressible flows acts. By analyzing different initial population sizes, it turns out that by increasing the number of individuals, per deme, agent simulations converge to the deterministic results. This result is found both without a velocity field and when a weak compressible velocity field is activated.

Below, in the appendix, a study concerning the microorganism's physical properties in terms of confinement in relation to the diffusivity parameter is added. The *Escherichia Coli*, characterized by a swimming mechanism known as run-and-tumble, has been considered. The microorganism motion is characterized by an effective diffusivity that can vary according to the type of confinement. The swimmer is stuck in circular orbits near stable walls in a weak containment. When the tumbling frequency is equal to the angular velocity of the stable orbits, optimum diffusivity is observed. The stable circular orbits vanish in strong confinement, and the diffusion coefficient decreases monotonically with the tumbling rate. Our findings can be potentially applied to other, both natural and artificial, chiral swimmers. Indeed, several asymmetric swimmers follow circular trajectories when moving close to boundaries, see e.g. [76, 77] and, in principle, can present an optimal tumbling rate that maximizes their diffusivity.

A | Diffusivity of E. coli-like microswimmers in confined geometries: The role of the tumbling rate

So far, diffusivity has been analyzed as a simple numerical parameter, however, the diffusivity dependence on the properties of the considered organism should also be taken into account. The whole can also vary in relation to a strong density gradient, so if the system is confined and depends on the given confinement, the correlated diffusivity of the organism varies. In the following section, the effect of confinement on the effective diffusion of a run-and-tumble E. coli like flagellated microswimmer is analyzed.

The run phase is obtained via a fully resolved swimming problem, i.e. the Stokes equations for the fluid coupled with the microorganisms rigid body dynamics. Tumbles events and collisions with the walls are modelled as random reorientation of the microswimmer. For weak confinement, the swimmer is trapped in circular orbits close to the solid walls. In this case, optimal diffusivity is observed when the tumbling frequency is comparable with the angular velocity of the stable orbits. For strong confinement, the stable circular orbits disappear and the diffusion coefficient monotonically decreases with the tumbling rate. Our findings can be potentially applied to several natural or artificial chiral microswimmers that follow circular trajectories close to an interface or in confined geometries.

The following study is not part of the doctoral project. it was developed for the master's thesis project and it was published during the first year of PhD.

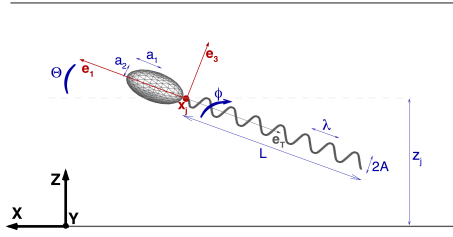


Figure A.1: Flagellated bacterium model and channel geometry. The flagellated microswimmer is modelled as a system of two rigid bodies, the head (a prolate ellipsoid) and the tail (an helical tubular structure). The head and tail axes lie along the same direction and the tail can rotate with respect to the head. The system has 7 degrees of freedom, namely the position \vec{x}_j of the junction between the head and the tail, the orientation of the head with respect to the fixed reference frame and the rotation angle ϕ of the tail with respect to the head. In the plane channel geometry, the only relevant degrees of freedom are the distance between the junction and the wall z_j and the angle Θ between \vec{e}_1 and \vec{x} .

A.1 Methods

The microswimmer is composed by two rigid bodies, the head and the tail, see fig. A.1. The head is a prolate ellipsoid with longitudinal and transverse semi-axis called a_1 and a_2 respectively. The swimmer head position is identified by the junction between head and tail \vec{x}_j , that is also taken as the origin of the body reference frame $\{\vec{e}_1, \vec{e}_2, \vec{e}_3\}$ where the unit vector \vec{e}_1 lays along the longer ellipsoid axis. The body translational velocity is denoted by \vec{U} while $\vec{\Omega}_H$ is the angular velocity of the head. The tail is modelled as a helix of wavelength λ , amplitude A and axis $\vec{e}_t = -\vec{e}_1$, being L the axial length of the tail which has a cross section of radius a_T . Following [60], the tail originates from the head at the junction point \vec{x}_j with vanishing small amplitude. Then, the helix amplitude grows up to A with an exponential law. The tail rotates around \vec{e}_t with angular velocity $\Omega_T = \dot{\phi}$. The microswimmer kinematics is completely defined by six degrees of freedom as appropriate for a free rigid body, plus the rotation angle of the tail $\phi(t)$. An internal torque of intensity τ_M , aligned with \vec{e}_1 , is exchanged between the head and the tail, so that the tail rotates around its axis and the head balances this motion by counter-rotating.

The hydrodynamics of the bacterium in presence of confinement is described by the Stokes equations

$$-\nabla p + \mu \nabla^2 \vec{u} = 0 \quad , \quad \nabla \cdot \vec{u} = 0. \quad (\text{A.1})$$

For liquid water on a solid surface, the intrinsic slippage is negligible [78, 79]. Hence, the no-slip boundary condition is appropriate for both the rigid wall and the microswimmer

surfaces. The solution of the Stokes equations is achieved by using the corresponding boundary integral equation, see e.g. [80]. In this Boundary Element Method (BEM) approach, the fluid boundaries, i.e. the microswimmer head and tail and the confining walls, are discretized by means of N triangles. The discrete form of the boundary integral equation results in a linear system of $3N$ equations relating the three velocity components to the three components of stresses over the N boundary elements. The velocity on each boundary element of the microswimmer surface depends on \vec{U} , $\vec{\Omega}_H$ and Ω_T , which represent seven further unknowns. Seven additional equations, namely the free-body balance equations (3 scalar equations for the forces and 3 for the torques) and the equation for the internal torque balance close the system, see e.g. [60, 61] for more details. The complete system ($3N + 7$ equations) is solved by a parallel Gauss-Jordan algorithm [81] implemented in an in-house code [61, 82]. A similar approach can be employed also for squirmers, see e.g. [83].

In principle, the solution of the system allows to set up a simple time marching algorithm for evaluating the dynamics of the microswimmer. At each time step, given the torque τ_M , the system is solved and the swimmer velocities can be employed to update the microswimmer configuration. Following Shum et al. [60, 84], the system symmetries can be exploited to set up a more efficient approach. In brief, since the system is invariant under rotation around the z -axis and translation in x and y directions, it is convenient to pre-calculate the velocities when the bacteria sits in specific positions in the reduced space (Θ, z_j) with Θ the (pitch) angle between the \vec{e}_1 body axis and the bottom wall and z_j the z -coordinate of the junction position \vec{x}_j , see figure A.1. The tail rotational velocity $\phi(t) = \Omega_T$ is much larger than the other velocities involved in the problem. This calls for averaging on the tail rotation ϕ , thus the swimmer translational velocity \vec{U} and its angular velocity $\vec{\Omega}_H$ only depend on Θ and z_j . The bacterium trajectory during the run phase is then calculated integrating the rigid body kinematics equations of the swimmer head, where \vec{U} and $\vec{\Omega}_H$ are interpolated from the pre-calculated values on a discrete set of Θ, z_j pairs.

The tumbling phase is achieved by randomly rotating \vec{e}_1 by an angle ψ to a new orientation \vec{e}'_1 which lies on a cone of axis \vec{e}_1 and semi-amplitude ψ . The tumbling occurs at a fixed frequency α . Moreover, a tumbling event is also triggered when the swimmer collides with the wall. It is worth noting that, in the limit of $\alpha \rightarrow 0$, our model is not expected to reproduce the swimmer dynamics on long time scales. Indeed, in absence of tumbling (or for very low tumbling rates α) the swimmer will still deviate from the deterministic trajectory due to rotational diffusion, see e.g. [85].

We performed simulations where ψ is not constant but is extracted, from each tumbling event, from a uniform distribution of mean value ψ . The overall behaviour of the diffusivity as a function of the tumbling rate is the same as the constant ψ case (data not shown).

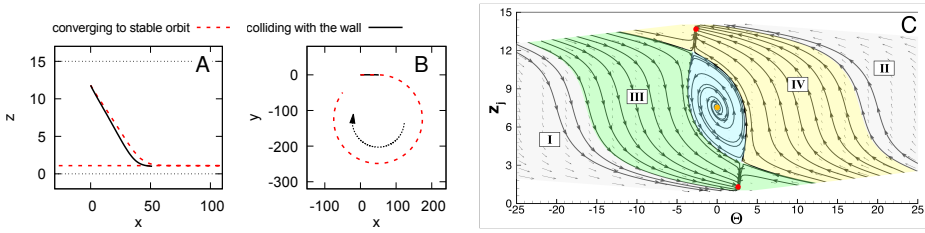


Figure A.2: Deterministic microswimmer trajectory for a boundary accumulating case. Panels A and B report xz and xy projections of the 3D trajectory for two initial conditions. Red (dashed) line: the swimmer stabilizes on a closed circular orbit. Black (solid) line: the swimmer collides with the wall. The reduced (Θ, z_j) phase space is represented in the panel C. The color refers to the different manifolds. Trajectories originating from the grey regions (I and II) eventually collide with the wall. Trajectories originating from green (III) and yellow (IV) regions are attracted to one of the two stable orbits (red points close to the walls). Channel height, $h = 15$. Microswimmer geometry; tail length $L = 5.31$, tail amplitude $A = 0.286$, tail wavelength $\lambda = 1.8$, tail radius $a_t = 0.05$, cell equivalent radius $a = 1.0$ with $a_2/a_1 = 0.33$.

In the following, the equivalent cell radius \bar{a} , defined as the radius of a sphere having the cell volume, is used as a reference length. The reference time unit is set as the time needed by the flagellum to perform a complete rotation with respect to the swimmer head in the free space. Unless explicitly indicated, we report our data in dimensionless units built with these reference length and time scales.

A.2 Weak confinement: Boundary accumulation

Deterministic motion. We start our analysis considering a microswimmer with tail axial length $L = 5.31$, tail amplitude $A = 0.286$ and tail wavelength $\lambda = 1.8$, tail radius $a_t = 0.05$, cell equivalent radius $a = 1.0$ with $a_2/a_1 = 0.33$, moving in a channel of height $h = 15$. As a first step, we discuss the deterministic dynamics, i.e. no tumbling events are introduced. The microswimmer is attracted by the walls and two different behaviors are observed depending on the microswimmer initial condition, namely, *i*) the swimmer collides with the channel boundaries or *ii*) it stabilizes on a circular trajectory close to one of the two walls. Figure A.2 reports two typical trajectories corresponding to case *i* (black solid line) and *ii* (red dashed line). The xz and xy projection of the 3D trajectory are shown in panel A and B, respectively. When the swimmer achieves a stable orbit, in agreement with previous findings [58, 61, 86], the bacterium follows a clock wise (CW) trajectory when observed from the liquid phase. A more synthetic representation of the microswimmer dynamics is given in terms of the vector field Θ, U_z in the reduced phase space (Θ, z_j) , see figure A.2C. Asymptotically stable equilibrium points, corresponding to circular trajectories in the 3D view, are apparent at both walls

(red dots), while an unstable point is present at $\Theta = 0, z_j = h/2 = 7.5$ (yellow dot).

In this representation, the white regions (e.g. low z_j for $\Theta > 0$) correspond to configurations where the swimmer body intersects the channel walls. For the sake of clarity, only the relevant portion of the reduced phase space (Θ, z_j) is reported. Regions I and II extend for $\Theta < 25^\circ$ and $\Theta > 25^\circ$, respectively. Indeed, for large negative Θ the deterministic trajectory of the swimmer always collides with the lower wall, while, for large positive Θ , the swimmer collides with the upper wall.

Run and Tumble. We then analyzed the run and tumble motion. The tumbling phase is achieved by randomly rotating \vec{e}_1 by an angle ψ at a fixed frequency α . A tumbling event is also triggered when the swimmer collides with the wall. The dynamics strongly depends on the tumbling rate α . Indicated as ω_s the angular velocity of the circular motion of the stable deterministic orbit, for $\alpha \ll \omega_s$, the swimmer is trapped on a stable orbit for a long time before a tumbling event allows it to escape. On the other hand, for $\alpha \gg \omega_s$, the run phase is too short to appreciate circular arcs. The effective diffusion D as a function of α is reported in figure A.3A for a tumbling angle $\psi = \pi/3$. D has a maximum for $\alpha = \alpha^* \simeq 0.5\omega_s$. The trajectory corresponding to the maximum diffusion is reported in red in figure A.3B,C. It is apparent that, in this case, the swimmer covers only a small portion of a circle before a tumbling event brings it on another circular orbit. Blue and green trajectories in figure A.3B,C correspond to the cases $\alpha \ll \omega_s$ and $\alpha \gg \omega_s$, respectively. The existence of an optimal tumbling rate was early proposed in [63]. Their model indicates that $\alpha^* = \omega_s$ in fair agreement with our results.

A similar scenario occurs for different tumbling angle ψ . The $D(\alpha)$ plots always show a single peak even though the optimal tumbling rate α^* changes with ψ , see figure A.4A. The data points are roughly fitted by $\alpha^*/\omega_s = 1/\psi$, dashed red line. The following simple geometrical argument, sketched in figure A.4B supports this finding. Let us assume that the motion occurs on a plane and that the trajectory during the run phases are circular. In addition, we assume that \vec{e}_1 is aligned along the tangent of the trajectory. During each run phase the microswimmer covers an angle ω_s/α . The net displacement after a single run phase is the chord length l (red dashed line) corresponding to the angle ω_s/α . Then, the swimmer tumbles, i.e., in the present 2D approximation, it rotates of an angle ψ either to the left or to the right and a second run phase begins. At the end of the second run phase, the maximum displacement with respect to the initial position occurs when the chord of the second run phase is aligned to the displacement of the first run. This optimal circumstance is verified only when $\psi = \omega_s/\alpha$ and only for one half of the tumbling events. All the other combinations of α and ψ result in smaller displacements.

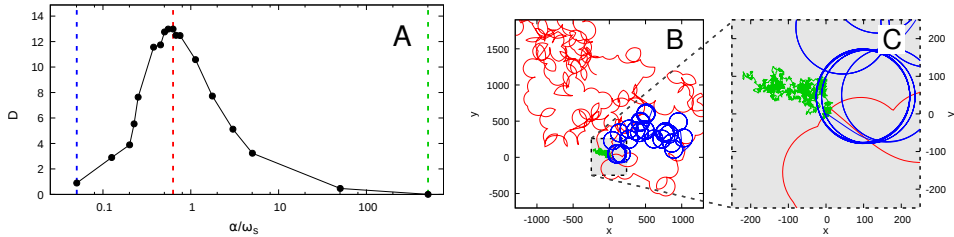


Figure A.3: A) Effective diffusion coefficient D as a function of the tumbling rate α for boundary accumulating microswimmers (same geometry as in figure A.2) for tumbling angle $\psi = \pi/3$. The tumbling rate α is normalized with the frequency ω_s corresponding to the stable circular motion observed for the same microswimmer in absence of tumbling. B,C) Examples of trajectories corresponding to for low tumbling rate (blue), optimal tumbling rate (red) and high tumbling rate (green).

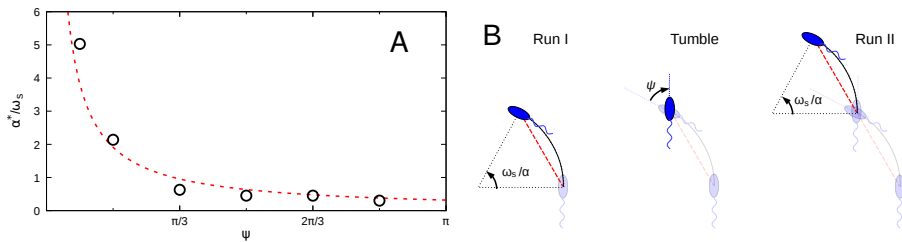


Figure A.4: A) Optimal tumbling rate α^* as a function of the tumbling angle ψ for a boundary accumulating case (same geometry as in figure A.2). Red dashed line corresponds to the relation $\alpha^*/\omega_s = 1/\psi$. B) Sketch of the geometrical argument discussed in the text. In a 2D model where the swimmer moves along circles during the run phase, the maximum possible displacement after two consecutive run phases is obtained when the displacement vectors are aligned (red lines correspond to the chord of the circular trajectories).

A.3 Strong confinement: Boundary escaping

In this section, we present the results for a narrow channel of height $h = 3.75$. Under strong confinement, the deterministic motion is no longer characterized by stable circular orbits near the walls. Swimmers that do not collide with the walls, after an initial oscillating transient, stabilize in a straight trajectory along the channel's midplane, see figures A.5A and B. As in the previous section, black solid line refers to a swimmer colliding with the wall, while an example of asymptotic trajectory is reported by the red dashed line. The 3D trajectory corresponds to the red point located at the center of the (Θ, z_j) reduced space, see figure A.5C. This phenomenology is indicated as boundary escaping [84]. The transition between boundary accumulating and boundary escaping behaviours as the channel height h is reduced was observed in [84] for different swimmer geometries.

For strong confinement, several regions on the (Θ, z_j) reduced space correspond to configurations where the swimmer body intersects the channel walls and are reported as white regions in figure A.5C.

The absence of the stable circular orbits has a dramatic effect on the dependence of the effective diffusion coefficient D on the tumbling rate α . Figure A.6 reports D as a function of α for different values of the tumbling angle ψ . It is apparent that the diffusion coefficient D decreases with α . The data are roughly aligned onto a straight line suggesting that the dependence $D(\alpha)$ can be captured by a power law whose scaling exponent and prefactor, in principle, depend on the tumbling angle ψ . In the following, we discuss a simple theoretical model that explain the observed data.

Random flight model. Let us consider a swimmer moving on a plane. During the run phase, the swimmer covers a segment of length $l = v\tau$, where $\tau = 1/\alpha$ is the time between two consecutive tumbling events and v is the swimmer speed. The displacement during the i -th run phase is indicated as \vec{r}_i , while $\vec{R}(N_t) = \sum_i^{N_t} \vec{r}_i$ is the swimmer displacement at time t after $N_t = t/\tau$ tumbles. For uncorrelated tumbling events, $\langle \vec{r}_i \cdot \vec{r}_j \rangle = 0$. Following [87] the variance of the displacement is

$$\langle \vec{R}^2(t) \rangle = N_t l^2 = \frac{v^2}{\alpha} t. \quad (\text{A.2})$$

Consequently, the resulting diffusion coefficient is

$$D = \frac{v^2}{4\alpha}. \quad (\text{A.3})$$

This kind of reasoning can be extended to the case where the tumbles occur with a specific tumbling angle ψ . Now, the tumbling directions are correlated. More specifically, the

generic displacement vector \vec{r}_i always forms an angle ψ with the previous displacement \vec{r}_{i-1} . It follows that $\langle \vec{r}_i \rangle = \vec{r}_{i-1} \cos \psi$. Following [87] the correlation $\langle \vec{r}_i \cdot \vec{r}_j \rangle$ can be calculated in a recursive manner starting from the initial condition $\langle \vec{r}_j^2 \rangle = l^2$, namely $\langle \vec{r}_i \cdot \vec{r}_j \rangle = l^2 (\cos \psi)^{|i-j|}$.

This result is successively used to compute the variance of the displacement [87]

$$\langle \bar{R}^2(t) \rangle = \frac{v^2}{\alpha} \frac{1 + \cos \psi}{1 - \cos \psi} t. \quad (\text{A.4})$$

Consequently, the diffusion coefficient D reads

$$D = \frac{v^2}{4\alpha} \frac{1 + \cos \psi}{1 - \cos \psi}. \quad (\text{A.5})$$

Equation (A.5) diverges for $\psi \rightarrow 0$, i.e. tumbling is not effective since the \vec{e}_1 is not rotated. Moreover, eq. (A.5) is valid only in the limit of large N_t . This limit is fully reached in the simulation data reported in figure A.6, where N_t ranges from 10^4 (for the lowest α) to 10^7 (for the largest α). The prediction of this simplified model well describes the data shown in figure A.6. In particular, when fitting the diffusion coefficient by a power law $D = c \alpha^b$, the scaling exponents range from $b \simeq -0.9$ for tumbling angle $\psi = \pi/3$ to $b \simeq -1.25$ for $\psi = 5\pi/6$. The prefactor c is in fair agreement with eq. (A.5), see inset figure A.6, where the actual prefactor (symbols) is compared with the expression appearing in eq. (A.5) (dotted line).

The model predicts a divergence of the diffusion coefficient for $\alpha \rightarrow 0$ as also shown by our data. It is worth noting that, for actual swimmers, at low α the dynamics will be dominated by the rotational diffusion of the swimmer body. In this more realistic case, as showed in [85], it is reasonable to expect that, for $\alpha \rightarrow 0$, D reaches a finite value.

A

In order to complete the study concerning the effects of confinement on the motion of the swimmer, we have considered a case of intermediate channel height, $h = 7.5$. The corresponding results are shown in figure A.7. Swimmers that do not collide with the walls are now found to stabilize on oscillating trajectories parallel to the channel midplane, see figure A.7A. This behaviour was also observed in early studies with similar swimmer model [84] and a more simplified pusher swimmer model [88]. These 3D trajectories correspond to a limit cycle in the reduced (Θ, z_j) phase space, see figure A.7B. The point $\Theta = 0, z_j = h/2$, yellow dot in figure A.7B, is now an unstable equilibrium point. Trajectories originating from the inside (region III_a) or from the outside (region III_b) of the limit cycle, converge to the limit cycle after a few oscillations in both z_j and Θ . Hence, also for $h = 7.5$, a boundary escaping scenario takes place, i.e. the swimmer is not

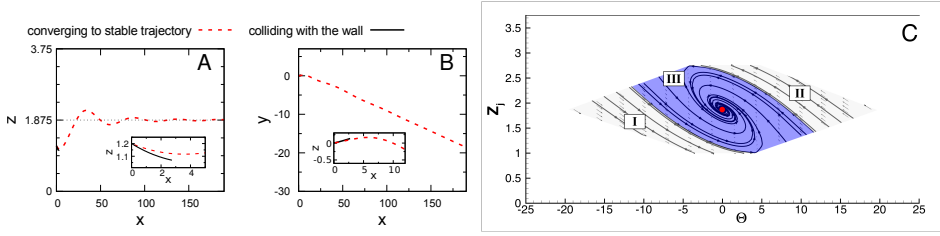


Figure A.5: Deterministic microswimmer trajectory in a boundary escaping case. Panels A and B report xz and xy projections of the 3D trajectory for two initial conditions. Red (dashed) line: the swimmer stabilizes on a trajectory parallel to the channel midplane. Black (solid) line: the swimmer collides with the wall. The reduced (Θ, z_j) phase space is represented in the panel C. The color refers to the different manifolds. Trajectories originating from the grey regions (I and II) eventually collide with the wall. Trajectories originating from blue (III) region asymptotically move on a straight line parallel to the channel midplane, red dot in the Θ, z_j phase space. Channel height, $h = 3.75$. Same swimmer geometry as in figure A.2.

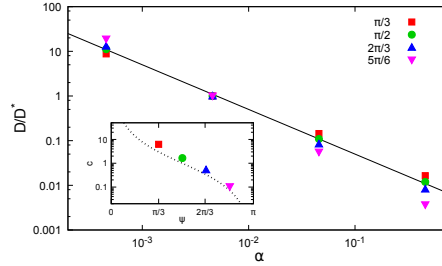


Figure A.6: Effective diffusion coefficient D as a function of the tumbling rate α for boundary escaping condition for different tumbling angle ψ . For the sake of clarity, D is normalized with the value obtained for $\alpha = 4.4 * 10^{-3}$. The solid line $D \sim \alpha^{-1}$ is drawn to guide the eye. The prefactor c is reported in the inset, the dotted line corresponds to the 2D random flight model prediction, eq. (A.5).

trapped at the wall and it follows an average straight line trajectory that lays on the channel midplane. Consequently, we expect that the dependence of the diffusion coefficient D as a function of the tumbling rate α , follows the strong confinement behaviour. Figure A.7C reports the diffusion coefficient D as a function of α for different values of the tumbling angle ψ for this intermediate channel height $h = 7.5$. The behaviour is essentially the same as discussed for the case of strong confinement, see figure A.6.

A.4 Conclusions

We analyzed the motion of a run-and-tumble *E.coli*-like swimmer in confined geometries. The motion is characterized in global terms by addressing the effective diffusion coefficient. This quantity can have a dramatic effect on the survival probability of a species, as

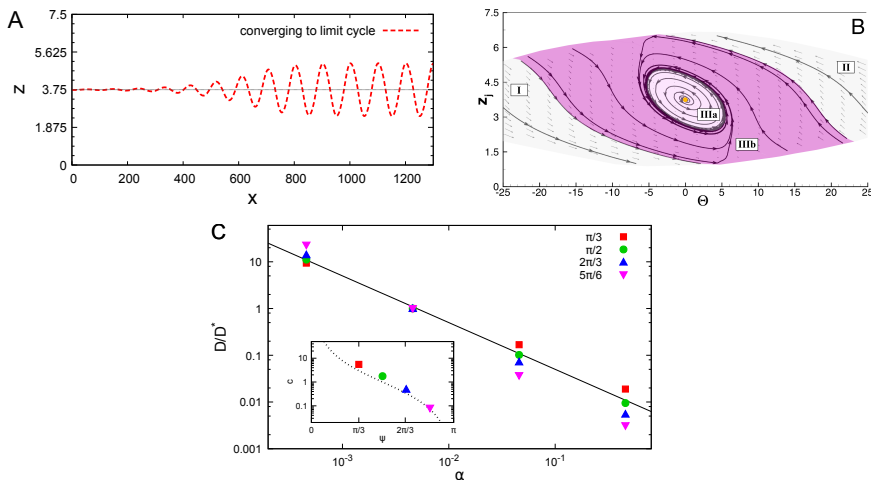


Figure A.7: Channel height $h = 7.5$. Same swimmer geometry as in figure A.2. Panel A reports the xz projection of the 3D trajectory that oscillates around the mid-plane. The reduced (Θ, z_j) phase space is shown in panel B. Trajectories originating from the grey regions (I and II) eventually collide with the wall. Trajectories originating from pink regions (III_a and III_b) asymptotically approach the limit cycle that corresponds to oscillating trajectories such as the one shown in panel A. The panel C reports the effective diffusion coefficient D as a function of the tumbling rate α for different tumbling angle ψ . D is normalized with the value obtained for $\alpha = 4.4 \times 10^{-3}$. The solid line $D \sim \alpha^{-1}$ is drawn to guide the eye. The prefactor c is reported in the inset, the dotted line corresponds to the 2D random flight model prediction, eq. (A.5).

A

suggested by Pigolotti and Benzi [89, 90], where it was shown that a small difference in the diffusion coefficient between two populations can result in a strong selective advantage towards the fastest species. Our data show that the diffusion coefficient D is a function of the tumbling rate and strongly depends on the confinement. In free space, D monotonically decreases with the tumbling rate α , namely, $D \sim v_0^2/\alpha$, with v_0 the swimmer speed. The simple argument beyond this well established result is that, during the run phase, the swimmer moves along a straight line for a distance $l = v_0/\alpha$. At time t , the mean square distance, after $N_t = t\alpha$ tumbling events is, $R^2(t) \simeq N_t l^2 \simeq (v_0^2/\alpha)t$, hence $D \simeq v_0^2/\alpha$. In weak confinement, the diffusion coefficient D shows a maximum for a specific value of the tumbling rate. Indeed, the hydrodynamic interaction between the swimmer and the channel walls, results in stable circular orbits close to the solid surface (boundary accumulation). At low tumbling rate α , the swimmer gets trapped in the stable orbit for a long time and, consequently, it is not able to explore the surrounding space, hence, for $\alpha \rightarrow 0$, $D \rightarrow 0$. As α increases, the tumbling events allow the swimmer to frequently escape from the stable orbit and to explore a larger portion of the space. The maximum of the diffusion coefficient is obtained for $\alpha \simeq \omega_s$, with ω_s the angular velocity along the stable circular orbit. Further increases of α result in a reduction of D . For high tumbling frequency (i.e. short run phase), the swimmer is never trapped on stable orbits and the trajectory during each run phase is approximatively a straight line. Hence, the same argument used for the free space case holds. For stronger confinement, stable orbits are not present and the hydrodynamic interaction results in the swimmer approximatively moving along a straight line laying on the channel's midplane. The scenario is similar to the free space case, the swimmer is now confined in a plane and the run phases are, as a first approximation, characterized by an almost straight motion. The diffusion coefficient monotonically decreases with α in rough agreement with a $1/\alpha$ scaling.

Bibliography

- [1] J. S. Guasto, R. Rusconi, and R. Stocker, “Fluid mechanics of planktonic microorganisms,” *Annual Review of Fluid Mechanics*, vol. 44, pp. 373–400, 2012.
- [2] C. B. Field, M. J. Behrenfeld, J. T. Randerson, and P. Falkowski, “Primary production of the biosphere: integrating terrestrial and oceanic components,” *Science*, vol. 281, no. 5374, pp. 237–240, 1998.
- [3] F. d’Ovidio, S. De Monte, S. Alvain, Y. Dandonneau, and M. Lévy, “Fluid dynamical niches of phytoplankton types,” *Proceedings of the National Academy of Sciences*, vol. 107, no. 43, pp. 18366–18370, 2010.
- [4] R. Benzi, M. H. Jensen, D. R. Nelson, P. Perlekar, S. Pigolotti, and F. Toschi, “Population dynamics in compressible flows,” *The European Physical Journal Special Topics*, vol. 204, no. 1, pp. 57–73, 2012.
- [5] P. Perlekar, R. Benzi, D. R. Nelson, and F. Toschi, “Population dynamics at high Reynolds number,” *Physical review letters*, vol. 105, no. 14, p. 144501, 2010.
- [6] P. A. P. Moran, “Random processes in genetics,” in *Mathematical Proceedings of the Cambridge Philosophical Society*, vol. 54, pp. 60–71, Cambridge University Press, 1958.
- [7] K. S. Korolev, M. Avlund, O. Hallatschek, and D. R. Nelson, “Genetic demixing and evolution in linear stepping stone models,” *Reviews of modern physics*, vol. 82, no. 2, p. 1691, 2010.
- [8] H. Hinrichsen, “Non-equilibrium critical phenomena and phase transitions into absorbing states,” *Advances in physics*, vol. 49, no. 7, pp. 815–958, 2000.
- [9] I. Dornic, H. Chaté, and M. A. Muñoz, “Integration of Langevin equations with multiplicative noise and the viability of field theories for absorbing phase transitions,” *Physical review letters*, vol. 94, no. 10, p. 100601, 2005.

- [10] S. Pigolotti, R. Benzi, P. Perlekar, M. H. Jensen, F. Toschi, and D. R. Nelson, “Growth, competition and cooperation in spatial population genetics,” *Theoretical population biology*, vol. 84, pp. 72–86, 2013.
- [11] A. Plummer, R. Benzi, D. R. Nelson, and F. Toschi, “Fixation probabilities in weakly compressible fluid flows,” *Proceedings of the National Academy of Sciences*, vol. 116, no. 2, pp. 373–378, 2019.
- [12] S. Pigolotti, R. Benzi, M. H. Jensen, and D. R. Nelson, “Population genetics in compressible flows,” *Physical review letters*, vol. 108, no. 12, p. 128102, 2012.
- [13] R. Benzi and D. R. Nelson, “Fisher equation with turbulence in one dimension,” *Physica D: Nonlinear Phenomena*, vol. 238, no. 19, pp. 2003–2015, 2009.
- [14] L. F. Richardson, “Atmospheric diffusion shown on a distance-neighbour graph,” *Proceedings of the Royal Society of London. Series A, Containing Papers of a Mathematical and Physical Character*, vol. 110, no. 756, pp. 709–737, 1926.
- [15] M. Cencini, A. Torcini, D. Vergni, and A. Vulpiani, “Thin front propagation in steady and unsteady cellular flows,” *Physics of Fluids*, vol. 15, no. 3, pp. 679–688, 2003.
- [16] F. Bianco, S. Chibbaro, D. Vergni, and A. Vulpiani, “Front speed in reactive compressible stirred media,” *Physical Review E*, vol. 87, no. 4, p. 042924, 2013.
- [17] C. R. Doering, C. Mueller, and P. Smereka, “Noisy wavefront propagation in the fisher-kolmogorov-petrovsky-piscounov equation,” in *AIP Conference Proceedings*, vol. 665, pp. 523–530, American Institute of Physics, 2003.
- [18] C. Darwin, *On the origin of species, 1859*. Routledge, 2004.
- [19] E. Lieberman, C. Hauert, and M. A. Nowak, “Evolutionary dynamics on graphs,” *Nature*, vol. 433, no. 7023, p. 312, 2005.
- [20] T. R. Malthus, “An essay on the principle of population, printed for j,” *Johnson, London*, 1798.
- [21] J. D. Murray, *Mathematical Biology I. An Introduction*, vol. 17 of *Interdisciplinary Applied Mathematics*. New York: Springer, 3 ed., 2002.
- [22] M. Kimura, “On the probability of fixation of mutant genes in a population,” *Genetics*, vol. 47, no. 6, p. 713, 1962.

- [23] M. Kimura and G. H. Weiss, "The stepping stone model of population structure and the decrease of genetic correlation with distance," *Genetics*, vol. 49, no. 4, p. 561, 1964.
- [24] M. Kimura and T. Ohta, "The average number of generations until fixation of a mutant gene in a finite population," *Genetics*, vol. 61, no. 3, p. 763, 1969.
- [25] T. Maruyama, "A simple proof that certain quantities are independent of the geographical structure of population," *Theoretical population biology*, vol. 5, no. 2, pp. 148–154, 1974.
- [26] R. A. Fisher, "The wave of advance of advantageous genes," *Annals of eugenics*, vol. 7, no. 4, pp. 355–369, 1937.
- [27] A. Kolmogorov, I. Petrovskii, and N. Piscunov, "A study of the equation of diffusion with increase in the quantity of matter, and its application to a biological problem," *Byul. Moskovskogo Gos. Univ.*, vol. 1, no. 6, pp. 1–25, 1937.
- [28] W. Van Saarloos, "Front propagation into unstable states," *Physics reports*, vol. 386, no. 2-6, pp. 29–222, 2003.
- [29] D. G. Aronson and H. F. Weinberger, "Nonlinear diffusion in population genetics, combustion, and nerve pulse propagation," in *Partial differential equations and related topics*, pp. 5–49, Springer, 1975.
- [30] U. Ebert and W. van Saarloos, "Front propagation into unstable states: universal algebraic convergence towards uniformly translating pulled fronts," *Physica D: Nonlinear Phenomena*, vol. 146, no. 1-4, pp. 1–99, 2000.
- [31] E. Brunet and B. Derrida, "Shift in the velocity of a front due to a cutoff," *Phys. Rev. E*, vol. 56, pp. 2597–2604, Sep 1997.
- [32] A. B. Ryabov and B. Blasius, "Population growth and persistence in a heterogeneous environment: the role of diffusion and advection," *Mathematical Modelling of Natural Phenomena*, vol. 3, no. 3, pp. 42–86, 2008.
- [33] H. Goldstein, C. Poole, and J. Safko, "Classical mechanics," 2002.
- [34] "La struttura locale della turbolenza in un fluido viscoso incompressibile per numeri di Reynolds molto grandi," *Cr Acad. Sci. URSS*, vol. 30.
- [35] J. Bec, "Fractal clustering of inertial particles in random flows," *Physics of fluids*, vol. 15, no. 11, pp. L81–L84, 2003.

- [36] C. W. Gardiner *et al.*, *Handbook of stochastic methods*, vol. 3. Springer Berlin, 1985.
- [37] N. G. Van Kampen, *Stochastic processes in physics and chemistry*, vol. 1. Elsevier, 1992.
- [38] C. R. Doering, C. Mueller, and P. Smereka, “Interacting particles, the stochastic Fisher–Kolmogorov–Petrovsky–Piscounov equation, and duality,” *Physica A: Statistical Mechanics and its Applications*, vol. 325, no. 1-2, pp. 243–259, 2003.
- [39] L. Biferale, A. Crisanti, M. Vergassola, and A. Vulpiani, “Eddy diffusivities in scalar transport,” *Physics of Fluids*, vol. 7, no. 11, pp. 2725–2734, 1995.
- [40] J. F. Crow, M. Kimura, *et al.*, “An introduction to population genetics theory,” *An introduction to population genetics theory.*, 1970.
- [41] R. MacArthur and R. Levins, “The limiting similarity, convergence, and divergence of coexisting species,” *The American naturalist*, vol. 101, no. 921, pp. 377–385, 1967.
- [42] S. A. Levin, “Community equilibria and stability, and an extension of the competitive exclusion principle,” *The American Naturalist*, vol. 104, no. 939, pp. 413–423, 1970.
- [43] F. Herrerías-Azcué, V. Pérez-Muñuzuri, and T. Galla, “Stirring does not make populations well mixed,” *Scientific reports*, vol. 8, no. 1, pp. 1–9, 2018.
- [44] J. M. Szymura and N. H. Barton, “Genetic analysis of a hybrid zone between the fire-bellied toads, *bombina bombina* and *b. variegata*, near cracow in southern poland,” *Evolution*, vol. 40, no. 6, pp. 1141–1159, 1986.
- [45] S. L. Strom, “Microbial ecology of ocean biogeochemistry: a community perspective,” *science*, vol. 320, no. 5879, pp. 1043–1045, 2008.
- [46] P. Belda-Ferre, L. D. Alcaraz, R. Cabrera-Rubio, H. Romero, A. Simon-Soro, M. Pignatelli, and A. Mira, “The oral metagenome in health and disease,” *The ISME journal*, vol. 6, no. 1, pp. 46–56, 2012.
- [47] A. Pérez-García, D. Romero, and A. De Vicente, “Plant protection and growth stimulation by microorganisms: biotechnological applications of bacilli in agriculture,” *Current opinion in biotechnology*, vol. 22, no. 2, pp. 187–193, 2011.
- [48] M. O. Lavrentovich and D. R. Nelson, “Nucleation of antagonistic organisms and cellular competitions on curved, inflating substrates,” *Physical Review E*, vol. 100, no. 4, p. 042406, 2019.

-
- [49] E. Lauga and T. R. Powers, “The hydrodynamics of swimming microorganisms,” *Reports on Progress in Physics*, vol. 72, no. 9, p. 096601, 2009.
- [50] R. Nash, R. Adhikari, J. Tailleur, and M. Cates, “Run-and-tumble particles with hydrodynamics: Sedimentation, trapping, and upstream swimming,” *Physical review letters*, vol. 104, no. 25, p. 258101, 2010.
- [51] H. C. Berg and D. A. Brown, “Chemotaxis in escherichia coli analysed by three-dimensional tracking,” *Nature*, vol. 239, no. 5374, pp. 500–504, 1972.
- [52] E. M. Purcell, “Life at low reynolds number,” *American journal of physics*, vol. 45, no. 1, pp. 3–11, 1977.
- [53] R. E. Goldstein, “Green algae as model organisms for biological fluid dynamics,” *Annual review of fluid mechanics*, vol. 47, pp. 343–375, 2015.
- [54] J. M. Yeomans, D. O. Pushkin, and H. Shum, “An introduction to the hydrodynamics of swimming microorganisms,” *The European Physical Journal Special Topics*, vol. 223, no. 9, pp. 1771–1785, 2014.
- [55] B. Nasouri and G. J. Elfring, “Hydrodynamic interactions of cilia on a spherical body,” *Physical Review E*, vol. 93, no. 3, p. 033111, 2016.
- [56] H. C. Berg, *E. coli in Motion*. Springer Science & Business Media, 2008.
- [57] J. Tailleur and M. Cates, “Sedimentation, trapping, and rectification of dilute bacteria,” *EPL (Europhysics Letters)*, vol. 86, no. 6, p. 60002, 2009.
- [58] E. Lauga, W. R. DiLuzio, G. M. Whitesides, and H. A. Stone, “Swimming in circles: motion of bacteria near solid boundaries,” *Biophysical journal*, vol. 90, no. 2, pp. 400–412, 2006.
- [59] R. Di Leonardo, D. Dell’Arciprete, L. Angelani, and V. Iebba, “Swimming with an image,” *Physical review letters*, vol. 106, no. 3, p. 038101, 2011.
- [60] H. Shum, E. Gaffney, and D. Smith, “Modelling bacterial behaviour close to a no-slip plane boundary: the influence of bacterial geometry,” *Proceedings of the Royal Society A: Mathematical, Physical and Engineering Sciences*, vol. 466, no. 2118, pp. 1725–1748, 2010.
- [61] D. Pimponi, M. Chinappi, P. Gualtieri, and C. M. Casciola, “Hydrodynamics of flagellated microswimmers near free-slip interfaces,” *Journal of Fluid Mechanics*, vol. 789, pp. 514–533, 2016.

- [62] G. Sinibaldi, V. Iebba, and M. Chinappi, “Swimming and rafting of e. coli microcolonies at air–liquid interfaces,” *MicrobiologyOpen*, vol. 7, no. 1, p. e00532, 2018.
- [63] K. Martens, L. Angelani, R. Di Leonardo, and L. Bocquet, “Probability distributions for the run-and-tumble bacterial dynamics: An analogy to the lorentz model,” *The European Physical Journal E*, vol. 35, no. 9, p. 84, 2012.
- [64] R. A. Fisher, *The genetical theory of natural selection*. 1958.
- [65] S. Wright, “Evolution in mendelian populations,” *Genetics*, vol. 16, no. 2, p. 97, 1931.
- [66] P. A. P. Moran *et al.*, “The statistical processes of evolutionary theory.,” *The statistical processes of evolutionary theory.*, 1962.
- [67] D. L. Hartl, A. G. Clark, and A. G. Clark, *Principles of population genetics*, vol. 116. Sinauer associates Sunderland, MA, 1997.
- [68] M. Kimura, “‘stepping stone’ model of population,” *Annual Report of the National Institute of Genetics Japan*, vol. 3, pp. 62–63, 1953.
- [69] P. Perlekar, R. Benzi, S. Pigolotti, and F. Toschi, “Particle algorithms for population dynamics in flows,” in *Journal of Physics: Conference Series*, vol. 333, p. 012013, IOP Publishing, 2011.
- [70] G. Guccione, R. Benzi, A. Plummer, and F. Toschi, “Discrete eulerian model for population genetics and dynamics under flow,” *Physical Review E*, vol. 100, no. 6, p. 062105, 2019.
- [71] C. Mueller and R. B. Sowers, “Random travelling waves for the KPP equation with noise,” *Journal of Functional Analysis*, vol. 128, no. 2, pp. 439–498, 1995.
- [72] V. Kachitvichyanukul and B. W. Schmeiser, “Binomial random variate generation,” *Communications of the ACM*, vol. 31, no. 2, pp. 216–222, 1988.
- [73] O. Hallatschek and K. Korolev, “Fisher waves in the strong noise limit,” *Physical Review Letters*, vol. 103, no. 10, p. 108103, 2009.
- [74] M. Abel, A. Celani, D. Vergni, and A. Vulpiani, “Front propagation in laminar flows,” *Physical Review E*, vol. 64, no. 4, p. 046307, 2001.
- [75] B. Pearson and B. Fox-Kemper, “Log-normal turbulence dissipation in global ocean models,” *Physical review letters*, vol. 120, no. 9, p. 094501, 2018.

- [76] H. Löwen, “Chirality in microswimmer motion: From circle swimmers to active turbulence,” *The European Physical Journal Special Topics*, vol. 225, no. 11-12, pp. 2319–2331, 2016.
- [77] F. Kümmel, B. ten Hagen, R. Wittkowski, I. Buttinoni, R. Eichhorn, G. Volpe, H. Löwen, and C. Bechinger, “Circular motion of asymmetric self-propelling particles,” *Physical review letters*, vol. 110, no. 19, p. 198302, 2013.
- [78] M. Chinappi and C. Casciola, “Intrinsic slip on hydrophobic self-assembled monolayer coatings,” *Physics of Fluids*, vol. 22, no. 4, p. 042003, 2010.
- [79] M. Sega, M. Sbragaglia, L. Biferale, and S. Succi, “Regularization of the slip length divergence in water nanoflows by inhomogeneities at the angstrom scale,” *Soft Matter*, vol. 9, no. 35, pp. 8526–8531, 2013.
- [80] C. Pozrikidis *et al.*, *Boundary integral and singularity methods for linearized viscous flow*. Cambridge University Press, 1992.
- [81] G. Sharma, A. Agarwala, and B. Bhattacharya, “A fast parallel gauss jordan algorithm for matrix inversion using cuda,” *Computers & Structures*, vol. 128, pp. 31–37, 2013.
- [82] D. Pimponi, M. Chinappi, P. Gualtieri, and C. M. Casciola, “Mobility tensor of a sphere moving on a superhydrophobic wall: application to particle separation,” *Microfluidics and nanofluidics*, vol. 16, no. 3, pp. 571–585, 2014.
- [83] L. Zhu, E. Lauga, and L. Brandt, “Low-reynolds number swimming in a capillary tube,” *arXiv preprint arXiv:1304.7671*, 2013.
- [84] H. Shum and E. A. Gaffney, “Hydrodynamic analysis of flagellated bacteria swimming near one and between two no-slip plane boundaries,” *Physical Review E*, vol. 91, no. 3, p. 033012, 2015.
- [85] C. Condat, J. Jäckle, and S. Menchón, “Randomly curved runs interrupted by tumbling: A model for bacterial motion,” *Physical Review E*, vol. 72, no. 2, p. 021909, 2005.
- [86] D. Giacché, T. Ishikawa, and T. Yamaguchi, “Hydrodynamic entrapment of bacteria swimming near a solid surface,” *Physical Review E*, vol. 82, no. 5, p. 056309, 2010.
- [87] M. Doi, S. F. Edwards, and S. F. Edwards, *The theory of polymer dynamics*, vol. 73. oxford university press, 1988.

- [88] J. de Graaf, A. J. Mathijssen, M. Fabritius, H. Menke, C. Holm, and T. N. Shendruk, “Understanding the onset of oscillatory swimming in microchannels,” *Soft Matter*, vol. 12, no. 21, pp. 4704–4708, 2016.
- [89] S. Pigolotti and R. Benzi, “Selective advantage of diffusing faster,” *Phys. Rev. Lett.*, vol. 112, p. 188102, May 2014.
- [90] S. Pigolotti and R. Benzi, “Competition between fast-and slow-diffusing species in non-homogeneous environments,” *Journal of theoretical biology*, vol. 395, pp. 204–210, 2016.

Summary

In nature, the expansion of biological organisms is generally traced back to the contribution of both individual spatial dispersion and growth. In the case of aquatic systems, microbial processes are influenced by turbulent flows which can have an impact on the microorganisms' dynamics. This Ph.D. dissertation deals with understanding the incidence of compressible turbulence on the fixation probability of a particular species having a selective advantage.

The introduction and a review of the state of the art methods are introduced in chapter 1 and chapter 2, respectively.

A new method capable of describing the dynamics of two competing species is proposed in chapter 3. This technique resulted computationally very efficient for the study of a large number of individuals composing a population. We investigated the new approach in one and two dimensions, and in presence of a weakly compressible fluid. It was found that the compressible fluid can have a significant impact on the dynamics of the organisms.

The proposed method is employed in chapter 4 to investigate the population dynamics at the limit of "strong noise". We examined the impact of the system diffusivity on the fixation probability of a beneficial allele. Moreover, an incompressible velocity field has been considered in order to explore possible related effects on the population dynamics. It was found that the fixation probability does depend neither on the diffusivity nor on the advection, with this latter, assumed to be incompressible.

The theoretical study in chapter 5 examines the impact of genetic drift on the dynamics of two antagonistic species. The effect of a compressible velocity field is also considered. In order to explain the contribution of random genetic fluctuations, deterministic results are compared with agent simulations. For all the considered cases, a good agreement between the theoretical and numerical outcomes is found.

Giorgia Guccione

Curriculum Vitae



🏠 Viale Spartaco 91, Roma, Italia 00174
☎ +39 328 0743988
✉ guccione.giorgia@gmail.com
♀ Gender Female
📅 Date of Birth 22/10/1990
🇮🇹 Nationality Italian

WORK EXPERIENCE

OCTOBER 2020 – CURRENT

Researcher & Aeronautical Meteorological Forecaster
ENAV S.P.A., Rome (Italy)

AUGUST 2018 – CURRENT

Population Dynamics in Turbulent Flows
Joint Ph.D. in Theoretical Physics between :
Eindhoven University of Technology, Eindhoven
(Netherlands) &
Roma Torvergata University of Technology, Rome
(Italy)
Position Held: Ph.D.

JANUARY 2018 – APRIL 2018

Population Dynamics in Turbulent Flows
HPC-Europa3 Transnational Access Programme
Eindhoven University of Technology, Eindhoven
(Netherlands)
Position Held: Ph.D.

This project focus on the enhancement or inhibition of selective advantage in population dynamics subject to advection of compressible turbulence.

OCTOBER 2016 – CURRENT

Population Dynamics in Turbulent Flows
Theoretical Physics \ Computational Fluid Dynamics
Ph.D.

Roma Torvergata University of Technology, Rome
(Italy)

Position Held: Ph.D.

MARCH 2015 – MAY 2015

Atmospheric Physics and Meteorology
R.A.C.S.A. Training Department Airspace Control
Pratica di Mare Air Base, Rome (Italy)

Position Held: Operative Internship

Theoretical and Practical knowledge about Aeronautical Meteorology, Marine Meteorology, Aeronautical Codes.
Job Training at Airport Weather Office and C.N.M.C.A (National Center of Aeronautics Meteorology and Climatology).
Qualification provided by the World Meteorological Organization WMO, Weather Forecasters for the resolution of problems of flight assistance related to climatic phenomena.

FEBRUARY 2014 – SEPTEMBER 2014

Computational Fluid Dynamics
Exchange Program
Eindhoven University of Technology, Eindhoven
(Netherlands)

Position Held: Internship

Data Analysis and Simulations to understand the behavior of microorganisms motility exposed to turbulent flow. The dynamics of motile microorganisms has a profound effect on the ecology of aquatic environments and at the global scale.

JANUARY 2013 – SEPTEMBER 2013

Atmospheric Chemistry and Physics
National Research Council, Rome (Italy)

Position Held: Internship

In-depth Study and Data Analysis of of Aerosol particles in Atmosphere; their importance is related to the Earth's radiation balance, visibility and human health.

2008 – CURRENT

Occasional Employments
Position Held: Promoter - Hostess

Promotion activity and Sale
Organization and Management Events

SOCIAL SKILLS AND COMPETENCES

Confident and highly motivated person and ready to experiment new areas of work.

Ability to work both autonomously and within a team; organize and manage several projects concurrently.

Flexibility to travel abroad, willing to adapt quickly and easily to multicultural environments.

PERSONAL SKILLS

Mother Tongue	ITALIAN
Other Language	ENGLISH
	Comprehension [Listening B2 - Reading C1]
	Speaking [Interaction B2 - Oral Production B2]
	Writing [B2]

COMPUTER SKILLS

Intermediate Knowledge	Mac based Operating Systems Microsoft Windows, OpenOffice, Fortran, C, L ^A T _E X,
------------------------	---

DRIVING LICENCES

A1, B

EDUCATION

- 2018 **Joint-Ph.D.**
PHYSICS RESEARCH
University of Rome TorVergata,
Eindhoven University of Technology,
Rome (Italy) - Eindhoven (Netherlands)
- 2018 **Europe Scholarship**
PHYSICS RESEARCH
SURFsara chance to operate with one of
the largest Hadoop clusters for
scientific research in the Netherlands
*Eindhoven University of Technology,
Eindhoven (Netherlands)*
- 2016 – PRESENT **Ph.D. in Theoretical Physics**
*University of Rome TorVergata,
Rome (Italy)*
- 2016 **Master's Degree**
PHYSICS
Thesis on Physics of Microswimmers
Physics Research
"Hydrodynamic analysis of
flagellated swimmers
under confinement"
TorVergata University, Rome (Italy)
- 2015 **Meteorologist Qualification**
10 COURSE OF ATMOSPHERIC PHYSICS
AND METEOROLOGY
Certificate of Attendance
contents adhering to ENAC Regulation
for the provision of meteorological
services ed.2011 for initial training of
the Aeronautical Meteorologist
Pratica di Mare Air Base, Rome (Italy)
- 2014 **Exchange Program**
FLUID DYNAMICS
Exchange program and relative exams
*Eindhoven University of Technology,
Eindhoven (Netherlands)*
- 2013 **Bachelor's Degree**
ATMOSPHERIC PHYSICS
AND METEOROLOGY
Thesis on Atmospheric Chemistry and
Physics Research
"Optical Properties of
Ultrafine Aerosol Particle
in Troposphere"
TorVergata University, Rome (Italy)
- 2009 **High School Diploma**
*High Scientific School "I. Newton",
Rome (Italy)*

PUBLICATIONS

Guccione Giorgia, et al. “Discrete Eulerian model for population genetics and dynamics under flow.”
Physical Review E 100.6 (2019): 062105.

Guccione Giorgia, et al. “Diffusivity of E. coli-like microswimmers in confined geometries: The role of the tumbling rate.”
Physical Review E 96.4 (2017): 042603.

ATTENDANCE AT COURSES CONFERENCE AND SEMINARS

JANUARY 21-22, 2020

CONGRESS Topical Overview of Physics in the
Netherlands
Veldhoven, (Netherlands)

JULY 8-12, 2019

CONFERENCE International Conference on Statistical
Physics, StatPhys27
IUPAP, Buenos Aires (Argentina)

JUNE 12-14, 2019

WORKSHOP Statistical Mechanics of Active Matter
GSSI, Gran Sasso Science Institute, L'Aquila (Italy)

JANUARY 22-23, 2019

CONGRESS Topical Overview of Physics in the
Netherlands
Veldhoven, (Netherlands)

NOVEMBER 18-20, 2018

CONFERENCE 71st Annual Meeting of the American
Physical Society's Division of Fluid Dynamics (DFD)
Georgia World Congress Center in Atlanta (Georgia)

SEPTEMBER 9-13, 2018

CONFERENCE 12th European Fluid Mechanics
Conference
TU Wien, Vienna (Austria)

JANUARY 23-24, 2018

CONGRESS Topical Overview of Physics in the
Netherlands
Veldhoven, (Netherlands)

JULY 10-21, 2017

26th SUMMER SCHOOL on Parallel Computing
Offices of Cineca, Rome (Italy)

MAY 22-26, 2017
CONFERENCE Fluids and Structures: Interaction and
Modeling
Naples, (Italy)

MAY 8-12, 2017
COURSE Complex Flows and Complex Fluids
CISM Udine (Italy)

MAY 3-5, 2017
COURSE Introduction to technical and computing in
C
Offices of Cineca, Rome (Italy)

MARCH 13-16, 2017
COURSE Introduction to modern Fortran
Offices of Cineca, Rome (Italy)

Acknowledgements

At the end of this path I feel to thank those who, in various ways, took part in these important Phd years.

My first thought goes to my supervisor Roberto Benzi.

Roberto, grazie per aver creduto in me ed avermi dato questa incredibile opportunità. Spesso mi sono scontrata con i limiti e le difficoltà a cui la ricerca mette di fronte, ma tu c'eri sempre come sostegno ed ispirazione. Ogni tua parola per me è insegnamento. Mi sento onorata di aver avuto vicino una persona come te e spero che il nostro rapporto di collaborazione e personale continui a lungo.

I would like to thank my supervisor Federico Toschi who let me to join the European joint doctorate program, allowing me to travel back to my sunny and beloved Eindhoven, that is like my second home.

Federico, la tua passione per la ricerca è affascinante. Hai molti progetti ed il tuo applicarti per ognuno di essi è davvero stimolante e ne farò tesoro. Mi dispiace se tutt'ora non vado d'accordo con gitlab ma ti prometto che un giorno o l'altro, in un futuro prossimo, ci farò pace! Grazie ancora per la tua guida ed i tuoi consigli.

I'm deeply indebted to my lovely Abby! What would have happened if I hadn't met you? Since the beginning you were always there for me despite the kilometers that keep us apart! You shared with me all your knowledge, always with a big smile and super enthusiastically! You're a great inspiration and a real friend to me!

I wish to express my gratitude to David Nelson for the helpful discussions on many different aspects of my project.

Thanks to Marjan, for the kind support and to arrange all the bureaucratic formalities. A special thanks to *F&F* group! In particular to Gianluca and Alessandro grazie per aver risolto tanti anzi tantissimi dei mille intoppi per cui venivo a stressarvi! Grazie a Matteo e ad Arianna per la vostra sincera amicizia! Siete una coppia di sposini bellissimi e non vedo l'ora di conoscere il piccolo in arrivo!

Thanks to Francesca, la perfetta office-mate! Sei stata tanto importante in tutto questo percorso! Ne abbiamo passate davvero tante insieme tra risate, gioie, pianti, crisi nervose, avvenimenti assurdi, viaggi dall'altra parte del mondo.. ci siamo divertite tanto! Ed ormai da amiche-colleghe passiamo solo ad amiche-amiche!

The time that I spent in Eindhoven wasn't always so easy to me but during this journey. I met people who have contributed to make everything better!

The first person that i want to thank is Tanya! You are precious and we had so great time together! I cannot wait to come to visit you in Amsterdam and go skating somewhere! Ed un grazie mille va a tutti i voi: Geckino, Gabriele, Basic, Sergino, Marco, Giacomo, Claudia, Mandy, Viviana sono le persone che rendono belli i posti ed avete decisamente migliorato e reso speciale il mio vivere abroad!

Thanks to all my lifelong friends, in particular to Marta, Chiara, Carola, Elisa e Cristina always there for me! Non c'è distanza che tenga :P

Grazie Simone. "Tu mi hai raccolto come un gatto e mi hai portato con te"

Hai stravolto la mia vita ed illuminato i miei giorni.

Grazie per credere sempre in me e darmi un sostegno incredibile.

Grazie per gli stimoli che mi dai e per spronarmi ad essere sempre migliore.

Grazie per la tua infinita pazienza e speranza.

Thanks to me, per ricordarmi, un giorno, che questo lungo percorso non è stato semplice né emotivamente né fisicamente, spesso è stata dura ritrovarsi sola. E' stata una sfida per alcuni tratti più grande di me ma ho tenuto duro e sono stata tenace.

Grazie ai miei genitori ed a mia sorella, per essersi fatti carico, in questi anni, di ogni mio stato d'animo e per aiutarmi, sostenermi ed amarmi smisuratamente sempre.

Grazie ai miei piccoli nipoti, di cui sono follemente innamorata, Mattia e Flavio, la cui curiosità mi motiva e ricorda da dove nasce l'amore per la ricerca.

Grazie a mia nonna ed a tutta la mia splendida famiglia, che fa sì che io sia così incredibilmente fortunata.